First La Plata

International School

Compact Objects and their Emission

Edited by

Ileana Andruchow
IALP-FCAG, CCT La Plata, CONICET-UNLP

Gustavo E. Romero
IAR-CONICET, CCT La Plata, FCAG-UNLP

La Plata, 2009

Scientific Contributions

First International School on Astronomy and Geophysics

Compact Objects and their Emission

Facultad de Cs. Astronómicas y Geofísicas, UNLP, La Plata, Argentina

11–14 March 2008

First La Plata International School
Compact Objects and their Emission: Scientific Contributions.
Coordinado por Ileana Andruchow y Gustavo E. Romero. -1a ed. -
La Plata : Univ. Nacional de La Plata, 2009.
145 p. 26x17 cm.

ISBN 978-950-34-0555-0

1. Astrofísica. I. Andruchow, Ileana, coord. II. Romero, Gustavo E., coord.
CDD 523.01

Fecha de catalogación: 06/05/2009

LA PLATA
2009

Index

Preface

The present volume contains the contributions of the participants of the First La Plata International School on Astronomy and Geophysics, which was held at La Plata Observatory in March 2008, with the participation of 65 advanced and graduted students from 14 different countries. The School was devoted to the subject of "Compact Objects and their Emission", being hosted by the Group of Relativistic Astrophyscis and Radio Astronomy (GARRA) and the Chair of Relativistic Astrophysics of the *Facultad de Ciencias Astronómicas y Geofísicas*, *FCAG*, University of La Plata. Ten Professors, selected among some of the most respected authorities in the field, lectured during a whole week in the nice and classical environment of La Plata Observatory about white dwarfs, neutron stars, black holes, radiative process and all type of phenomena related to the astrophysics of compact objects. These lectures are contained in a companion volume.

During the School, the participants had the opportunity to present their own research in front of the professors and students. This book is formed by these contributions and represents a good sample of the current state of research on compact objects and related astrophyscis. All manuscripts were subject to expert review. The volume contains only those works that were finally accepted for publication after such reviewing process.

The School was a huge step forward in the academic offer of La Plata University in the field of astrophysics. It was only possible thanks to the initiative and continous support of the Head of FCAG, Dr. Pablo Cincotta, and the Vice-Head, Dr. Amalia Meza. As organizers, we are deeply grateful to them and to the Academic Council of FCAG (HCA). Additional thanks are due to Ezequiel García (electronics), Rubén Martínez, Eduardo Suárez (informatics), the Local Organizing Committee (Ileana Andruchow, Anabella T. Araudo, Paula Benaglia -Chair-, Pablo M. Cincotta, Mariana Orellana, and Gabriela S. Vila), the maintenance personnel (especially María and Claudio), and the many students from FCAG that helped in one way or another.

We want also to thank the different organizations that provided support to make of this School a reality: the Argentine Astronomical Society (AAA), the University of La Plata (FCAG), the National Research Council (CONICET), the National Agency for the Promotion of Science and Technology (ANPCyT), and the Center of Students of FCAG-UNLP

Our final thanks are for the professors and students, who made of this event not only an academic success but also an extremely enjoyable experience.

Ileana Andruchow & Gustavo E. Romero
Editors
La Plata, January 5th, 2009.

First La Plata International School, 2008
Compact Object and their Emission, 2009
Ileana Andruchow & Gustavo E. Romero, eds.

Non-thermal emission from massive YSOs. Exploring the spectrum at high energies

Anabella T. Araudo[1,2], Gustavo E. Romero[1,2], Valentí Bosch-Ramon[3] & Josep M. Paredes[4]

[1]*Instituto Argentino de Radioastronomía, (CCT La Plata - CONICET) Casilla de Corrreos No. 5, Villa Elisa 1894, Provincia de Buenos Aires ARGENTINA. E-mail: aaraudo@fcaglp.unlp.edu.ar*

[2]*Facultad de Cs. Astronómicas y Geofísicas, Universidad Nacional de La Plata, Paseo del Bosque, 1900 La Plata, Argentina*

[3] *Max Planck Institut für Kernphysik, Saupfercheckweg 1, Heidelberg 69117, Germany*

[4]*Departament d'Astronomia i Meteorologia, Universitat de Barcelona, Martí i Franquès 1, 08028, Barcelona, Spain*

Abstract. Thermal radio and X-ray emission has been traditionally associated with the formation of stars. However, in recent years, non-thermal radiation from massive star forming regions has been detected.

Synchrotron radio emission and non-thermal X-rays from the outflows of massive young stellar objects (YSOs) provide evidence of the presence of relativistic particles in these sources. In YSOs, the acceleration of particles is likely produced where the thermal jet impacts on the surrounding medium and a shock wave is formed. Thus, particles might be accelerated up to relativistic energies through a Fermi-I type mechanism.

Relativistic electrons and protons can interact with thermal particles and photons, producing then γ-rays. These energetic photons could be detected by the new generation of instruments, making massive YSOs a new population of γ-ray surces.

In the present contribution we briefly describe some massive star forming regions from which non-thermal radio emission has been detected. In addition, we present a general model for high-energy radiation from the massive YSOs embedded in these regions. We take into account both leptonic and hadronic interactions of particles accelerated at the termination points of the collimated outflows ejected from the protostar.

1. Introduction

The mechanism of formation of massive stars ($M > 8M_{\odot}$) remains one of the open questions in astrophysics. Massive stars appear in massive star associations where cloud fragmentation seems to be common. It is known that these stars originate inside giant and massive molecular clouds but the sequence of processes that take place during the formation of the star are mostly unknown. It has

been suggested, for example, that the coalescence of various protostars in the same cloud can lead to the emergence of a massive star (Bonnell et al. 1998). Alternatively, a massive star could form by the collapse of the core of a molecular cloud, with associated episodes of mass accretion and ejection, as observed in low-mass stars (Shu et al. 1987). In such a case, the effects of jets propagating through the medium that surrounds the protostar should be detectable. Until now, the formation of stars has been mostly associated with thermal radio and X-ray emission. However, non-thermal radio emission has been detected in some massive star forming regions. This is a clear evidence that efficient particle acceleration is occurring there, which may have as well a radiative outcome at energies much higher than radio ones. In the present contribution, based on recent multiwavelength observations and reasonable physical assumptions, we show that massive protostars could produce a significant amount of radiation in the gamma-ray domain, because of the dense and rich medium in which they are formed.

2. Non-thermal radio sources

In recent years, synchrotron radiation has been observed from some regions where massive stars form. This emission is associated with outflows emanating from a central protostar. In what follows, we briefly describe some of these non-thermal radio sources that could be potential emitters of gamma-rays.

2.1. IRAS 16547−4247

The triple radio source associated with the protostar IRAS 16547−4247 is one of the best candidates to produce gamma-rays. This system is located within a very dense region (i.e. densities $n \approx 5 \times 10^5$ cm^{-3}) of a giant molecular cloud located at a distance of 2.9 kpc. The luminosity of the IRAS source is $L = 6.2 \times 10^4 L_\odot$, possibly being the most luminous known YSO associated with collimated thermal jets.

ATCA and VLA observations (Garay et al. 2003, Rodríguez et al. 2005) have shown that the southern lobe of this system, of size $\sim 10^{16}$ cm, has a clear non-thermal spectrum, with an index $\alpha \sim 0.6$ ($S_\nu \propto \nu^{-\alpha}$). The specific flux of this source is 2 mJy at 14.9 GHz and the estimated magnetic field is $B \sim 2 \times 10^{-3}$ G (Araudo et al. 2007).

2.2. Serpens

The Serpens molecular cloud is located at a distance of ~ 300 pc. One of the two central dense cores of this cloud is a triple radio source, composed by a central protostar (IRAS 18273−0113) and two lobes. The northwest (NW) hot-spot is connected with the central source by a highly collimated thermal jet, whereas the southeast (SE) is separated and broken into two clumps. The luminosity of the source IRAS 18273−0113 is $L \sim 300 L_\odot$ and the particle density at the center of the molecular cloud is $n_0 \sim 10^5$ cm^{-3}.

The observed radio emission (Rodríguez et al. 1989, Curiel et al. 1993) detected from the central and NW sources has a spectral index $\alpha \approx -0.15$ and $\alpha \approx 0.05$, respectively. This emission, of a luminosity $\sim 2 - 3$ mJy, is produced

via thermal Bremsstrahlung. However, the radiation produced in the SE lobe seems to be non-thermal ($\alpha = 0.3$), likely produced via synchrotron emission. The specific flux of this source is $2 - 5$ mJy. The equipartition magnetic field estimated in the SE lobe is $B_{\rm equip} \sim 10^{-3}$ G (Rodríguez et al. 1989).

2.3. HH 80-81

The famous Herbig-Haro objects called HH 80−81 are the south component of a system of radio sources located in the Sagitarius region, at a distance of 1.7 kpc. The central source has been identified with the luminous ($L = 1.7 \times 10^4 L_\odot$) protostar IRAS 18162−2048. HH 80 North is the northern counterpart of HH 80−81. The velocity of the jet has been estimated as $v \sim 700$ km s^{-1}, allowing to derive a dynamical age for the system similar to 4000 yr.

Radio observations carried out with the VLA instrument (Martí et al. 1993) showed that the central source has a spectral index $\alpha \sim 0.1$, typical of free-free emission, whereas HH 80−81 and HH 80 North are likely non-thermal sources, with spectral index $\alpha \sim 0.3$. The specific flux measured at a frecuency of 5 GHz is $F_\nu \sim 1 - 2$ mJy and $F_\nu \approx 2.4$ mJy for the sources HH 80−81 and HH 80 North, respectively. At this frecuency, the angular size of the north and the south components are $\sim 6''$.

In addition, the HH 80−81 system is a source of thermal X-rays with a luminosity $L_X \sim 4.3 \times 10^{31}$ erg s^{-1} (Pravdo et al. 2004).

2.4. W3(OH)

Another interesting source to study is the system composed by an H_2O maser complex and the Turner-Welch (TW) source in the W3 region (Wilner et al. 1999). The central source of this system is a very luminous ($L \sim 10^5 L_\odot$) YSO and the mean density of cool particles is $n \sim 4 \times 10^4$ cm^{-3}. The distance to W3(OH) is 2.2 kpc.

Continuum radio observations (Wilner et al. 1999) show the presence of a sinuous double-sided jet, emanating from the TW source. The observed radio flux, from 1.6 to 15 GHz, is in the range 2.5-0.75 mJy, and the spectral index of the observed emission is clearly non-thermal: $\alpha = 0.6$. The inhomogeneous synchrotron model proposed by Reid et al. (1995) predicts for the emitting jet a density of relativistic electrons $n_e(\gamma, r) = 0.068\gamma^{-2}(r/r_0)^{-1.6}$ cm^{-3} and a magnetic field $B(r) = 0.01(r/r_0)^{-0.8}$ G, where $r_0 = 6.6 \times 10^{15}$ cm, and r and γ are the distance to the jet origin and the electron Lorentz factor, respectively. Unlike in the previous cases, here the non-thermal radio emission comes from the jet and not from its termination region. Non-thermal jets associated with a YSO are uncommon.

3. Acceleration of particles and losses

The non-thermal radio emission observed in some massive star forming regions is interpreted as synchrotron radiation produced by the interaction of relativistic electrons with the magnetic field present in the cloud, being typically $B_{\rm cloud} \sim 10^{-3}$ G (Crutcher 1999). These particles could be accelerated at a shock, formed in the point where the jet terminates, via diffusive shock acceleration (Drury

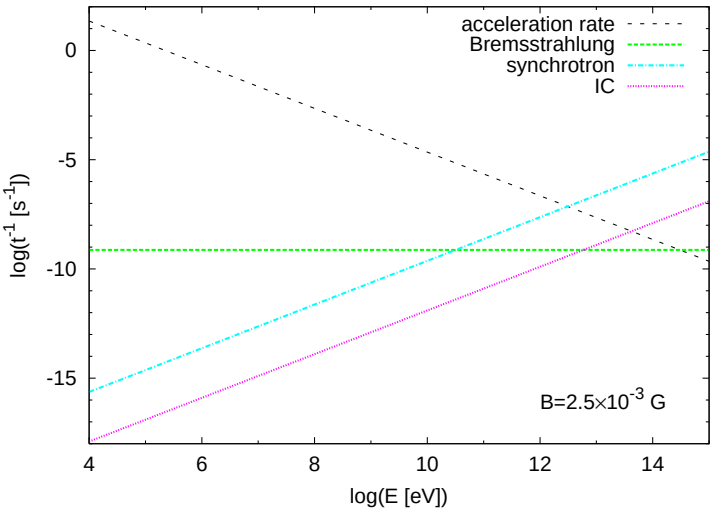

Figure 1. Energy loss and acceleration rates for electrons in the IRAS 16547−4247 southern lobe.

1983). The acceleration efficiency, characterized by η, is related to the velocity of the shock. Using the values of the velocities given for the sources described in the previous section, and assuming Bohm diffusion, values for η of $\sim 10^{-6} - 10^{-5}$ are obtained.

Particles accelerated up to relativistic energies interact with the different fields present in the medium. As noted at the beginning of this section, electrons radiate synchrotron emission under the ambient magnetic field B. In addition, particles, electrons and protons, can also interact with the cold matter in the jet termination region (via relativistic Bremsstrahlung the leptons, and inellastic proton-nuclei collisions the protons). In addition, electrons interact with the background field of IR photons of the protostar, of energy density $u_{\rm ph}$, through inverse Compton (IC) scattering.

Using the following parameter values: $n = 5 \times 10^5$ cm^{-3}; $B = 2.5 - 3 \times 10^{-3}$ G; and $u_{\rm ph} = 3.2 \times 10^{-9}$ erg cm^{-3} given for IRAS 16547−4247 (Garay et al. 2003, Araudo et al. 2007), we estimate the cooling time of the main leptonic processes in this scenario. As seen in Figure 1, relativistic Bremsstrahlung losses are dominant up to ~ 10 GeV. In addition, it is possible to see from this figure that the maximum energy achieved by electrons is $E_e^{\rm max} \sim 4$ TeV and is determined by synchrotron losses, being IC losses negligible.

Protons can be accelerated by the shock in the same way as electrons and interact with cold particles present in the cloud. The maximum energy achieved by protons is higher, $E_p^{\rm max} \sim 10^2$ TeV, and determined by the size of the acceleration region. In *pp* interactions, besides γ-rays, secondary electron-positron pairs are produced. The maximun energies of these leptons is $E_{e^\pm}^{\rm max} \sim 10$ TeV. These secondary particles will radiate by the same mechanisms as primary electrons (i.e. synchrotron radiation, IC scattering and relativistic Bremsstrahlung).

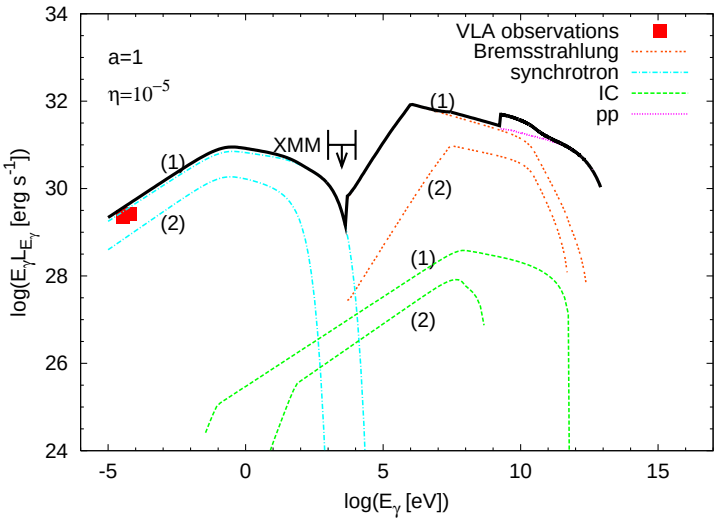

Figure 2. Spectral energy distribution for the south lobe of the YSO embedded in the source IRAS 16547−4247, for the case $a = 1$. The radiative contribution of secondary pairs (2) produced via $\pi^{\pm}$-decay is shown along with the contribution of primary electrons (1).

4. High-energy emission

In order to calculate the non-thermal spectral energy distribution (SED) of a massive protostar, the magnetic field of the cloud and the distributions of relativistic particles, $n(E)$, are needed. To obtain the magnetic field B and the normalization constants of the particle distributions, we use the standard equations given by Ginzburg & Syrovatskii (1964) for the observed synchrotron flux and assume equipatition between the magnetic and the relativistic particle energy densities:

$$\frac{B^2}{8\pi} = u_e + u_p + u_{e^{\pm}}, \tag{1}$$

where u_e , u_p and $u_{e^{\pm}}$ are the energy density of relativistic electrons, protons and secondary pairs, respectively. In Eq. (1), the following relationships are implicit: $u_{\rm p} = a\, u_{\rm e}$ and $u_{e^{\pm}} = f\, u_{\rm p}$. The constant a is a free parameter of the model, that characterizes how much energy goes to the different types of accelerated particles and f can be estimated using the average ratio of the number of secondary pairs to π^0-decay photons as in Kelner et al. (2006).

In Figs. 2 and 3, we show the computed broadband SEDs for the parameters of the source IRAS 16547−4247, in the cases with $a = 1$ (equipartition between protons and electrons) and $a = 100$ (larger acceleration efficiency in protons than in electrons). As seen from these figures, in the former case the leptonic emission is dominated by the primary electron population and in the latter by the secondary pairs. The typical lepton luminosities are $L_e \sim 10^{32}$ erg s^{-1}. Regarding the hadronic emission, the luminosity produced by π^0-decay is higher in the case $a = 100$, reaching a value of $L_{pp} \sim 5 \times 10^{32}$ erg s^{-1}.

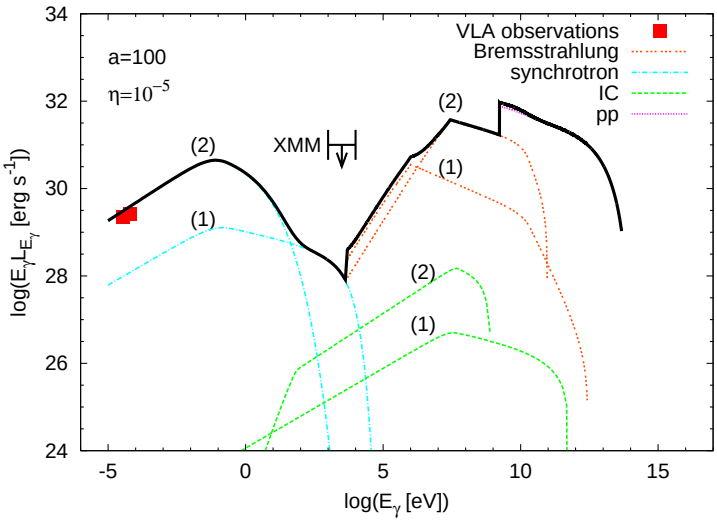

Figure 3. The same as in Fig. 2, but for the case $a = 100$.

5. Discussion

In this work we show that, if the source is located at few kpc, the high-energy emission may be detected by GLAST and even by forthcoming Cherenkov telescope arrays after long enough exposure. This opens a new window to the study of star formation and related processes. Also, determinations of the particle spectrum and its high-energy for different sources with a variety of environmental conditions can shed light on the properties of galactic supersonic outflows, and on the particle acceleration processes occurring at their termination points.

Radio observations already demonstrate that relativistic electrons are produced in some sources. According to the presence of non-thermal emission detected at cm-wavelengths and IR observations of the protostar emission we can suggest several good candidates to be targeted by GLAST. These objects are IRAS 16547−4247 (Araudo et al. 2007), the multiple radio source in Serpens (Rodríguez et al. 1989, Curiel et al. 1993), HH 80−81 (Martí et al 1993) and W3 (Reid et al. 1995, Wilner et al. 1999).

To conclude, we emphasize that massive YSO with bipolar outflows and non-thermal radio emission can form a new population of gamma-ray sources that could be unveiled by the next generation of γ-ray instruments.

Acknowledgments. A.T.A. and G.E.R. are supported by CONICET (PIP 5375) and the Argentine agency ANPCyT through Grant PICT 03-13291 BID 1728/OC-AC. V.B-R. gratefully acknowledges support from the Alexander von Humboldt Foundation. V.B-R., and J.M.P acknowledge support by DGI of MEC under grant AYA2004-07171-C02-01, as well as partial support by the European Regional Development Fund (ERDF/FEDER).

References

Araudo, A. T. et al. 2007, A&A, 476, 1289
Bonnell, I. A., Bate, M. R., & Zinnecker H. 1998, MNRAS 298, 93
Crutcher, R. M. 1999, ApJ, 520, 706
Curriel, S. et al. 1993, ApJ, 415, 191
Drury, L. O'C. 1983, Rep. Prog. Phys., 46, 973
Garay, G. 2003, ApJ, 537, 739
Ginzburg, V. L., & Syrovatskii, S. I. 1964, *The Origin of Cosmic Rays*, Pergamon Press, New York
Kelner, S. R., Aharonian, F. A., & Vugayov, V. V. 2006, Phys. Rev. D, 74, 034018
Martí, J., Rodríguez, L. F., & Reipurth, B. 1993, ApJ, 449, 184
Pravdo, S. H., Tsuboi, Y., & Maeda, Y. 2004, ApJ, 605, 259
Reid, M. J. et al. 1995, ApJ, 443, 238
Rodríguez, L. F. et al. 1989, ApJ, 346, L85
Rodríguez, L. F. 2005, ApJ, 626, 953
Shu, F. H., Adams, F. C., & Lizano, S. 1987, ARA&A, 25, 23
Wilner, D. J., Reid, M. J., & Menten, K. M. 1999, ApJ, 513, 775

First La Plata International School, 2008
Compact Object and their Emission, 2009
Ileana Andruchow & Gustavo E. Romero, eds.

The influence of strong magnetic fields in the thermal evolution of neutron stars

Deborah N. Aguilera

Tandar Laboratory, CAC. Comisión Nacional de Energía Atómica. Av. Gral. Paz 1499. 1650 San Martín, Buenos Aires, Argentina.
aguilera@tandar.cnea.gov.ar

(Work done in collaboration with José A. Pons and J. A. Miralles, University of Alicante, Spain)

Abstract. We investigate the influence of strong magnetic fields $B > 10^{13}$ G on the thermal evolution of neutron stars including the heating produced by the magnetic field decay in the crust. We present results of 2D cooling simulations considering an anisotropic thermal conductivity tensor and all the relevant neutrino emission processes in realistic neutron stars. We show that the inclusion of the magnetic field has important effects on the cooling: its presence affects significantly the temperature surface distribution and the evolution of these objects during both the early neutrino cooling era and the late photon cooling era. We conclude that to explain the observations properly, a more complex scenario than the generally assumed *standard cooling* scenario is needed and this work can be seen as a first step towards a consistent magnetothermal evolution of magnetized neutron stars.

1. Introduction

Observational data of thermally emitting isolated neutron stars (NSs) confirm that most of them have magnetic fields larger than 10^{13} G. Therefore, a theoretical description of the thermal evolution must not avoid the inclusion of the magnetic field effects.

The analysis of observational data (see reviews: Zavlin, 2007 and Haberl 2007) confirm the non-uniform distribution of the surface temperature of isolated NSs. The mismatch between the extrapolation to low energy of the fits to X-ray spectra, and the observed Rayleigh Jeans tail in the optical band (*optical excess flux*), cannot be addressed with an uniform temperature. Several simultaneous fits to multiwavelength spectra of RX J1856.5−3754 (Pons et al., 2002), RBS 1223 (Schwope et al., 2007), and RX J0720.4−3125 (Pérez-Azorín et al. (2006a) are explained by a small hot emitting area of about 10–20 km^2 and an extended cooler component.

It has been proposed that the non-uniform surface temperature distribution may be produced by crustal confined magnetic fields (Geppert et al., 2004, Pérez-Azorín et al., 2006b). The reason is that magnetic fields larger than 10^{13} G limit the movement of the electrons (heat carriers) in the direction perpendicular to the field resulting in a strong supression of the thermal conductivity and remaining almost unaffected along the field lines.

Another crucial point when including such large fields is that the field decay through Ohmic dissipation and Hall drift processes is very efficient. Therefore, the heat released in the crust (Joule heating) must be considered in the thermal evolution of a neutron star (Aguilera et al., 2008a). In this article we focused on the effects of field decay and Joule heating on the neutron star cooling. In particular, we compare our simulations with observational data of a sample of isolated NSs that are highly magnetized.

2. Cooling of neutron stars with magnetic fields

We have performed two–dimensional simulations by solving the energy balance equation that describes the thermal evolution of a neutron star (NS)

$$C_v \frac{\partial T}{\partial t} - \vec{\nabla} \cdot (\hat{\kappa} \cdot \vec{\nabla} T) = -Q_\nu + Q_{\rm J} \ , \tag{1}$$

where C_v is the specific heat per unit volume, Q_ν are energy losses by ν-emission, $Q_{\rm J}$ the heat released by Joule heating, and $\hat{\kappa}$ is the thermal conductivity tensor, in general anisotropic in presence of a magnetic field. In this equation we have omitted relativistic factors for simplicity. A detailed description of the formalism, the code, and results can be found in Aguilera et al. (2008a). The geometry of the magnetic field is fixed during the evolution. As a phenomenological description of the field decay, we have assumed the following law

$$B = B_0 \frac{\exp\left(-t/\tau_{\rm Ohm}\right)}{1 + (\tau_{\rm Ohm}/\tau_{\rm Hall})(1 - \exp\left(-t/\tau_{\rm Ohm}\right))} \ , \tag{2}$$

where B is the magnetic field at the pole, B_0 its initial value, $\tau_{\rm Ohm}$ is the Ohmic characteristic time, and $\tau_{\rm Hall}$ the typical timescale of the fast, initial Hall stage. In the early evolution, when $t \ll \tau_{\rm Ohm}$, we have $B \simeq B_0(1 + t/\tau_{\rm Hall})^{-1}$ while for late stages, when $t \geq \tau_{\rm Ohm}$, $B \simeq B_0 \exp(-t/\tau_{\rm Ohm})$. This simple law reproduces qualitatively the results from more complex simulations (Pons & Geppert, 2007) and facilitates the implementation of field decay in the cooling of NSs for different Ohmic and Hall timescales.

3. Joule heating governing the cooling

We present results of our cooling simulations for a 1.35 $M_\odot$ neutron star with a crustal confined magnetic field (see Aguilera et al., 2008a for model details), in which we have varied the parameters that describe the typical timescales for Ohmic dissipation and the fast initial decay induced by the Hall drift. In Fig. 1 we show the cooling curves at the magnetic pole (right panel) and equator (left panel) for different values of Joule parameters ($\tau_{\rm Ohm}, \tau_{\rm Hall}$): ($10^6$yr, 10^3yr), and (10^6yr, 10^4yr), represented by dashed and dash-dotted lines, respectively. For comparison, the solid lines show the evolution with constant field for the same initial field $B_0 = 5 \times 10^{14}$ G.

There is a large effect of the field decay on the temperature at the bottom of the envelope T_b: as a consequence of the heat released, it remains much higher than in the case of non–decaying magnetic field. The strong influence of the field

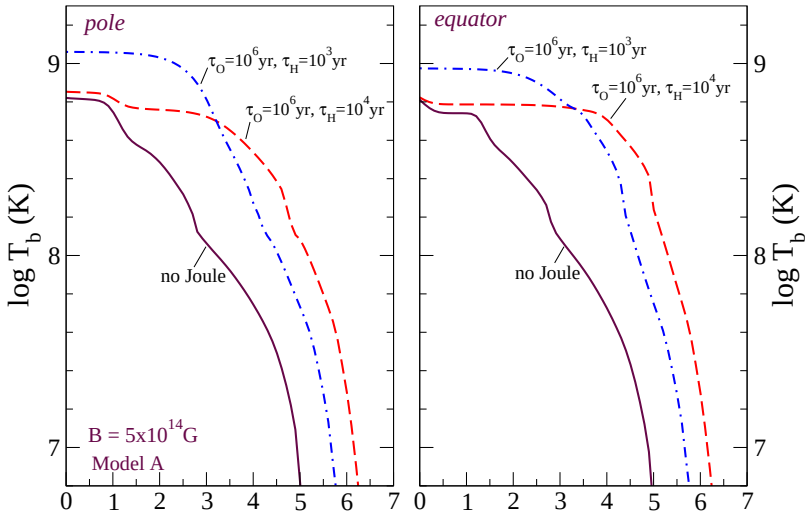

Figure 1. Cooling of strongly magnetized NSs with Joule heating for $B_0 = 5 \times 10^{14}$ G: T_b vs. t at the pole (left) and at the equator (right). Two pairs of Joule parameters $(\tau_{\rm Ohm}, \tau_{\rm Hall})$ are shown: $(10^6{\rm yr}, 10^3{\rm yr})$ with dashed lines, and $(10^6{\rm yr}, 10^4{\rm yr})$ with dashed-dotted lines, respectively. Without Joule effect is shown as solid line.

decay is evident for all parameters chosen. The temperature of the initial plateau is higher for shorter $\tau_{\rm Hall}$, but the duration of this stage with nearly constant temperature is also shorter. When $t = \tau_{\rm Hall}$, B has decayed to about $1/2B_0$ and 3/4 of the initial magnetic energy has been dissipated. After $t = \tau_{\rm Hall}$, T_b drops due to the transition from the fast Hall decay to the slower Ohmic decay.

There is a twofold insulating effect of tangential magnetic fields, as we can see from Fig. 1. First, in the absence of additional heating sources, it decouples low latitude regions from the hotter core resulting in lower temperatures at the base of the envelope. Second; if there is heat released in the crust, it prevents the extra heat to flow into the inner crust or the core where it is more easily lost in the form of neutrinos. Our simulations with Joule heating show systematically a hot equatorial belt at the crust–envelope interface. However, as discussed in Aguilera et al. (2008a), the *inverted temperature distribution* at the level of the crust is not necessarily visible in the surface temperature distribution because it is filtered by the magnetized envelope as we will see next.

In Fig. 2 we show the angular distribution of the surface temperature, T_s normalized to its value at the pole, $T_s^{\rm pole}$ corresponding to the simulations of Fig. 1. We show them for three different evolution times: $t = 10^4, 10^5, 10^6$ yr.

An analysis of the angular temperature distribution given in Fig. 2 shows the development of a middle latitude region hotter than the pole at relatively late stages in the evolution ($t \simeq 10^4, 10^5$ yr). This hotter area is found with a wide range of parameters, and it would have implications on the light curves of rotating NSs, that will differ substantially from the light curves obtained with a typical hot polar cap model.

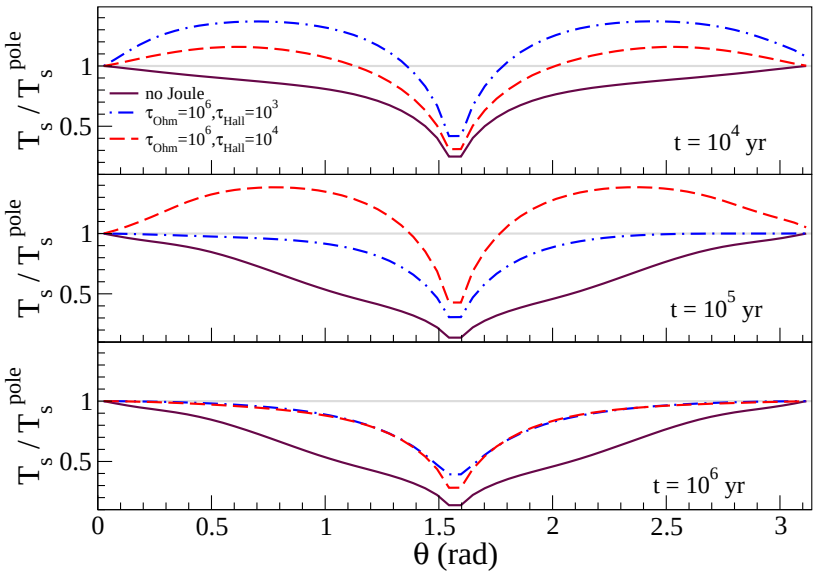

Figure 2. T_s normalized to $T_s^{\rm pole}$ vs. θ for simulations of Fig. 1.

4. Spin-down age of neutron stars

In general, the age of an isolated neutron star is calculated from the measurements of the rotational period P and its derivative $\dot{P}$. The so called *spin down age*, $t_{sd} = P/2\dot{P}$, is thus derived assuming that the lose of angular momentum is entirely due to dipolar radiation from a constant (in time) magnetic dipole. This model gives a reasonable approximation to the *true age* t if the magnetic field is constant. But in the case of a decaying magnetic field, $t_{\rm sd}$ can seriously overestimate t. A simple algebra shows that in the case of purely Ohmic decay

$$t = \frac{\tau_{\rm Ohm}}{2} \ln\left(1 + 2\frac{t_{\rm sd}}{\tau_{\rm Ohm}}\right). \tag{3}$$

In the case that a Hall–induced fast decay also occurs, Eq. (2) results in a large correction of $t_{\rm sd}$ as follows:

$$t_{\rm sd} = \tau_{\rm Hall}\ f(t)\ e^{2t/\tau_{\rm Ohm}} \left[f(t) - e^{-t/\tau_{\rm Ohm}} - \frac{\tau_{\rm Hall}}{\tau_{\rm Ohm}} f(t) \ln f(t)\right] \tag{4}$$

where $f(t) = 1 + \frac{\tau_{\rm Ohm}}{\tau_{\rm Hall}}(1 - e^{-t/\tau_{\rm Ohm}})$. This relation gives $t_{\rm sd} \gg t$ by several orders of magnitude for $t \gg \tau_{\rm Hall}$, as shown in Fig. 3. Therefore, we correct the cooling evolution time obtained in the simulations according to the prescription for the magnetic field decay in order to compare with the observations properly. A detailed comparison with observational sources is presented in Aguilera et al. (2008b) and is summarized in the next section.

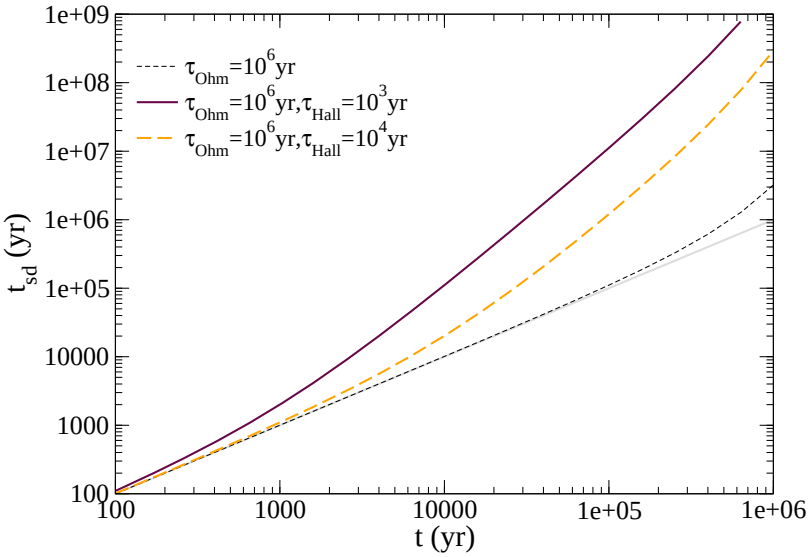

Figure 3. Spin down age ($t_{\rm sd}$) vs. *true age* (t) for a model with magnetic field decay. Results for two rates ($\tau_{\rm Ohm}, \tau_{\rm Hall}$) are shown: ($10^6$yr, 10^3yr) with solid lines and (10^6yr, 10^4yr) with dashed lines. The grey solid line represents $t_{\rm sd} = t$, and the short dashed line the purely Ohmic decay with $\tau_{\rm Ohm} = 10^6$ yr.

5. Comparison of cooling curves with observations

We compare in Fig. 4 our simulations with observational data of NSs covering about three orders of magnitude in magnetic field strength: from radio-pulsars ($B \simeq 10^{12}$ G) and isolated radio-quiet NSs ($B \simeq 10^{13}$ G) to recent magnetar candidates ($B \simeq 10^{14-15}$ G). The sources considered here are listed in Table 1 of Aguilera et al. (2008b), with corresponding references.

For most NSs, B is estimated by assuming that the lose of angular momentum is entirely due to dipolar radiation. The dipolar component is $B_d = 3.2 \times 10^{19}(P\dot{P})^{1/2}$ G, where P is the spin period in seconds, and $\dot{P}$ is its time derivative. In order to work with an homogeneous sample, we have included in the comparison only those objects for which $\dot{P}$ is available and the quoted magnetic field is B_d and discarded those sources for which B is inferred by other methods. For example, for a few radio-quiet isolated NSs B can also be estimated assuming that observed x-ray absorption features are due to proton cyclotron lines, but this gives the surface field, which is usually larger than the external dipolar component.

The reported temperatures are in most cases blackbody temperatures, except for low field radio-pulsars for which we take the temperature consistent with Hydrogen atmospheres following the criteria in Page et al. (2004). Nevertheless, there are some objects in which the estimate is an upper limit for the thermal component, like the Crab pulsar. This is also the case for some magnetars, which show large variations in the flux in the soft x-ray band on a timescale

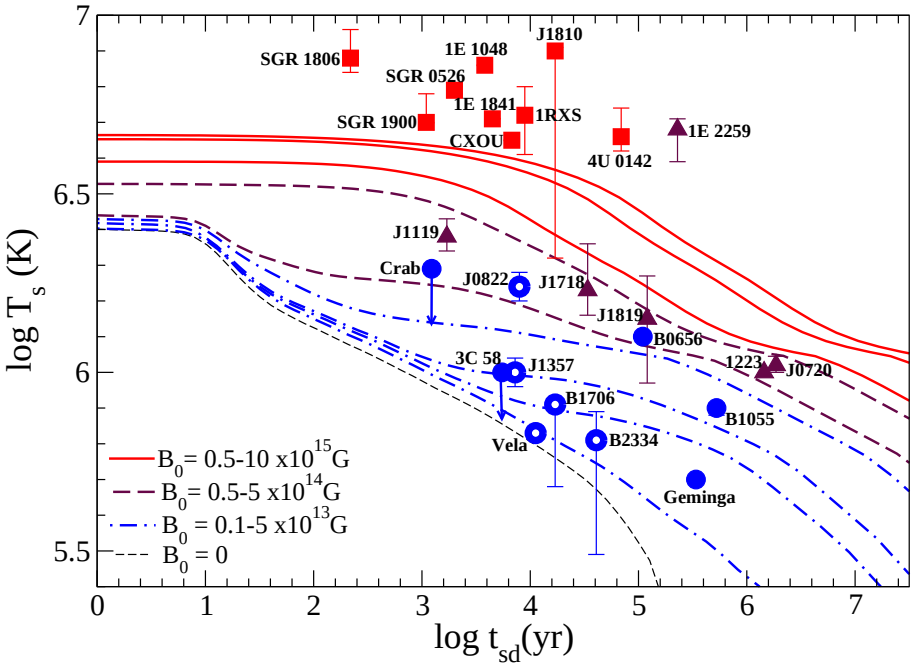

Figure 4. Cooling curves with corrected spin down age. Observational sources correspond to Table 1 of Aguilera et al. (2008b). Symbols identify sources with the same order of magnetic field: squares for magnetars (AXPs and SGRs, with $B \simeq 10^{14-15}$ G), triangles for radio-quiet isolated NSs (with $B \simeq 10^{13}$ G), and circles for radio-pulsars (with $B \simeq 10^{12}$ G). Open circles denote temperatures obtained from fits to Hydrogen atmospheres.

of a few years, indicating that the thermal component must be measured during quiescence and that the luminosity during their active periods is a result of magnetospheric activity.

The age of a NS is subject to a large uncertainty, but it can be estimated by the *spin-down age* ($t_{sd} = P/2\dot{P}$), provided that the birth spin rate far exceeds the present spin rate and B is considered constant. For some cases an independent *kinematic age* is available, which does not necessarily coincide with t_{sd}. As shown in Sec. 4., if one considers magnetic field decay, t_{sd} seriously overestimates the age t of the simulations. Therefore, we transform the cooling curves to plot T_s vs. t_{sd}, to include the temporal variation of the magnetic field.

In Fig. 4 our results show that the effect of high magnetic field ($B_0 \simeq 10^{14-15}$ G, solid lines) in the cooling is important from the very beginning of the NS evolution. The temperature reached is increased up to a factor of 5 in comparison with a non–magnetized model and can be kept nearly constant for about 10^4 years. The effect of Joule heating is very significant and may help to explain why magnetars are so hot (Kaspi, 2007): the high temperatures in the early epoch result in higher electrical resistivity and in an faster magnetic

field dissipation that releases the heat in the crust. In this picture, the thermal evolution of radio-quiet, isolated NSs could be represented either by NSs born with intermediate fields in the range of $B_0 = 10^{13}$-10^{14} G (dashed lines) or by magnetars in which the field has already decayed in a timescale of $\approx 10^{5-6}$ years. For intermediate field strengths, the initial effect is not so pronounced but the star can be kept much hotter than non-magnetized NSs from 10^4 yr to 10^6 yrs. For weakly magnetized NSs, radiopulsars with $B \simeq 10^{12}$ G, the effect of the magnetic field is small (dashed dotted lines) and they can satisfactorily be explained by non-magnetized models, with the exception of very old objects ($t > 10^6$ years), as discussed in Miralles et al. (1998).

6. Conclusions

The thermal evolution of a magnetized NS is strongly modified by the presence of magnetic fields. Therefore, to study the properties of NSs interior (e.g. EoS, neutrino processes, etc.) for objects with $B \geq 10^{13}$ through their cooling behaviour one should not neglect the magnetic field effects, that may be dominant in the evolution. This work could be seen as a first step towards a coupled magneto-thermal evolution and further investigations are needed include the evolution of the magnetic field geometry.

Acknowledgments. D.N.A would thanks the organizers of the "First La Plata International School" for the nice meeting and fruitful discussions. D.N.A. is member of the CONICET scientific staff.

References

Aguilera, D. N., Pons, J. A., & Miralles, J. A. 2008, A&A(in press), preprint[0710.0854]
Aguilera, D. N., Pons, J. A., & Miralles, J. A. 2008, ApJ, 673, L167
Geppert, U., Küker, M., & Page, D. 2004, A&A, 426, 267
Haberl, F. 2007, Ap&SS, 308, 181
Kaspi, V. M. 2007, Ap&SS, 308, 1
Miralles, J. A., Urpin, V., & Konenkov, D. 1998, ApJ, 503, 368
Page, D. et al. 2004, ApJS, 155, 623
Pérez-Azorín, J. F. et al. 2006a, A&A, 459, 175
Pérez-Azorín, J. F., Miralles, J. A., & Pons, J. A. 2006b, A&A, 451, 1009
Pons, J. A et al. 2002, ApJ, 564, 981
Pons, J. A., & Geppert, U. 2007, A&A, 470, 303
Schwope, A. D. et al. 2007, Ap&SS, 308, 619
Zavlin, V. E. 2007, preprint [astro-ph/0702426]

First La Plata International School, 2008
Compact Object and their Emission, 2009
Ileana Andruchow & Gustavo E. Romero, eds.

Evolutionary Studies of Cataclysmic Variables - The Recurrent Novae T Pyx

Helena Uthas

University of Southampton, Department of Physics and Astronomy, Highfield, Southampton SO17 1BJ, UK, and Nordic Optical Telescope, Apartado 474, E-38700 Santa Cruz de La Palma, Spain.
helena@not.iac.es

Abstract.

Standard evolutionary models for cataclysmic variables (CVs) predict that $\sim 70\%$ of the CVs should already have passed their minimum orbital period. However, few such systems are known, and some systems near the period minimum are having much higher accretion rates than can be explained by the conventional models. An example of such a system is the recurrent novae T Pyx.

Phase-resolved, optical spectroscopy of T Pyx was obtained with GIRAFFE, VLT with the aim to establish system parameters such as the masses of both components, by measuring the radial velocities of the narrow components in the Bowen blend as a function of orbital phase. The Bowen blend is assumed to arise from a fluorescence process originating from the irradiated front side of the secondary star (Steeghs and Casares 2002). Preliminary results of the observations are presented.

1. Introduction

1.1. Evolution of Cataclysmic Variables

Cataclysmic variables consist of a late-type secondary star that loses mass to a primary white dwarf. As long as the secondary remains near the Hydrogen-burning main sequence, the accretion process leads to a decrease in the orbital period of the system. However, due to the mass loss, the secondary will reduce both its mass and size, and its fate is to eventually become a degenerate brown dwarf. In this evolutionary phase the secondary will expand as a result of the continued mass loss, and the orbital period will increase (Warner 1995). Therefore, a CV is expected to go through a minimum period during its evolution. Observations indicate that the minimum orbital period for CVs is around 75 minutes (Knigge 2006).

There are several factors that can influence the evolution of cataclysmic variables. The systems undergo many nova eruptions; the secondary is losing mass, it is influenced by being tidally locked to the white dwarf, and its front side is irradiated by a hot white dwarf.

1.2. The Recurrent Novae T Pyx

T Pyx is a recurrent nova (RN) that accretes at a much higher rate than is expected for its short orbital period of 1.83 hours. It is the RN with the shortest

interval between the eruptions of about 22 years. The last eruption was in 1966, which means that T Pyx has passed its mean recurrence time by almost 20 years. The eruptive behavior of RNe compared to classical novae is thought to be due to a high mass-transfer rate in combination with a massive primary white dwarf, resulting in unusually frequent thermo-nuclear runaways on the surface of the white dwarf.

T Pyx contains an unusually luminous white dwarf, $L_{bol} \geq 10^{36}$ ergs^{-1} (Patterson et al. 1998), that has been heated by the nova eruptions. According to evolutionary theory, angular momentum loss and mass transfer in systems with orbital periods below $P_{orb} \sim 3$ hours are supposed to be driven by gravitational radiation. However, when this theory is applied to T Pyx, a significantly lower luminosity is predicted, $\sim 10^{32}$ ergs^{-1} (Knigge et al. 2000). This implies that another mechanism must be found to explain its high luminosity. Nuclear burning on the surface of the white dwarf could be part of an explanation, and it has been suggested that T Pyx has properties similar to the super soft sources (SSS). These systems consist of a slightly evolved secondary that has a mass $M_2 > 1.3\ M_\odot$ (Patterson et al. 1998). But there are many reasons why T Pyx does not fit SSS models, for instance due to its short orbital period. It has therefore been suggested that the system is part of a subtype, a wind-driven super soft source. The surface of the secondary is strongly irradiated by X-ray emission from the white dwarf, and this could result in the formation of a wind that is leading to a high accretion rate.

Such high mass-transfer in combination with a short orbital period can be devastating for the system as it could lead the white dwarf to exceed the Chandrasekhar limit and the system to become a supernovae type Ia. If it turns out that other systems are also entering such a phase, it could possibly explain why we do not see so many systems at the period minimum (Knigge et al. 2000).

2. Multi-Fibre Spectroscopy of T Pyx

Phase-resolved optical spectroscopy of T Pyx was obtained with the VLT instrument GIRAFFE (on FLAMES) in 2004 and 2005. There is data from 5 nights spread out in time over two months and the total observing time is about 8.5 hours. The data was taken in the integrated field-unit mode (IFU), so the contribution from the nova shell could be distinguished from T Pyx itself. The fibre system Argus was used. It consists of 317 fibres in total where 15 fibres are pointed to sky, and 5 fibres are pointed to a calibration unit. The grating order 4 was used, which gives a resolution of R=12000. The wavelength range was chosen between 4501 - 5078 Å, so the emission-line spectrum would include the Bowen blend at 4645 - 4650 Å, and the HeII at 4686 Å.

The initial steps in the data reduction were performed using the ESO pipeline for GIRAFFE. The basic functions of the pipeline are to provide master calibration data, dispersion solutions and reduced science frames. The output from the pipeline is a rebinned and reduced image that is flat-fielded and wavelength calibrated. In the image, one column corresponds to the signal from a single fibre. To extract the spectrum from the desired fibres and to correct for the contribution from the sky background and cosmic rays, the output from the pipeline was processed further in IRAF.

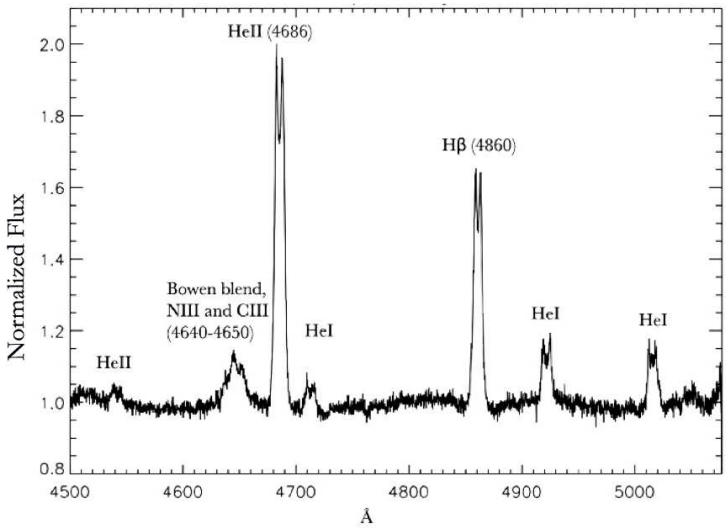

Figure 1. T Pyx has a highly excited emission-line spectrum that is unusual when compared to conventional CVs. The front side of the secondary is irradiated by the white dwarf, giving rise to a fluorescence process that can be seen in the spectrum as the Bowen blend at $\sim$ 4640 Å. The Bowen blend consists of several narrow components of NIII and CIII and has been found in other high-accretion rate CVs.

3. Results

3.1. The Spectrum

The data analysis package MOLLY was used to normalize the spectra using a third-order spline fit to the averaged spectrum. The normalized and averaged spectrum can be seen in Fig. 1. The Bowen blend is clearly present at $\sim$ 4650 Å, and it is possible to distinguish about three components in the blend. The presence of sub-peaks in the Bowen blend in the average spectrum could indicate that they do originate from the secondary star, since features from the disc are expected to be smeared out by orbital effects. However T Pyx is a low-inclination system and disc features will not be that broad compared to systems with higher inclination. The double-peaked HeII line can be seen at $\lambda \sim 4686$ Å, as well as emission from Hβ and HeI. The widths of the arc lines in the calibration frames are about 2 pixels, which give a spectral resolution of 0.2 Å. This corresponds to a resolution in velocity of about 26 km/s.

In order to get a visual look at the orbital modulations, trailed spectrograms were plotted in MOLLY for the HeII line and the Bowen blend. The trailed spectrograms were constructed from binning all 141 spectra into 20 phase bins and are shown repeated over two orbital cycles in Fig. 2. The double peaked HeII line shows a clear orbital modulation. It is possible to distinguish three sub-peaks in the Bowen blend, all showing weak signatures of the orbital modulation.

Figure 2. Trailed spectrograms were constructed by binning all 141 spectra into 20 phase bins and are shown here repeated over two orbital cycles. The spectrograms were constructed for the purpose of studying the orbital modulation for (*Left:*) the Bowen blend and (*Right:*) the HeII line.

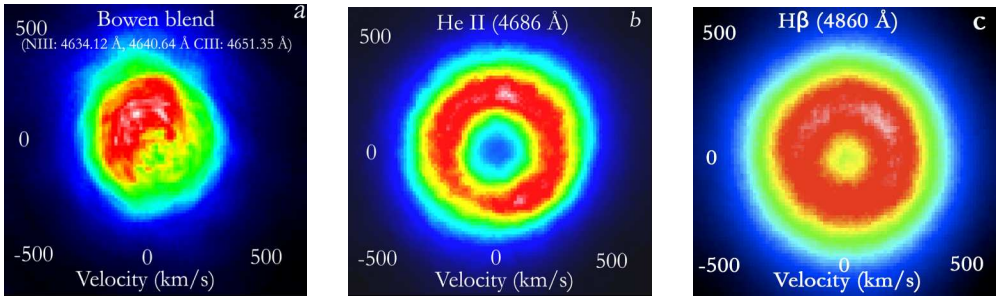

Figure 3. The Doppler maps were constructed in MOLLY from the phase binned and velocity binned data. The velocity resolution in the maps is 20 km/s/pixel.

3.2. Doppler Mapping

Doppler tomography (Marsh and Horne 1988) is used to determine the origin of line emission in a system by mapping the data on a radial velocity scale. Maps were constructed for the HeII line, the Hβ line and the Bowen blend. The Doppler map for the HeII line shows emission from the whole disk, but the emission is clearly asymmetric which, e.g., is not seen in the map for the Hβ line. The Doppler map for the Bowen blend shows a more localized but still extended emission. This emission might be identified with emission from the secondary and the accretion stream, where the low signal-to-noise of the Bowen blend probably causes this emission to appear relatively diffuse in the map (see Fig. 3).

4. Future Work

The aim of the observations was to establish the system parameters by studying the kinematics of the emission lines. Radial velocity curves for the HeII and the Hβ lines have been constructed by using the double-Gaussian technique (Schneider and Young 1980). Future work involves studying these curves in more detail. The method was not applied to the components in the Bowen blend due to the low signal-to-noise in the individual spectra. The construction of Doppler maps is therefore an important tool when studying the Bowen blend.

Future work also involves the study of other systems that do not seem to follow the evolutionary models. It is obvious that we need to gain more

knowledge to be able to understand these systems and to explain why we do not find so many systems at or beyond the period minimum.

Acknowledgments. I would like to thank all the teachers for the inspiring lectures and the local organizing committee for making the First La Plata International School a memorable experience.

References

Knigge, C. 2006, MNRAS, 374, 484
Knigge, C., King, A. R., & Patterson J. 2000, A&A, 364, 61
Marsh, T. R., & Horne K. 1988, MNRAS, 235, 269
Patterson, J. et al. 1998, PASP, 110, 380
Schneider, D. P., & Young, P. 1980, ApJ, 238, 946
Steeghs, D., & Casares, J. 2002, ApJ, 560, 273
Warner, B. 1995, Cataclysmic Variable Stars, Cambridge, Cambridge Univ. Press

First La Plata International School, 2008
Compact Object and their Emission, 2009
Ileana Andruchow & Gustavo E. Romero, eds.

Formation and evolution of helium white dwarfs in the old metal-rich open cluster NGC 6791

Alejandra D. Romero, Jorge A. Panei & Leandro G. Althaus

Facultad de Ciencias Astronómicas y Geofísicas, UNLP.
Instituto de Astrofísica La Plata (CCT La Plata, CONICET).

Abstract.

NGC 6791 is both the oldest ($\sim$ 8 Gyr) and most metal-rich ([Fe/H] $\sim$ +0.4) open cluster in our Galaxy. This cluster contains a large blue straggler population, and an extremely blue horizontal branch. In addition, it has been shown that two-thirds of the NGC 6791 members white dwarfs have masses below $\sim 0.46 M_{\odot}$ at which helium is ignited in the core. In particular extreme horizontal branch stars, and also low mass helium white dwarf, can be formed as a result of increased mass loss in post main sequence evolutionary stages, since mass loss is much more efficient in high metallicity environments.

In this work we explore the formation and evolution of low mass helium white dwarfs in a high metallicity environment. We compute full evolutionary sequences from the beginning of the main sequence to the white dwarf cooling curve, considering the single stellar evolutionary channel with strong mass loss on the red giant branch.

1. Introduction

NGC 6791 is one of the richest open clusters in the galactic disk, possibly the oldest and possesses a significantly supersolar metallicity. Because of these characteristics it has been the target of several studies. The most recent ones, indicate that the age of NGC 6791 is $\gtrsim$ 8 Gyr, the [α/Fe] is solar (Origlia et al. 2006), and the metallicity is [Fe/H]=+0.3-+0.5 (Kaluzny 1990; Gratton, et al. 2000; Origlia, et al. 2006; among others). Therefore, NGC 6791 is both the oldest and most metal-rich open cluster in our Galaxy (Friel & Janes 1993). This cluster is also one of the most populous open star clusters, with a mass higher than 4000 $M_{\odot}$ (Carraro, et al. 2006) and it is relatively nearby ($d \sim 4$ kpc- Chaboyer, Green & Liebert 1990).

The Color-Magnitude diagram (CMD) of NGC 6791 shows a large blue straggler population, and both a red giant clump and an extremely blue horizontal branch (see Kalirai, et al. 2007- Fig. 3). The red giant clump represents a phase of core helium burning following the helium flash at the tip of the cluster's red giant branch. The extreme horizontal branch stars are also burning helium in their cores but have very likely formed as a result of increased mass loss in post main sequence evolutionary phases, suffering a delay in the ignition of helium in the core until they have reached higher effective temperatures. The enhanced mass loss could be driven by the high metallicity of the cluster (Faulkner 1972, D'Cruz, et al. 1996). The extreme horizontal branch stars are cluster counter-

parts of the subdwarf B and subdwarf O stars that are found in the galactic field. Finally, there is also a population of white dwarf candidates. The results obtained by Kalirai, et al. (2007) suggest that the white dwarf population of NGC 6791 is indeed notably under massive ($< M > = \ 0.43 \pm 0.06 M_{\odot}$) when compared to other star clusters and also to the field distribution.

Since white dwarfs are cooling with age, this objects work as clocks to measure the clusters age. The technique of determining ages from white dwarf cooling theory successfully reproduces ages independently measured using the main sequence turnoff technique in the six other open clusters, and two globular clusters (von Hippel 2005; Hansen et al. 2004, 2007). However Bedin, et al. (2005), fitting standard white dwarf models (carbon-oxygen core) to the observed luminosity function, conclude that the white dwarf cooling age of NGC 6791 is 2.4 Gyr. This value corresponds to a factor of three less than the well measured main sequence turnoff age.

As possible solution Hansen (2005) suggested that, instead of the standard white dwarf models, helium core white dwarf models should be used in the fitting. In addition, this author concluded that the white dwarf luminosity function for NGC 6791 should be bimodal: with a strong peak corresponding to helium core white dwarfs and a second peak, at fainter magnitudes, resulting from traditional carbon-oxygen white dwarfs which did pass through the horizontal branch phase. The helium core white dwarf population could be formed following a single evolutionary channel involving significant mass loss on the red giant branch, leading to a final mass below the critical mass needed to ignite helium in the core of the star. Hence, the progenitors of these white dwarfs avoided the helium flash – flash manqué stars – and therefore the cores of the white dwarfs are composed of helium and not carbon and oxygen.

Following this trend, we begin to study the formation and evolution of helium core white dwarfs in supersolar metallicity enviroments. We computed full evolutionary sequences of helium core white dwarfs taking into account the alternative energy sources present in the white dwarf phase besides the thermal cooling of the degenerate core. In particular, we consider the occurrence of nuclear flashes due to instabilities in the hydrogen burning shell that surrounds the core.

In Sec. 2. we briefly describe the input physics of the evolutionary code and the performed computations. In Sec. 3. we present and describe our results. Finally, in Sec. 4. we summarize our main results and enumerate some perspectives.

2. Imput physics and computational details

We compute four complete evolutionary sequences starting from the main sequence, through the red giant branch, to the white dwarf phase. These sequences were computed using the LPCODE evolutionary code (Althaus, et al. 2003, 2005). The code is based on an elaborated treatment of the chemical abundance changes that take place along the whole evolution, changes that are described via a time-dependent scheme for the simultaneous treatment of nuclear evolution and mixing process due to convection and diffusive overshoot. LPCODE employs OPAL radiative opacities (Iglesias & Rogers 1996) complemented at

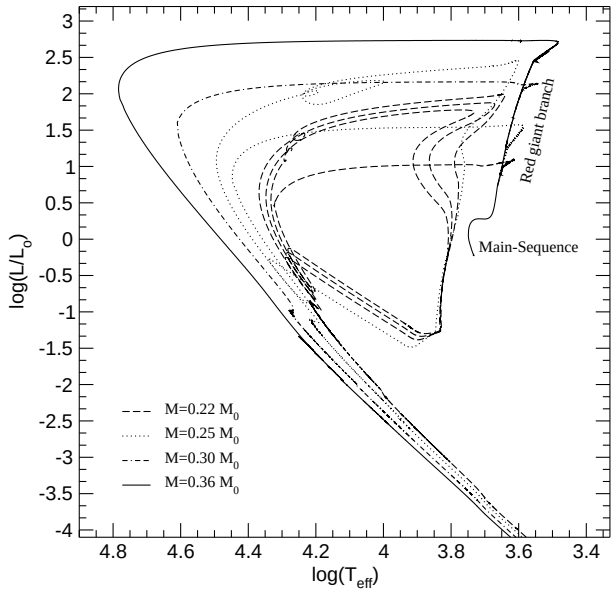

Figure 1. Evolutionary tracks with $Z = 0.030$ from the main sequence to the white dwarf cooling curve. The sequences are labeled according to the mass of the remnant at the white dwarf phase.

low temperatures with the molecular opacities of Alexander & Ferguson (1994). Neutrino emission rates are taken from the works of Itoh and collaborators.

In this work, a single seed sequence for a 1 $M_\odot$ model with $Z = 0.030$ was evolved from the zero age main sequence through the core hydrogen burning and the red giant branch until the white dwarf cooling curve. In order to obtain flash manqué star models, the mass loss rate was artificially enhanced during the red giant branch phase. By varying the mass loss rates we obtained white dwarf models with different masses. The final masses of our remnants at the white dwarf stage are 0.22, 0.25, 0.30 and 0.36 $M_\odot$. Additionally, we compute a single evolutionary sequence with metallicity $Z = 0.038$ by using the same technique, with a mass of 0.36 $M_\odot$ at the white dwarf phase.

3. Results

The complete evolutionary tracks with metallicity $Z = 0.030$ are depicted in Fig. 1 in the $\log(T_{\rm eff}) - \log(L_*/L_\odot)$ plane. As can be seen from this figure, the lower mass sequences suffer nuclear shell flashes due to instabilities in the hydrogen burning-shell that surrounds the helium core. As is well known, hydrogen-shell burning in low mass white dwarfs can become instable, leading to thermonuclear flashes by means of the CNO cycle. On the other hand, the most massive sequences do not experience nuclear flashes during he white dwarf stage. This is in agreement with the fact that thermonuclear flashes do not occur for stellar masses larger than $\sim 0.30\,M_\odot$ when diffusion processes are not considered (Panei, et al. 2007).

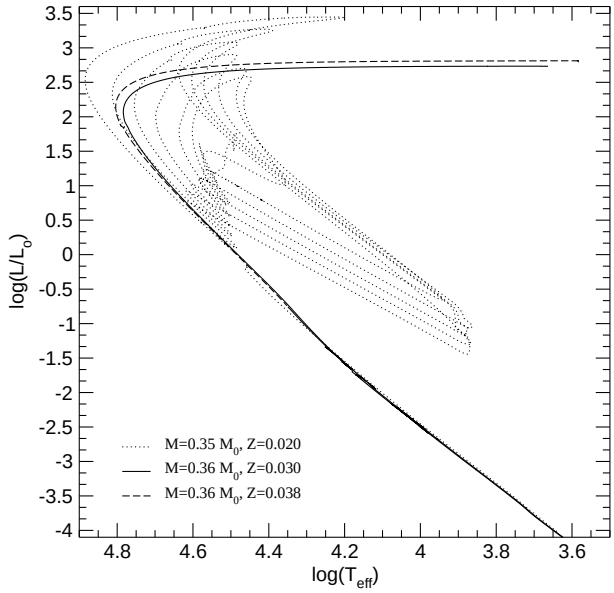

Figure 2. Evolutionary tracks with $M_* = 0.36 M_\odot$ and for $Z = 0.030$ and $Z = 0.038$. An evolutionary track corresponding to a sequence with solar metallicity and $M_* = 0.35 M_\odot$ is also depicted (Panei , et al. 2007).

In Fig. 2 we depicted the sequences with 0.36 $M_\odot$ and metallicities Z=0.030, 0.038 in the $\log(T_{\rm eff}) - \log(L_*/L_\odot)$ plane. These two evolutionary tracks overlap in the cooling phase for luminosities below ~ 0. However, the sequences defer in the cooling times. At lower metallicities the stellar atmosphere is more transparent to radiation coming from the interior of the star. Thus, the sequence with lower metallicity will lead to a shorter cooling time. In this case, the difference in Z seems to be too small to note a measurable age difference for a fixed luminosity value. At a $\log(L_*/L_\odot) \approx -3.5$ the age difference is around 10^8 yrs.

As we already mentioned, during the white dwarf stage, there is still a nuclear source, being the hydrogen burning-shell that surrounds the core. In order to account for the delay produced by this shell-source in the cooling, we recalculated the white dwarf phase for the sequence with $Z = 0.030$ and $M = 0.36\, M_\odot$ but this time we artificially turned off the nuclear burning at a given luminosity. As a result we obtained a sequence which energy is given solely by the kinetic energy of the ion gas in the core. In Fig. 3 we depict the luminosity in a logarithmic scale as a function of the white dwarf age in Gyr. Clearly, the sequence with a residual shell source cools more slowly since it posses an additional energy source, contrary to the one where the nuclear burning was suppressed. For example, for $\log(L_*/L_\odot) \approx -3.5$ the ages differ in ~ 3 Gyrs. Thus, for an accurate age measure using white dwarf cooling sequences it is necessary to consider the presence of residual nuclear sources, in this case, the hydrogen shell source.

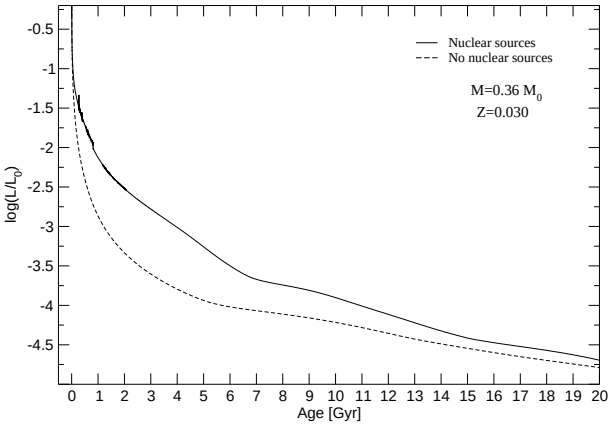

Figure 3. Luminosity ($\log(L_*/L_\odot)$) as a function of the white dwarf age (Gyr) for two sequences of $0.36\,M_\odot$ and $Z = 0.030$. Solid line: sequence with active residual nuclear sources. Dashed line: sequence where nuclear burning was artificially turned off.

4. Summary and perspectives

In this work we study formation and evolution of helium core low mass white dwarfs with supersolar metallicity. In particular we analyzed the impact of an hydrogen burning shell on the cooling times. We found a delay of ~ 3 Gyr in the cooling time when this energy source is considered in the calculations.

This is the first step to obtain white dwarf models, coming from complete evolutionary sequences, necessary to perform age measurements using the white dwarf cooling technique. In particular to measure the age of the open cluster NGC 6791. In the future we will improve the white dwarf star models by including a treatment of elemental diffusion in the outer layers and the influence of alternative energy sources, like gravitational settling of ^{22}Ne in the white dwarf core. We also will increase the studied mass range for the metallicity values considered.

Acknowledgments. This research has been partiallysupported by the PIP 6521 grant from CONICET. This research has made use of NASA's Astrophysics Data System.

References

Alexander, D. R., & Ferguson, J. W. 1994, ApJ, 437, 879
Althaus, L. G., et al. 2003, A&A, 404, 593
Althaus, L. G., et al. 2005, A&A, 435, 631
Bedin, L. R. 2005, ApJ, 624, L45
Chaboyer, B., Green, E. M., & Liebert, J. 1999, AJ, 117, 1360
D'Cruz, N. L., et al. 1996, ApJ, 466, 359
Faulkner, J. 1972, ApJ, 173, 401
Friel, E. D., & Janes, K. A. 1993, A&A, 267, 75

Gratton, R., et al. 2006, ApJ, 642, 462
Hansen, B. M. S., et al. 2004, ApJS, 155, 551
Hansen, B. M. S. 2005, ApJ, 635, 522
Hansen, B. M. S., et al. 2007, ApJ, 671, 380
Iglesias, C. A., & Rogers, F. J. 1996, ApJ, 464, 943
Kalirai, J. S., et al. 2007, ApJ, 671, 748
Kaluzny, J. 1990, MNRAS, 243, 492
Origlia, L., et al. 2006, ApJ, 646, 499
Panei, J. A., et al. 2007, MNRAS, 382, 779
von Hippel, T. 2005, ApJ, 622, 565

First La Plata International School, 2008
Compact Object and their Emission, 2009
Ileana Andruchow & Gustavo E. Romero, eds.

Are neutron stars hybrid stars?

A. R. Turlione & D. N. Aguilera

Tandar Laboratory CNEA, Av. Gral Paz 1499, 1650 San Martin, Argentina, turlione@tandar.cnea.gov.ar

Abstract. We investigate the hypothesis that some compact stars might actually be *hybrid stars* composed by a hadronic shell and an ultra-dense quark matter core. We study the structure of neutron stars using dense matter equations of state under the constraints of charge neutrality and beta-equilibrium. We obtained stable hybrid stars configurations compatible with observational data of mass and radius of compact objects.

1. Introduction

Neutron stars are the most compact stellar objects known and therefore extraordinary laboratories for dense matter properties. Neutron stars structure depends on the nature of the equation of state, which is not well understood in dense matter. At several times nuclear matter density nucleon cores start to overlap loosing their identity and quark degrees of freedom become important. It is thought that the density in the inner core of neutron stars can reach those extreme values, thus a compact star might be actually a *hybrid star* composed by an hadronic shell and a quark matter core (Lattimer & Prakash, 2001).

The presence of quark matter in a neutron star core is an open issue in compact objects physics. Several works study how the presence of quark matter core could affect the mass-radius relationship of a compact star (Burgio & Plumari, 2008; Schaffner-Bielich, 2005; Alford et. al, 2007). The maximum mass is one of the most sensitive physical quantities to the presence of quark matter, and it has been found that the presence of a quark core lowers the maximum mass (Lattimer & Prakash, 2001). Nevertheless it is very difficult to find venues from astrophysical observations that could unambiguously distinguish hybrid stars from ordinary neutron stars. Other aspects such as thermal evolution, pulsar glitches dynamics or quasiperiodic variability could provide astrophysical constraints on the dense matter equation of state (EoS). However some of these analyses rely on two of the most uncertain properties of astrophysical objects: their distances and ages. To date, predictions based on observations indicate that the existence of hybrid stars cannot be ruled out, but neither favored (Özel, 2006; Alford et. al, 2007).

In this article we study qualitatively the phase transition from nuclear matter to quark matter inside neutron stars and discuss about the existence of hybrid stars. We obtain that our results for those stars are compatible with observations and theoretical constraints. The paper is organized as followed: in Section 2 we briefly review the models for nuclear and quark matter EoSs used

and present phase transitions using the Maxwell construction. In Section 3 we present results for hybrid stars, and finally, in Section 4 we draw our conclusions.

2. Dense matter equations of state

2.1. Nuclear matter for compact stellar objects

We use here a relativistic mean field approach to model nuclear matter in which the nucleons interact via exchange of mesons: scalar σ and vector ω with masses m_σ, m_ω, respectively (Glendenning, 2000). The Lagrangian for the short-range interaction of fermions fields $\psi(x)$ is given by

$$L_{\rm int} = g_\sigma \sigma(x)\overline{\psi}(x)\psi(x) - g_\omega \omega_\mu(x)\overline{\psi}(x)\gamma^\mu\psi(x) \ , \tag{1}$$

where the coupling constants g_σ/m_σ and g_ω/m_ω are determined by the extrapolation from symmetric nuclear matter properties: the binding energy $BE = -16$ MeV at the nuclear saturation density $n_0 = 0.15$ fm^{-3} (Glendenning, 2000). The pressure and the energy density of the system are:

$$P = -\frac{1}{2}m_\sigma^2\sigma^2 + \frac{1}{2}m_\omega^2\omega^2 + \frac{1}{3}\frac{2}{\pi^2}\int_0^{k_f}\frac{k^2}{\sqrt{k^2+m^*}}k^2dk \tag{2}$$

$$\epsilon = \frac{1}{2}m_\sigma^2\sigma^2 + \frac{1}{2}m_\omega^2\omega^2 + \frac{2}{\pi^2}\int_0^{k_f}\sqrt{k^2+m^*}k^2dk \tag{3}$$

where the equilibrium values σ and ω are determined by minimizing the energy respect to the fields. The nucleon effective mass $m^* = m_N - g_\sigma\sigma$ is reduced in comparison to the free nucleon mass m_N owing to the scalar field.

The single-particle Fermi energy defines the corresponding chemical potential μ. In stellar matter chemical potentials of particle species are related by the condition of weak interaction equilibrium ($n+\nu_e \leftrightarrow e+p$) and charge neutrality,

$$\mu_n = \mu_e + \mu_p \quad , \quad \frac{k_p^3}{3\pi^2} = \frac{k_e^3}{3\pi^2} \tag{4}$$

where k_i is the Fermi momentum of the particle i. Since we are considering low temperature approximation, neutrinos are not trapped and $\mu_{\nu_e} = 0$.

2.2. Quark matter equation of state

At high enough density quark degrees of freedom become important and quark matter could appear in the core of neutron stars. To describe quark matter we use the MIT bag model, based on the idea of a gas of free quarks confined in colorless zones. The pressure and energy density in the bulk quark phase containing *up* (u), *down* (d) and *strange* (s) quarks are due to the kinetic energy density of quarks $E(k)$ and to a negative *Bag pressure* B. At zero temperature,

$$P = \sum_f \frac{1}{3}\frac{\gamma_f}{2\pi^2}\int_0^\infty k\frac{\partial E_f(k)}{\partial k}(n(k,\mu_f)+n(k,-\mu_f))k^2dk - B, \tag{5}$$

$$\epsilon = \sum_f \frac{\gamma_f}{2\pi^2}\int_0^\infty E_f(k)(n(k,\mu_f)+n(k,-\mu_f))k^2dk + B, \tag{6}$$

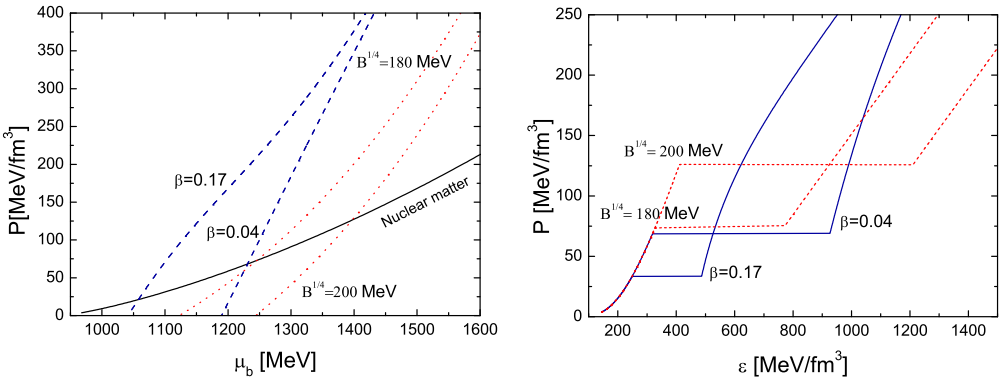

Figure 1. Maxwell construction. Left: Pressure vs. baryon chemical potential. Right: Pressure vs. energy density. Dotted lines are for constant B and solid lines for $B(\rho)$.

where $n(k,\mu)$ is the Fermi distribution, and $\gamma_f = 2_{spin} \times 3_{\rm color}$ is the degeneracy factor for each flavor $f = u, d, s$. The constant B represents the energy density difference between the perturbative vacuum and the true vacuum.

The quark matter EoS is constructed under conditions of beta-equilibrium and charge neutrality:

$$\mu_d = \mu_u + \mu_e, \quad \mu_s = \mu_d, \tag{7}$$

$$\sum_f q_f \frac{k_f^3}{3\pi^2} - \frac{k_e^3}{3\pi^2} = 0 \tag{8}$$

where q_f is the electric charge of the flavor f.

The value of B cannot be fixed directly from neither from dense matter theory nor from neutron star observables and thus remains as a free parameter. Nevertheless, we can constraint its value from particle phenomenology, introducing a *density-dependent Bag constant* $B(\rho)$ (Maieron et al., 2004),

$$B(\rho) = B_\infty + (B_0 - B_\infty) \exp\left[-\beta(\frac{\rho}{\rho_0})^2\right] \tag{9}$$

The parameters $B(0) = B_0 = 400$ MeVfm^{-3} and $B(\infty) = B_\infty = 50$ MeVfm^{-3} are fixed in order not to have a transition to symmetric nuclear matter below $3-4\,n_0$ with a fast decrease up to $6-7\,n_0$ where a phase transition to strange quark matter is expected from quark-gluon plasma formation in heavy ion collision at CERN (Heinz et al, 2001).

In Fig. 1 (left panel) we show quark matter EoSs: P versus baryon chemical potential, μ_b, for different values of constant B (dotted lines) and parametrizations of $B(\rho)$ (dashed lines). The solid line is the nuclear matter EoS presented in Sec. 2.1.. Above a certain density (or μ_b), quark matter EoSs have larger values of P than the nuclear matter EoS and a phase transition takes place.

2.3. Phase transition in dense matter

To perform the phase transition from nuclear to quark matter, we adopt the Maxwell construction, in which we equal μ_b and P in both phases,

$$\mu_b^N = \mu_b^Q, \quad P^N = P^Q \tag{10}$$

where superscripts N and Q denote (nuclear) and (quark) phases, respectively.

In Fig. 1 (right panel) we show P vs. ϵ and corresponding phase transitions; at the transition line P is constant, but there is a jump in ϵ and consequently in the particle composition. An EoS is termed soft (stiff) when the ratio of P to ϵ is small (large). For constant B (dotted lines) the transition takes place at relatively large values of P due to the stiffness of the EoS: the larger the pressure, the bigger the jump.

3. Structure of hybrid stars

Given the EoS we solve Tolman-Oppenheimer-Volkoff (TOV) equations and calculate neutron stars configurations. TOV equations uniquely determine the structure of the star, in particular its mass and radius, for a given central density.

We study three classes of stars: pure neutron stars (NSs), made purely of nuclear matter, quark stars (QSs) made entirely of quark matter, and hybrid stars (HSs), composed by an hadronic shell and a quark matter core. We analyze their maximum mass, $M_{\max}$, and characteristic radius, R. The value of $M_{\max}$ is defined by the stiffness of EoS, soft (stiff) EoSs lead to more (less) compact stars with smaller (larger) $M_{\max}$. Moreover, $M_{\max}$ is very sensitive to the EoS at supranuclear density, whereas R depends on the EoS in the vicinity of n_0 (Lattimer & Prakash, 2001). A necessary condition for stellar stability is $dM/dn > 0$ and neutron stars likely become unstable when they reach $M_{\max}$. In Fig. 2 three classes of star configurations are shown with theoretical and observational constraints. The light grey region on the top left is excluded by general relativity ($R > 2\,GM/c^2$), the dark grey region is forbidden by finite pressure ($R > 2.25\,GM/c^2$), and the grey region is excluded by causality ($R > 2.9\,GM/c^2$). The grey region on the botton right cannot be accesed by the maximum rotation frequency (716 Hz) of the J1748-2446ad pulsar (Lattimer & Prakash, 2007). The region inbetween dotted lines indicate the dispersion of masses measured in binary systems (Lattimer & Prakash, 2007). The dash-dotted line is the redshift $z = 0.35$ measured in the active X-ray buster EXO 0748-676 (Cottam et al., 2002), although this value has been put into question (Sidoli et al., 2005). The solid curve corresponds to NSs, and dashed curves are QSs configurations. Short dashed curves are HSs for $B = B(\rho)$, and dotted curves are for B constant.

A comparison between QSs and NSs shows some fundamental differences. First, QSs reach lower values of $M_{\max}$ because quark matter EoSs are softer than nuclear matter EoSs. The larger B, the softer the EoS, the smaller $M_{\max}$. Second, in the case of QSs, M and R become smaller when the central density, n_c, decreases while for NSs, R increases when M decreases making the star less compact. This is because QSs are self-bound stars (bound only by the strong interaction) while NSs are gravitationally bound.

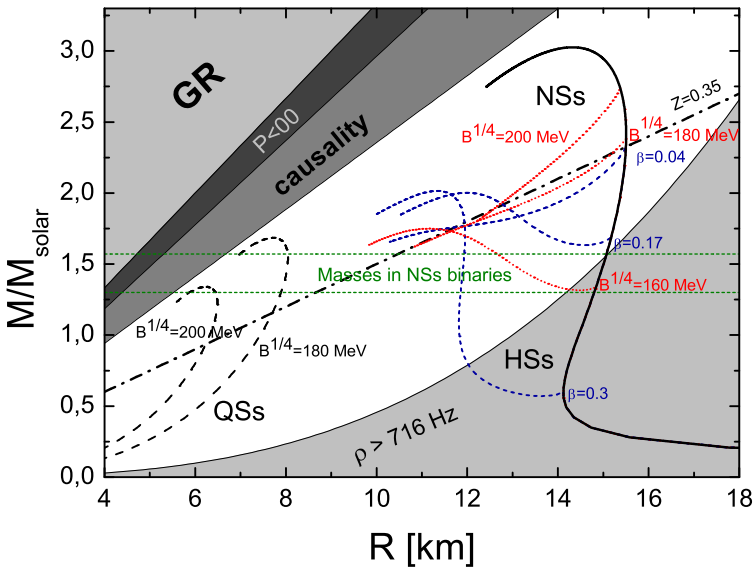

Figure 2. Mass-radius for neutron star configurations. Dashed curves are quark stars, solid curves are ordinary neutron stars. Short dashed and dotted curves are hybrid stars. Grey regions are theoretical and observational constraints.

HSs have lower $M_{\max}$ than NSs since phase transitions to quark matter result in a softening of the EoS. Turn-off points from the NSs stability curve indicate the change of EoS from nuclear to quark matter, and hence quarks matter core presence. When the transition occurs at relatively low density, the quark core occupies a large volume of the star, as for $\beta = 0.3$ and $B^{1/4} = 160$ MeV cases. In contrast, when this happens at high density, hybrid stars become unstable and the quark core do not take place. We got stable HSs for values of $\beta = 0.3 - 0.17$ and low B ($B^{1/4} < 160$ MeV).

In Fig. 3 we see the variation of the neutron star and quark core radius (left panel) and mass (right panel) with n_c for $\beta = 0.17$ and $\beta = 0.3$. Solid lines are NSs and dotted lines are HSs configurations. Dashed lines show corresponding values for the quark core. Triangles indicate $M_{\max}$ for stable configurations and circles denote corresponding radii, R^*. The mass (radius) of the quark core become larger as the total value increases (decreases) until the star becomes unstable right after it reaches $M_{\max}$ (R^*). As we show, the quark core could occupy a significant percentage of the star volume.

Finally, we note that all studied stars (NSs, HSs and QSs) show configurations consistent with observational data. Therefore, to distinguish if neutron stars are actually hybrid stars or ordinary neutron stars, further information from other physical aspects such as cooling (Aguilera et al., 2008), magnetic evolution (Pons et al., 2007), rotation (Stejner, 2008), etc. is needed.

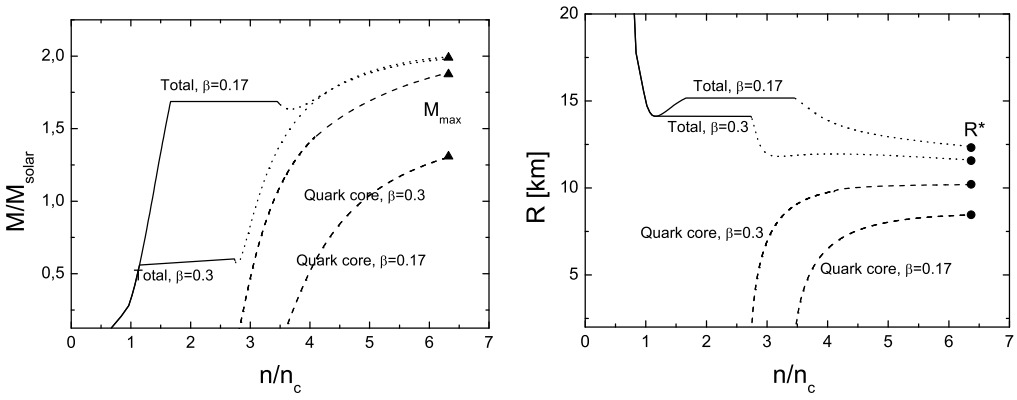

Figure 3. Left panel: total and quark core mass of neutron stars vs. central number density n_c. Right panel: Same for the radius.

4. Summary and perspectives

We present a qualitatively study of dense matter equations of state and investigate hybrid star configurations composed by a nuclear matter shell and a quark core. We obtain stable hybrid stars with a quark core that could occupy a large volume: this can have a significant impact on processes that depend on extensive properties of dense matter. Within the models studied, we found a wide range of parameters for which hybrid stars (as well as neutron stars) are compatible with both observational data and theoretical constraints. Therefore, additional information, such as thermal or magnetic evolution, rotation, etc., of neutron stars is needed to evaluate in a consistent picture the presence or not of an exotic phase. As final remark we should mention that these configurations could be modified if other possibilities for deconfined states such as pion or kaon condensation, hyperons or pairing in quark matter are considered. Their inclusion, however, would introduce more unknown parameters.

References

Aguilera, D. N., Pons, J. A., & Miralles, J. A. 2008, A&A, 441, 1115
Alford, M. G. et al. 2007, ArXiv e-prints, 709, arXiv:0709.4635
Burgio, G. F., & Plumari, S. 2008, Phys.Rev.D, 77, 085022
Cottam, J., Paerels, F.,& Mendez, M. 2002, Nature, 420, 51
Glendenning N. K. 2000, "Compact Stars", I. Appenzeller, Heidelberg, Germany.
Heinz, U. 2001, NuPhA, 685, 414
Lattimer, J. M., & Prakash, M. 2001, ApJ, 550, 426
Lattimer, J. M., & Prakash, M. 2007, Phys. Rep., 442, 109
Maieron, C. et al. 2004, Phys.Rev.D, 70, 043010
Özel, F. 2006, Nature, 441, 1115
Pons, J. A., & Geppert, U. 2007, A&A, 470, 303
Schaffner-Bielich, J. 2005, J. Phys., G31, 651
Sidoli, L., Parmar, A. N., & Oosterbroek, T. 2005, A&A, 429, 291

Stejner, M., Weber, F., & Madsen, J. 2008, arXiv:0801.0358

First La Plata International School, 2008
Compact Object and their Emission, 2009
Ileana Andruchow & Gustavo E. Romero, eds.

A model for kHz QPO in neutron star binaries

Héloise Méheut & Michel Tagger

APC-Univ. Paris Diderot & SAp CEA meheut@apc.univ-paris7.fr

LPCE Orleans

Abstract. We present a model that may explain the twin kHz frequency quasiperiodic oscillation (QPO) observed in neutron star binaries. The model explains the higher frequency QPO with the dynamics of the gas trapped in the neutron star magnetoshere. This approach also gives a clue to understand the difference between the frequencies of the QPO, which is close to but distinct from the rotation frequency of the neutron star.

1. Introduction

Neutron star binaries are at the center of numerous investigations since they are the laboratory of extreme physics such as high magnetic field and strong gravity. These extreme conditions can be explored thanks to the X-rays emissions of the accretion disk of the neutron star. The millisecond variability is one of the key-point of this emission since it is emitted from the inner part of the disk exposed to the higher gravitational field. The kHz quasi-periodic oscillations have been widely studied since their discovery in 1996 by the RXTE satellite. Various theoretical frameworks have been proposed, but none of them was really convincing. The paper presents a new model for the kHz QPO in neutron star binaries, based on the dynamics of the gas in the inner part of the accretion disk.

This paper is organised as follows. First, we present observations of the kHz QPO that have been done, their properties, and we present an overview of the main approaches that have been suggested. Then we consider the stability of the gas that penetrated the magnetosphere and is in corotation with the neutron star, and how the dynamics of this gas may explain the kHz QPO. Finally, the paper is summarized and the perspectives are presented in the last section.

2. Observations and first models

2.1. Neutron star binaries

Neutron star binaries are composed of a neutron star that accretes matter coming from the companion normal star trough an accretion disk. Dynamical timescales can be approximated by supposing that the gas of the accretion disk has a keplerian motion:

$$M \simeq 1.4 M_\odot \quad \text{and} \quad r_0 \simeq 10 \text{ km},$$

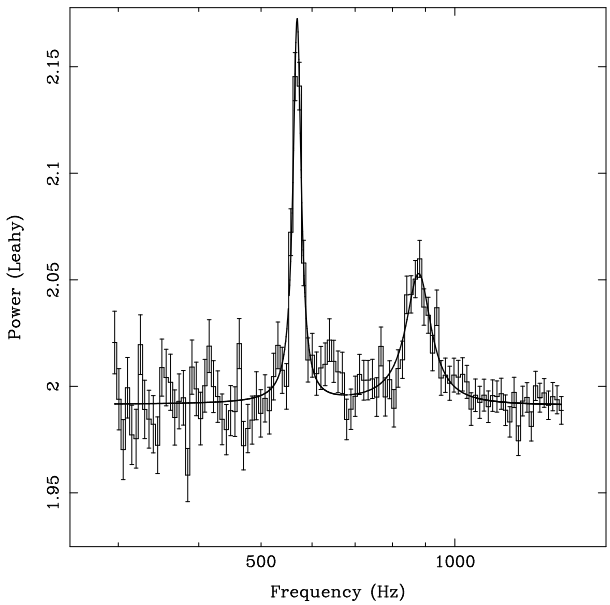

Figure 1. Example of twin QPO observation in 4U 1608-52 (Mendez et al. 1998)

$$\tau_{\rm dyn} = \left(\frac{r_0^3}{GM}\right)^{1/2} \simeq 0.1 \text{ ms},$$

where M is the mass of the neutron star, r_0 is the radius of the neutron star and G the gravitational constant.The keplerian frequency at the inner edge of the disk is then

$$\nu_K = \frac{1}{2\pi\tau_{\rm dyn}} \simeq 1 \text{ kHz}.$$

Because of this order of magnitude, kHz QPO are supposed to be the expression of the physics of the inner disk.

2.2. Twin QPO

In 1996, the X-ray satellite RXTE has detected in the power spectrum of Sco X-1 two simultaneous peaks around 1 kHz, and thereafter twin kHz QPO have been discovered in other low-mass X-ray binaries with a low magnetic field neutron star with diverse X-ray luminosities. An example is shown in Fig.2.2.: the twin QPO can be clearly identified and the lower frequency QPO has a higher quality factor ($Q = \nu/\Delta\nu$ where $\Delta\nu$ is the full width at half maximum) than the higher one. From now on, the two QPO frequencies will be noted $\nu_{\rm l}$ for the lower frequency peak and $\nu_{\rm h}$ for the higher one.

One interesting point of twin QPO is that for the same neutron star binaries, their frequencies may evolve but the difference between the two peaks $\Delta\nu = \nu_{\rm h} - \nu_{\rm l}$, is constant for a wide range of variations of $\nu_{\rm l}$, and $\Delta\nu$ is close but different from the burst oscillation frequency. Those bursts are thermonuclear

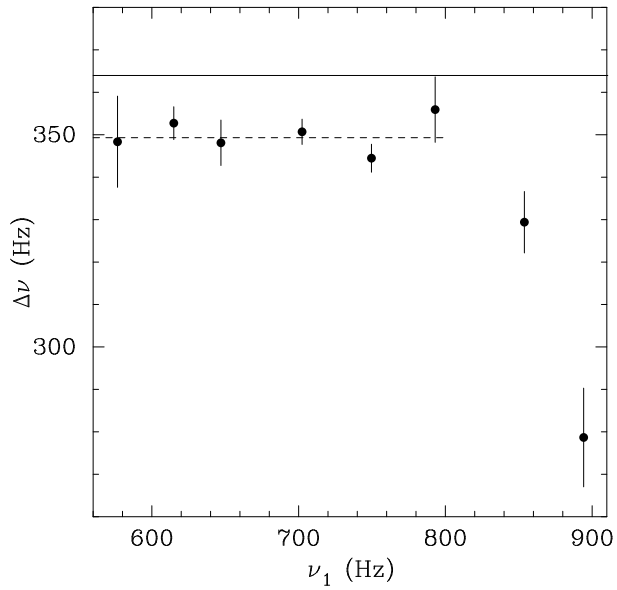

Figure 2. Variations in kHz QPO peak separation as a function of the lower kHz frequency in 4U 1728-34. The upper horizontal line corresponds to the burst oscillation frequency. (Mendez & van der Klis 1999)

runaways in the accreted matter at the surface of the neutron star and the burst frequency is identified to the neutron star rotation frequency Ω_*. In Fig.2.2., we show the QPO frequency in 4U 1728-34 displaying this behaviour; however an important difficulty for models is that $\Delta\nu$ decreases when ν_1 increases.

2.3. Firsts models

After the discovery of the twin kHz QPOs, their intrinsic fundamental nature has been suggested and different models have been proposed. Two main classes of frameworks can be distinguished: those based on a beat frequency and the relativistic precession models. In the beat frequency approach, the higher quasi-periodic oscillation peak is interpreted as the keplerian rotation frequency Ω_K at the inner edge of the keplerian disk, whereas the lower one is due to a beat phenomenon between this keplerian frequency and the neutron star rotation frequency. A more precise presentation of these models can be found in Miller et al. (1998). Therefore, these models provide an explanation for the value of the constant separation between the two peaks but fail to explain the decrease at higher frequencies.

In the relativistic precession model, the frequencies observed are due to the different precession frequencies expected in general relativity. With such an approach some questions remain unanswered, such as the fit of the burst frequency with $\Delta\nu$. For more explanations on these models see Stella & Vietri (1999). So after more than a decade the twin QPO are still not clearly understood.

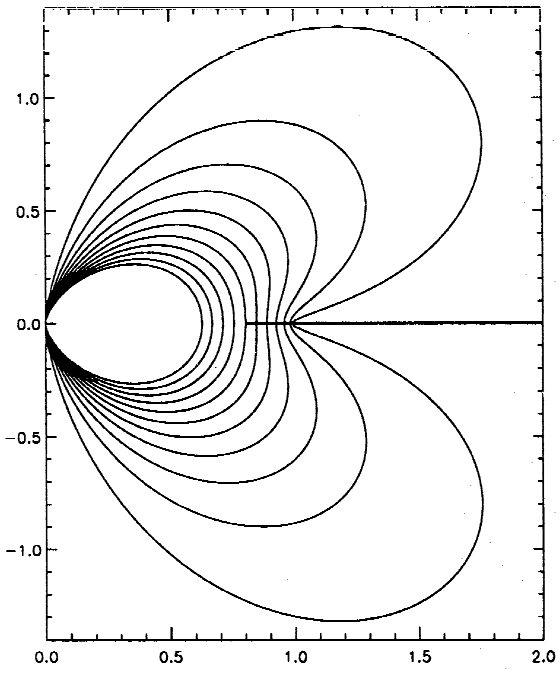

Figure 3. Geometry configuration of the model. The keplerian disk is outside of the magnetosphere of the neutron star and the magnetospheric disk is supported by the magnetic lines, and rotates with the neutron star (Lepeltier & Aly 1998).

3. A new model for the kHz QPO

In the model presented here, we assume that ν_1 is the keplerian frequency at the inner edge of the keplerian disk: this is a fundamental frequency much better adapted to explain the higher quality factor of the lower QPO. We then seek to explain the higher-frequency QPO by the presence of a magnetospheric disk: as far as the neutron star magnetic dipole is pinched by the magnetised keplerian disk, it has been shown (Lepeltier et al. 1996) that with this geometry it is possible to have a layer of gas trapped on the field lines attached to the neutron star, extending the accretion disk inside the magnetosphere (see Fig. 3.). This magnetic field geometry was studied to explain the helmet structures in solar prominences.This magnetospheric disk is in solid rotation with the star, and supported against gravity and magnetospheric accretion by the curvature of the magnetic field.

3.1. Dynamics of the magnetospheric disk

The magnetospheric disk is subject to the interchange instability (Spruit et al. 1990) and a bending instability (Agapitou et al. 1997). Thanks to the first, the gas of the keplerian disk can cross the magnetic lines as long as the instability criterion is verified:

Figure 4. Example of a warped disk: the warped galaxy ESO 510-13

$$\frac{\partial}{\partial r}(\frac{\Sigma}{B_z}) > 0$$

where Σ is the surface density of the magnetospheric disk and B_z is the vertical magnetic field. The magnetospheric disk then has an inner edge where the curvature of the field lines vanishes.

In addition, we consider here a mechanism that was developped initially by Pringle (1996) to explain the warping seen in the outer part of AGN disks: this warping instability is due to the illumination of this outer region by the energetic flux from the inner region of the disk. Here we find that most of the accretion energy is released at the transition between the keplerian and magnetospheric disks, and that it can cause a warp of the nearby magnetospheric disk.

The warp will survive because of the amplification of the bending instability, as it can be seen on the dispersion relation.

$$(\omega - m\Omega_*)^2 = \Omega_K^{d2} + \frac{r(\Omega_K^2 - \Omega^2)}{B_z}\frac{\partial B_z}{\partial r} + \frac{2B_r^2}{\Sigma}|k| + \frac{L}{\Sigma d} + i\frac{L}{\Sigma}|k|, \qquad (1)$$

where ω is the frequency of the instability, Ω_* is the neutron star rotation frequency, m is the wave number , Ω_K^d is the keplerian frequency at the inner edge of the keplerian disk, Σ is the surface density in the magnetospheric disk, B the magnetic field, k the radial wave number, L and d are respectively the luminosity and the radius of the inner edge of the keplerian disk. Even if the two terms of Eq.1 that involve the luminosity are small, they introduce an imaginary part in the frequency of the mode which means that the amplitude of the wave is $\propto e^{\Im(\omega)}e^{i(\Re(\omega)t - m\theta)}$, and with $\Im(\omega) > 0$ the wave is amplified. It is the frequency of this wave that can account for $\nu_{\rm h}$. The fact that $\nu_{\rm h}$ is due to an instability and not an orbital frequency is coherent with the lower quality factor of this QPO.

3.2. Frequencies difference

In some magnetic configurations, the last four terms of the right hand side of Eq.1 may be small enough to be neglected and then this equation can be rewritten as: $\omega - \Omega_K \simeq \Omega_*$ for the first mode. Then, identifying $\nu_{\rm h}$ with ω and $\nu_{\rm l}$ with

Ω_K^d, $\Delta\nu = \nu_{\rm h} - \nu_{\rm l} = \omega - \Omega_K$, which is close to the neutron star's spin frequency. The difference between $\Delta\nu$ and Ω_* is due to the last terms of eq. 1 .

The expansion of the keplerian disk would lead to an increase of the keplerian frequency, a modification of the magnetic configuration, and a modification of the values of the last two terms of the l.h.s. of the Eq. 1 Then at higher QPO frequencies $\Delta\nu$ may diminish, as has been observed.

4. Summary and perspectives

We have presented a new approach for the high frequency QPO in neutron stars binaries. In this model the lower QPO is the fundamental one, it is the keplerian frequency at the inner edge of the accretion disk, and the higher frequency QPO is due to a bending instability in the magnetospheric disk. This model can explain the behaviour of the QPO frequency difference $\Delta\nu$. This work is still in development. We now plan to examine the parameter space, in order to constrain the phyiscal conditions that could fit with the observed values of the frequency difference, and of its variations with the luminosity.

References

Agapitou, V., Papaloizou, J., & Terquem,C. 1997, MNRAS, 631, 645
Lepeltier, T., & Aly, J.J. 1996, A&A, 645,665
Mendez, M., & van der Klis M. 1999. ApJ 517:L51-54
Mendez, M. et al. 1998, ApJL, 505, 23
Miller, M.C, Lamb, F.K., & Psaltis, D. 1998, ApJ, 508, 791
Pringle, J.E. 1996, MNRAS, 281, 357
Spruit, H.C. & Taam, R.E. 1990, A&A, 475,493
Stella, L., Vietri, M. 1999, PhRvL, 82,17

First La Plata International School, 2008
Compact Object and their Emission, 2009
Ileana Andruchow & Gustavo E. Romero, eds.

Rotochemical heating in Neutron Stars with Cooper Pairing

Cristóbal Petrovich.[1,3], Andreas Reisenegger[1] and Rodrigo Fernández[2]

[1] *Pontificia Universidad Católica de Chile,* [2] *University of Toronto.*
[3] *Email: cpetrovi@puc.cl*

Abstract. When a rotating neutron star loses angular momentum the reduction in the centrifugal force makes it contract. This perturbs each fluid element, raising the local pressure and originating deviations from beta equilibrium. This mechanism is named Rotochemical Heating and has previously been studied for neutron stars of non-superfluid matter, finding that the system reaches a new equilibrium configuration. This implies a conversion of rotational energy into thermal energy and an enhanced neutrino emission originated by a departure from the beta equilibrium. As a result, the temperature of the neutron star increases and this mechanism keeps old Millisecond Pulsars at surface temperatures 10^5 K. Another important fact in very condensed matter is the influence of nucleons superfluidity in the thermal evolution of the neutron stars. Superfluidity is due to Cooper Pairing formation of these nucleons (neutrons and protons) and an important effect is the reduction of neutrino emission rate via Direct and Modified URCA processes. Thus, this effect should raise the temperature and thermal luminosity. Our aim is to consider these two mechanisms for describing more accurately the thermal evolution of neutron stars, expecting to fit recent observations.

1. Introduction

Neutron stars thermal evolution is an important tool for the study of dense matter. By comparing cooling models with observations of thermal emission of these objects it is possible to gain insight into the equation of the state, signature of exotic particles, superfluid gaps and magnetic field properties.

At the moment, researchs of the effects of superfluidity has been widely studied in the context of the cooling of neutron stars at the neutrino cooling stage, i.e. an early stage (see Yakovlev et al 2002 for a complete review).

The model we are exploring considers the late thermal evolution of the neutron stars proposing a reheating mechanism with the effects of superfluidity taken into account for a stage where their cooling is mostly determined by the photon luminosity. The main idea is to describe accurately the thermal evolution with a theoretical model wich depends on parameters that are observable: angular frequency and time derivative of the frequency. Thus, measuring the surface temperature of this star it would be possible to infer or constrain the amplitude superfluid gaps and to understand their behavior under certain configuration of the temperature and the density. This problem is unresolved at the

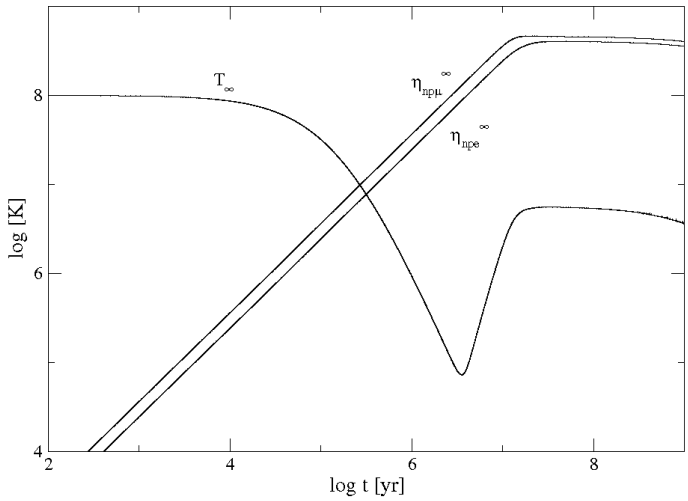

Figure 1. Evolution of the internal temperature and chemical imbalances for a $1.4M_\odot$ star calculated with the A18 + δv + UIX* EOS, with initial conditions $T_\infty = 10^8$ K and null chemical imbalances at $t = 0$, and spin-down parameters $B = 10^8$ G and $P_0 = 1$ ms (figure taken from Fernández & Reissenegger 2005)

moment because the interactions to produce the superfluid state of the matter are very model-dependent at these very high densities.

2. Rotochemical heating mechanism

2.1. Spin down affects local pressure

It is well known that the rotation frequency of pulsars slows down with time. This fact implies directly that the centrifugal force diminishes with time and the neutron star starts to compress. This compression was calculated in the framework of general relativity using lagrangian formalism (Fernández & Reissenegger 2005) and changes strongly with the pressure and the keplerian angular velocity Ω_K. In order of magnitude: $\left(\frac{\partial P}{\partial \Omega^2}\right)_{N,A} \sim -\frac{P}{\Omega_K^2}$ where A and N are the total baryon number and fixed baryon number respectively. With this expression is possible to compute the change in the equilibrium number of particles of species $i = n, p, e$ in terms of the spin-down power $\Omega\dot{\Omega}$, as follows: $\dot{N}_{\rm i}^{\rm eq} = 2\Omega\dot{\Omega} I_{\Omega,{\rm i}}$, where the $I_{\Omega,{\rm i}}$ is a function of $\left(\frac{\partial P}{\partial \Omega^2}\right)_{N,A}$.

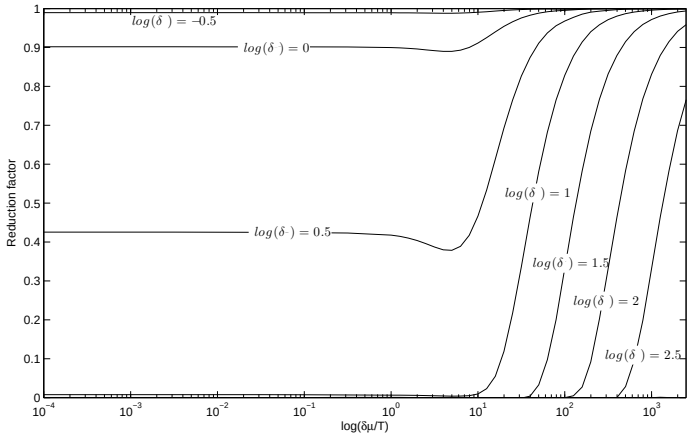

Figure 2. Reduction factor for Direct URCA Process as a function of the departure of beta equilibrium for several values of gap's amplitude Δ in units of k_BT ($\delta = \Delta/k_BT$) (this figure is a recalculation of Villain & Haensel, 2005)

So far with these considerations the local density number has been perturbed and the total baryon number has not been modified, i.e. there exists a departure from beta equilibrium: $\eta_{\rm n,p,e} = \delta\mu_{\rm n} - \delta\mu_{\rm p} - \delta\mu_{\rm e} \neq 0$, where $\delta\mu_{\rm i} = \mu_{\rm i} - \mu_{\rm i}^{\rm eq}$ is the deviation from the equilibrium chemical potential of species i.

2.2. Chemical imbalance: heating the star

The predominant cooling mechanism for neutron star until the age of $\sim 10^5$[yr] is the neutrino emission. Considering $n - p - e - \mu$ matter the most efficient processes are the direct URCA and modified URCA.

When chemical imbalance is present these processes operate as a cooling and heating one, and depending on the relative size of the chemical imbalances $\eta^{\infty}_{\rm n,p,e}$ and temperature kT^{∞} will be net cooling or net heating.

If the spin-down timescale is shorter than the restoring time of the URCA processes, the star will be out of beta equilibrium. As the fraction $\eta^{\infty}_{\rm n,p,e}/(kT^{\infty})$ grows the heating becomes more important, reaching a fixed fraction of 1/2 and 5/8 of the energy for direct URCA and modified URCA respectively. Figure 1 shows this effect, when the ratio $\eta^{\infty}_{\rm n,p,e}$ is larger than (kT^{∞}), the star raises its temperature arriving to a quasi-equilibrium state where the neutron star keeps radiating for a long time with an almost constant temperature.

3. Cooper pairing

Many body fermion systems with an interaction that favors the formation of particle pairs may undergo a phase transition to a superfluid state similar to electrons in superconductors.

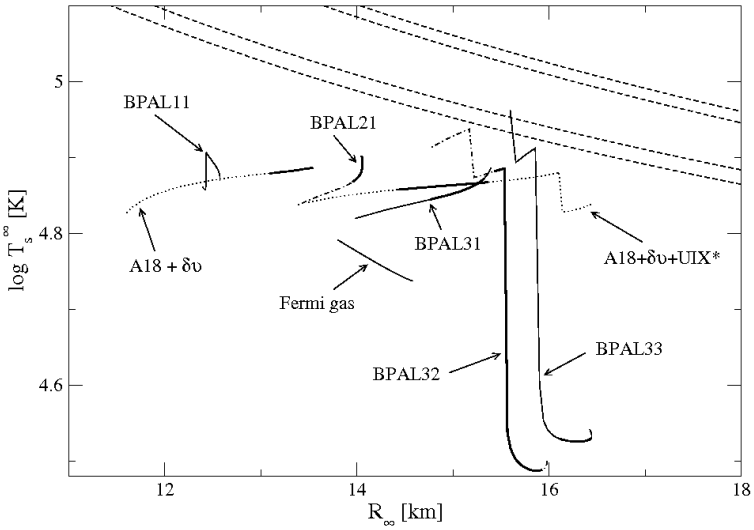

Figure 3. Quasi-equilibrium effective temperatures $T^{\infty}_{\rm S,eq}$ obtained with different EOSs and stellar models, for the spin parameters of PSR J0437-4715. Dashed lines are the 68% and 90% confidence contours of the blackbody fit of (kargaltsev2004) to probable thermal emission from this pulsar. Bold lines indicate, for each EOS, the range corresponding to the mass constraint of (Kargaltsev et al, 2004) for PSR J0437-4715. Abrupt reductions in temperature with (increasing or decreasing) radius correspond to opening of direct URCA reactions (figure taken from Fernández & Reissenegger 2005)

This phenomenon was well-described by the BCS theory (Bardeen, Cooper & Schrieffer, 1957) and these bound states of particle pairs are called Cooper Pairs.

In neutron stars this effect has been widely studied (see Yakovlev et al., 2002) and it is thought that soon after neutron stars birth neutrons and protons in the core become superfluid.

Cooper pairing formation demands:

- Two fermions with oppositte momenta and near the fermi surface, i.e. $|p_{particle} - p_F| << p_F$
- Temperature below the critical temperature T_c of phase transition (e.g. for ^4He, $T_c = 2.19K$).

The main consequence of this phase transition is the appearence of an energy gap Δ at the Fermi surface. This gap represents the latent heat of the phase transition and it must be larger than the temperature scale kT.

3.1. How does superfluidity affect Rotochemical heating?

Superfluidity affects directly the Beta processes, i.e. the cooling and heating motor of the neutron stars in Rotochemical Heating. The energy gap Δ reduces the available phase-space suppressing reactions of superfluid particles at the

Fermi surface in a 2Δ gap, i.e. there is no reactions if the particle's energy is between $\epsilon_F - \Delta$ and $\epsilon_F + \Delta$, where ϵ_F is the Fermi energy. Therefore, Cooper Pairing inhibits reactions in the URCA processes.

For measuring this suppression it is convenient to define a reduction factor R as the ratio between net reaction rate of superfluid matter and non-superfluid matter:

$$R = \frac{\Delta\Gamma_{\rm superfluid}}{\Delta\Gamma_{\rm non-superfluid}}. \quad (1)$$

Figure 2 shows that the roles of the gap Δ and $\delta\mu$,k_BT are opposite: the first inhibits reactions, while the the two second increase the available phase-space and therefore enhance reactions.

4. Results and dicussion: Non-superfluid case

The effective temperature of the quasi-equilibrium state found for rotochemical heating depends almost only on the spin-down power (or period and its derivative):

$$T^{\infty}_{\rm S,eq} \approx (2-3)\times 10^5 \left(\frac{\dot{P}_{-20}}{P^3_{\rm ms}}\right)^{2/7} K$$

This temperature is calculated for several EOS (see figure 3) and is found that the highest one predicted is lower than the balckbody fit of Kargaltsev to the UV emission of PSR J0437-4715 by about 20%.

5. Conclusions

- Rotochemical Heating is an important mechanism for reheating old MSPs: raises considerable the temperature and for a long time.
- Cooper pairing reduces beta reactions, while the roles of $\delta\mu$ and k_BT act counterbalancing the gap's superfluidity.
- Prediction for PSR J0437-4715 is about 20% than the observed value. Taking superfluidity into account this value should increase because Cooper pairing for a given temperature and chemical disequilibrium (η) reduces neutrino reaction rates, forcing the system to reach an equilibrium at higher η that implies a higher temperature.

References

Bardeen, J., Cooper, L. & Schrieffer, J. 1957, PhRv., 108, 1175.
Fernández, R. & Reisenegger, A. 2005, ApJ, 625, 291
Kargaltsev, O. , Pavlov, G. G. & Romani, R. 2004, ApJ, 602, 327
Reisenegger, A. 1995, ApJ, 442, 749
Villain, L. & Haensel, P. 2005 A&A, 444,539
Yakovlev, D. G et al. 2002, Phys. Rep. 354, 1

First La Plata International School, 2008
Compact Object and their Emission, 2009
Ileana Andruchow & Gustavo E. Romero, eds.

Ambiguity of converting phase-averaged flux into luminosity for millisecond pulsars in gamma rays

Anna Zajczyk

Nicolaus Copernicus Astronomical Center, ul. Rabiańska 8, 87-100 Toruń, Poland

zajczyk@ncac.torun.pl

Abstract. We study a magnitude of possible over/underestimation of the actual γ-ray luminosity $L_{\rm actual}$ of a millisecond pulsar when using so-called pseudo luminosity $L_{\rm pseudo}$ which is inferred from a phase-averaged flux. Both, $L_{\rm actual}$ and $L_{\rm pseudo}$ are calculated with the numerical code that models the millisecond pulsar magnetospheric activity in the space charge limited flow approximation with unscreened accelerating electric field. The behaviour of $L_{\rm pseudo}/L_{\rm actual}$ depending on viewing angle is analysed in the energy bands corresponding to the operational energy bands of Fermi GST and H.E.S.S. II.

1. Introduction

Magnetospheric activity of the millisecond pulsars is numerically modelled in order to test the correctness of pulsar theory and also in order to develop the tool that would predict the detectability of these pulsars with high energy observatories.

Our main reason for carrying out the numerical modelling of radiative processes taking place in millisecond pulsar magnetosphere is to check the accuracy of the so-called pseudo luminosity $L_{\rm pseudo}$ which is inferred from the observed phase-averaged flux as an estimation of the pulsar luminosity in γ-rays. In the calculations the unscreened electric field that includes general relativity effects is taken into account. The calculations are made for *a typical* millisecond pulsar with the spin period $P = 2.3$ ms and the magnetic field strength at the pole $B_{\rm pc} = 10^{-3}$ TG. We restrict our analysis to the energy range of γ-rays where the emission is due to the curvature process. An analogous treatment of X-ray characteristics of millisecond pulsars would require taking into account synchrotron radiation due to secondary pairs as well as the thermal component and this is beyond the scope of this work.

The main features of the numerical model are presented in Section 2; Sect. 3 shows the preliminary results of the modelling. The concluding remarks are gathered in Sect. 4.

2. Numerical Model

The radiative processes taking place in pulsar magnetosphere are modelled in 3D. It is assumed that charged particles move along open magnetic field lines

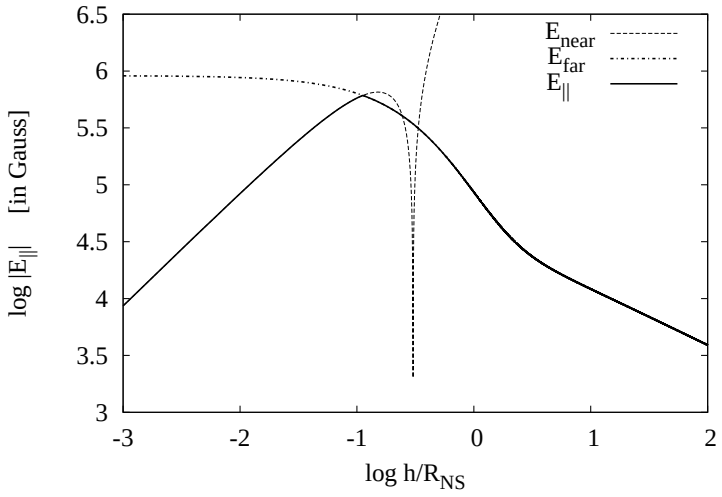

Figure 1. The accelerating electric field for a millisecond pulsar characterised with $P = 2.3$ ms, $B_{\rm pc} = 10^{-3}$ TG, $\alpha = 20^{\circ}$ and $\xi = 0.7$. The total electric field $E_{||}$(solid line) is a combination of a formula describing the electric field near the neutron star $E_{\rm near}$ (dashed line) up to a distance $h \sim 0.7$ of the polar cap radius where a formula depicted with $E_{\rm far}$ (dot-dashed line) becomes applicable.

where their flow is treated within the framework of the space charge limited flow (Fawley et al., 1977). The particles accelerate in the unscreened electric field (Muslimov & Harding, 1997; Harding & Muslimov, 1998) that includes the general relativistic effect of dragging of inertial frames of reference (Muslimov & Tsygan, 1992). It is predicted that for the majority of millisecond pulsars the acceleration voltage drop that develops above polar cap is not limited by the development of a pair formation front (Harding et al., 2002). Thus, particles are accelerated even at high altitudes and it is justified to describe the accelerating electric field as being unscreened.

In the magnetospheres of millisecond pulsars a variety of radiative processes may take place. In this work, however, we restrict the considered processes to curvature radiation and the magnetic absorption of curvature photons without tracing the created secondary particles because it is the curvature emission which (according to polar cap models) dominates completely the γ-ray energy range in millisecond pulsars (Bulik et al., 2000). The escape rate of primary electrons from the neutron star surface is assumed to be the Goldreich-Julian rate in the general relativistic regime (Harding & Muslimov, 1998).

Figure 1 demonstrates the behaviour of the electric field $E_{||}$ - the component parallel to the local magnetic field - above the polar cap (solid line). The accelerating field is a combination of the formula describing the electric field in the vicinity of a pulsar (dashed line; Dyks & Rudak, 2000) and the formula applicable to distances beyond ~ 0.7 of the polar cap radius (dot-dashed line; Muslimov & Harding, 1997). In Fig. 1 the case of a pulsar with $P = 2.3$ ms,

$B_{\rm pc} = 10^{-3}$ TG, $\alpha = 20^\circ$ and $\xi = 0.7$ is shown. Here α is the inclination angle of the magnetic axis with respect to the spin axis and $\xi \equiv \frac{\theta}{\theta(\eta)}$, where θ is a magnetic colatitude and $\theta(\eta)$ is a half-opening angle of the polar magnetic flux tube; $\eta \equiv 1 + \frac{h}{R_{\rm NS}}$, where h is an altitude above the neutron star surface.

3. Results

The parameters of the modelled *typical* millisecond pulsar that were used in calculations are: radius $R_{\rm NS} = 10^6$ cm, mass $M_{\rm NS} = 1.4$ M$_\odot$, moment of inertia $I_{\rm NS} = 10^{45}$ g cm^2, spin period $P = 2.3$ ms, magnetic field strength at the pole $B_{\rm pc} = 10^{-3}$ TG, inclination angle $\alpha = 20^\circ$ and spin down luminosity $L_{\rm sd} \simeq 4\pi^4 c^{-3} B_{\rm pc}^2 \, R_{\rm NS}^6 \, P^{-4} \simeq 5.2 \cdot 10^{35}$ erg s^{-1}.

We present the results for a single millisecond pulsar in the form of photon density maps, which demonstrate the directional dependence of the photon emission in a chosen energy band. Such map is a contour plot where the photon density defined as

$$\dot{N}_{\zeta,\varphi}(E_{\rm min}, E_{\rm max}) = \int_{E_{\rm min}}^{E_{\rm max}} \frac{dN}{dt \, dE \, d\zeta \, d\varphi} dE \qquad (1)$$

is coded in grey scale (N is a number of photons). It is presented in the coordinate system where the pulsar rotation phase $\phi = \varphi/2\pi$ is on the x-axis and the observing angle ζ is on the y-axis. Note that these maps are presented in a different manner than the photon density maps in e.g., Dyks & Rudak (2003), Frąckowiak & Rudak (2005) or Harding (2007).

Two energy bands have been chosen in which the photon density maps of the modelled millisecond pulsar are presented (Fig. 2). The low energy band stretches from 100 MeV to 30 GeV, while the high energy band covers the energies from 30 GeV up to 10 TeV. The energy division corresponds to the energy bands of Fermi GST (the low energy band) and H.E.S.S. II (the high energy band). Photons with energies below 30 GeV (Fig. 2, top panel) are emitted in a range of the viewing angle ζ that is wider in comparison with the range for the high energy band (Fig. 2, bottom panel). The emission cone of the high energy photons is centred at the pulsar magnetic axis. This centring of emission is also traceable in the horizontal cuts made through the photon density maps for chosen observers (Fig. 3). In the energies above 30 GeV the level of the photon density drops dramatically if the observer moves away from the magnetic axis (Fig. 3, right panel). The decrease in the photon density level is also present in the lower energy band (Fig. 3, left panel); however, it is not so rapid. This behaviour is clearly visible if one compares the light curves for $\zeta = 5^\circ$, 20° and 35° in different energies. The overall photon density level is lower for the high energy photons.

To have an idea how accurate the estimations of the average power radiated by the pulsar are, we have calculated a pseudo luminosity $L_{\rm pseudo}$ for both energy ranges. $L_{\rm pseudo}$ emulates the power inferred by an observer viewing the pulsar at an angle ζ. The emitted radiation is confined to a solid angle $\Omega_{\rm pseudo} = 1$ sr. The formula for the pseudo luminosity in the energy range from $E_{\rm min}$ to $E_{\rm max}$

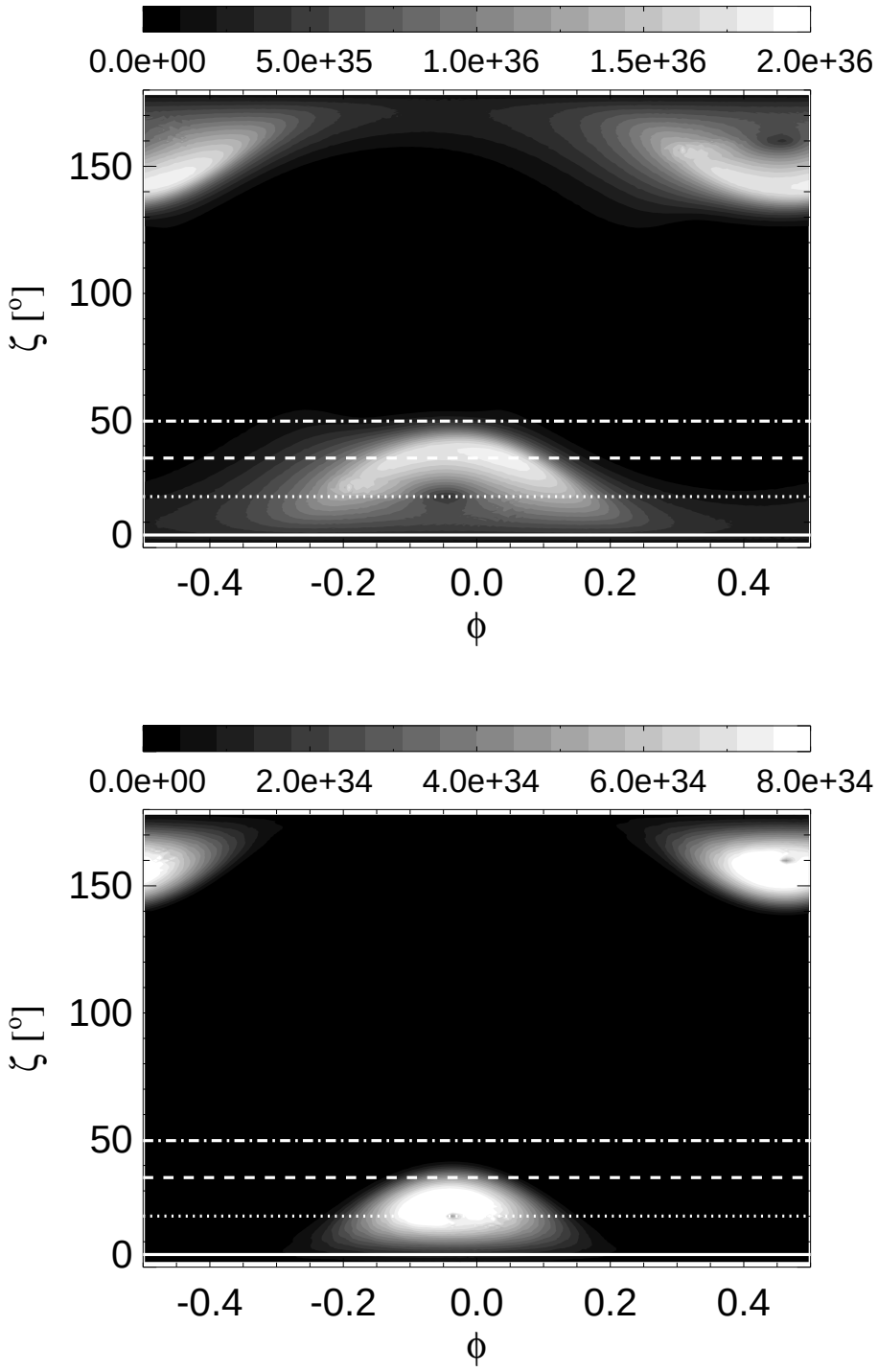

Figure 2. Photon density maps $\dot{N}_{\zeta,\varphi}(E_{\min}, E_{\max})$ in the energy ranges: from 100 MeV to 30 GeV (**top panel**) and from 30 GeV to 10 TeV (**bottom panel**). The pulsar rotation phase $\phi = \varphi/2\pi$ is on the x-axis and the viewing angle ζ in degrees is on the y-axis. White horizontal lines indicate observers for which corresponding light curves have been plotted in Fig. 3. $\zeta = 5°, 20°, 35°, 50°$ are depicted with solid, dotted, dashed and dot-dashed line, respectively. See discussion of the photon density maps in the text.

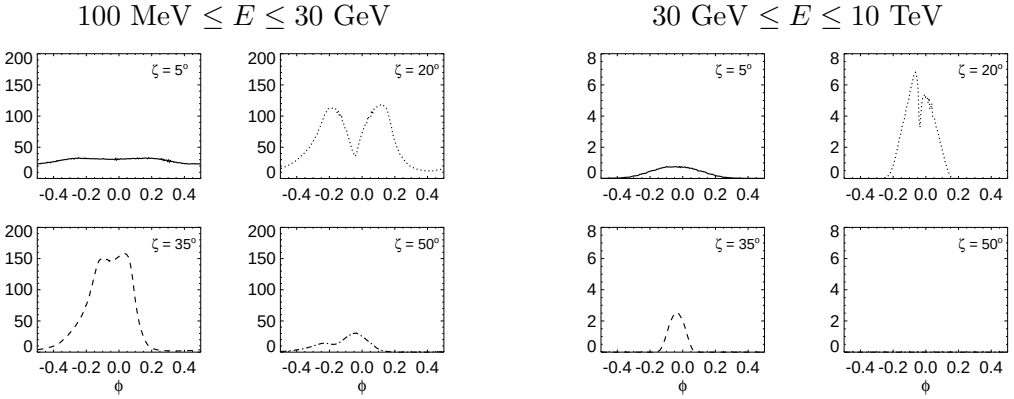

Figure 3. Pulsar light curves for the observers with $\zeta = 5°, 20°, 35°, 50°$ in the energy range from 100 MeV to 30GeV (**left panel**) and from 30 GeV up to 10 TeV (**right panel**). The light curves are due to the horizontal cuts through the photon density maps $\dot{N}_{\zeta,\varphi}(E_{\rm min}, E_{\rm max})$ presented in Fig. 2. The values of the photon density are in arbitrary units.

for a viewing angle ζ is thus given as

$$L_{\rm pseudo}(\zeta; E_{\rm min}, E_{\rm max}) = \frac{\Omega_{\rm pseudo}}{2\pi\ \sin\zeta} \int_{E_{\rm min}}^{E_{\rm max}} \int_0^{2\pi} E\ \frac{dN}{dt\ dE\ d\zeta\ d\varphi}\ d\varphi\ dE \quad . \qquad (2)$$

$L_{\rm pseudo}$ is a theoretical counterpart of $L_{\rm obs}$ inferred from observations in the given energy range $(E_{\rm min}, E_{\rm max})$, which can be described with the following formula:

$$L_{\rm obs}(E_{\rm min}, E_{\rm max}) = \Omega_{\rm arb} \cdot D^2 \cdot \langle F(E_{\rm min}, E_{\rm max})\rangle \quad , \qquad (3)$$

where $\Omega_{\rm arb}$ is a solid angle chosen arbitrarily (1 steradian or sometimes 2π steradians), D is the distance to the object and $\langle F(E_{\rm min}, E_{\rm max})\rangle$ is a phase-averaged energy flux within $(E_{\rm min}, E_{\rm max})$ inferred from observations. This formula is frequently used to asses the pulsar luminosity from the observed phase-averaged flux and the known distance to the object. The modelled pseudo luminosities $L_{\rm pseudo}$ will therefore test the accuracy of the observed luminosities $L_{\rm obs}$ versus the actual luminosity $L_{\rm actual}$.

The theoretical pseudo luminosity spectra are presented in the top panel of Fig. 4. In the same figure the spectrum of the actual power radiated by the pulsar from one pole is shown with solid line.

For each observer we can construct *the bias factor*

$$b \equiv \frac{L_{\rm pseudo}}{L_{\rm actual}} \quad , \qquad (4)$$

where $L_{\rm pseudo}$ is given by Eq. 2 and $L_{\rm actual}$ is defined as

$$L_{\rm actual}(E_{\rm min}, E_{\rm max}) = \int_{E_{\rm min}}^{E_{\rm max}} \int_0^{2\pi} \int_0^{\frac{\pi}{2}} E\ \frac{dN}{dt\ dE\ d\zeta\ d\varphi}\ d\zeta\ d\varphi\ dE \quad . \qquad (5)$$

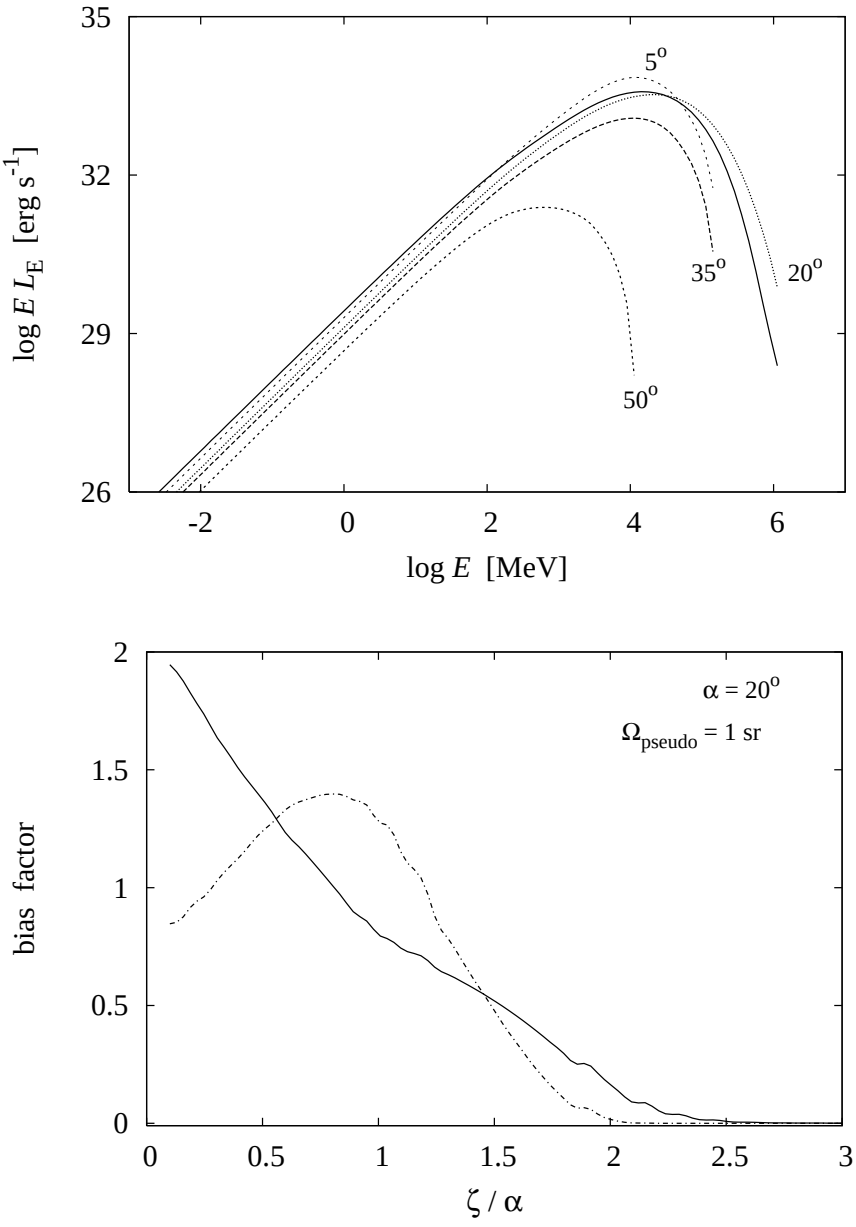

Figure 4. **Top panel:** Pseudo luminosity spectra $L_{\mathrm{E,pseudo};\zeta}$ for the observers with $\zeta = 5°, 20°, 35°, 50°$ are shown. Actual output from each pole $L_{\mathrm{E,actual}}$ is presented here with solid line. Here $L_{\mathrm{E}} = \frac{dL}{dE}$; $L_{\mathrm{E,pseudo};\zeta} = \frac{\Omega_{\mathrm{pseudo}}}{2\pi \sin\zeta} \int_0^{2\pi} E \frac{dN}{dt\, dE\, d\zeta\, d\varphi}\, d\varphi$ and $L_{\mathrm{E,actual}} = \int_0^{2\pi} \int_0^{\frac{\pi}{2}} E \frac{dN}{dt\, dE\, d\zeta\, d\varphi}\, d\zeta\, d\varphi$. **Bottom panel:** The dependence of the bias factor b on the viewing angle ζ scaled with the inclination angle α is presented in the energy range from 100 MeV to 30 GeV and from 30 GeV to 10 TeV with a solid and a dot-dashed line, respectively. See discussion of the bias factor in the text.

Both $L_{\rm pseudo}$ and $L_{\rm actual}$ are calculated within the same energy range ($E_{\rm min}$, $E_{\rm max}$). The dependence of the bias factor on the viewing angle is presented in the bottom panel of Fig. 4. In the low energy range (solid line) the bias factor equals 1 for $\zeta \simeq 0.8\,\alpha$. The observers with $\zeta \lesssim 0.8\,\alpha$ tend to overestimate the pulsar actual luminosity (Eq. 5) using the pseudo luminosity (Eq. 2), while observers with $\zeta \gtrsim 0.8\,\alpha$ underestimate $L_{\rm actual}$. In the high energy range (dot-dashed line) the situation is different due to an opening angle of the radiation smaller than the inclination angle α and $b = 1$ for $\zeta \simeq 0.25\,\alpha$ and $\zeta \simeq 1.2\,\alpha$. Viewing the pulsar with ζ in the range from $0.25\,\alpha$ to $1.2\,\alpha$ results in an overestimation of $L_{\rm actual}$. However, the overestimation is rather insignificant (b is less than 1.5 at the maximum). On the other hand, viewing it with ζ lower than $0.25\,\alpha$ or higher than $1.2\,\alpha$ leads to an underestimation of the pulsar actual luminosity.

Finally, we calculate the gamma-ray efficiency factor[†] :

$$\eta_\gamma = \frac{2L_{\rm actual}}{L_{\rm sd}} \quad . \tag{6}$$

Here, $L_{\rm actual}$ (Eq. 5) is calculated within the energy range stretching from 100 MeV up to 10 TeV. This factor demonstrates what part of the pulsar spin-down luminosity $L_{\rm sd}$ is converted into the gamma radiation. The gamma-ray efficiency factor for the modelled millisecond pulsar is $\eta_\gamma \simeq 0.05$. This result is in good agreement with η_γ estimated by Harding et al. (2002).

4. Conclusions

The preliminary results of the numerical modelling of millisecond pulsars have been presented in this paper. We have calculated the photon density maps in two energy regimes corresponding to the operational energy bands of Fermi GST and H.E.S.S. II. We have also computed the pseudo luminosities for different viewing angles and on their basis the plot presenting the behaviour of the bias factor has been constructed. From the comparison of the bias factor - viewing angle dependence in different energy bands we may infer information on the accuracy of the so-called pseudo luminosity $L_{\rm pseudo}$ as an estimation of the pulsar actual luminosity $L_{\rm actual}$ in γ-rays. It turns out that there are very few favourable ζ for which $L_{\rm pseudo}$ is a good estimate of $L_{\rm actual}$. Most often $L_{\rm actual}$ tends to be under/overestimated. The gamma-ray efficiency factor for the modelled millisecond pulsar has been calculated. Its value $\eta_\gamma \simeq 0.05$ is in agreement with the values in Harding et al. (2002). However, further work concerning modelling, especially the inclusion of radiative processes like synchrotron radiation and inverse Compton scattering important for pulsar X-ray emission, has to be done in order to draw accurate conclusions about millisecond pulsars. Also simulations for other sets of pulsar parameters, especially for different inclination angles α, have to be carried out.

We intend to use the results of modelling as a tool for predicting the detectability of millisecond pulsars with high energy observatories like Fermi GST,

[†] $L_{\rm actual}$ (Eq. 5) is the power output only from one pole. Thus, in order to compare it with $L_{\rm sd}$ we have to multiply it by 2 to include the output from both poles.

H.E.S.S. II and even CTA (Frąckowiak & Rudak, 2005). Furthermore, we plan to develop the population synthesis studies of high energy pulsars that would incorporate the results of the modelling described briefly in this paper.

Acknowledgments. AZ wants to thank Bronek Rudak and Jarek Dyks for many helpful discussions and critical remarks on the paper. AZ is also grateful to the organisers for giving her the opportunity to attend the *LAPIS School* and for financial support. This work was supported by the grant N203 017 31/2872 of the Ministry of Science and Higher Education and the Polish Astroparticle Network 621/E-78/SN-0068/2007.

References

Bulik, T., Rudak, B., & Dyks, J. 2000, MNRAS, 317, 97
Dyks, J., & Rudak, B. 2000, A&A, 362, 1004
Dyks, J., & Rudak, B. 2003, ApJ, 598, 1201
Fawley, W. M., Arons, J., & Scharlemann, E. T. 1977, ApJ, 217, 227
Frąckowiak, M., & Rudak, B. 2005, AdSpR, 35, 1152
Harding, A. K., & Muslimov, A. G. 1998, ApJ, 508, 328
Harding, A. K., Muslimov, A. G., & Zhang, B. 2002, ApJ, 576, 366
Harding, A. K. 2007, ArXiv:0710.3517
Muslimov, A. G., & Harding, A. K. 1997, ApJ, 485, 735
Muslimov, A. G., & Tsygan, A. I. 1992, MNRAS, 255, 61

First La Plata International School, 2008
Compact Object and their Emission, 2009
Ileana Andruchow & Gustavo E. Romero, eds.

Unveiling new quiescent BHs with IPHAS

Jesús M. Corral-Santana, Jorge Casares & Ignacio G. Martínez-Pais

Instituto de Astrofísica de Canarias,
Vía Láctea, s/n, 38205 La Laguna,
S/C de Tenerife, SPAIN

Abstract. X-ray transients provide the best evidence for the existence of stellar-mass BHs, with almost 20 confirmed cases based on dynamical studies. However, these are only the tip of iceberg of an estimated population of a few thousand BH binaries, which slowly reveal themselves through secular X-ray outbursts. Therefore, new strategies aimed at unveiling this dormant population are clearly needed. We propose to use the IPHAS catalogue, together with several diagnostic diagrams, as a shortcut to unveil the brightest members of the galactic population of BH binaries.

1. Introduction

X-ray binaries are binary systems composed by a compact object, either black hole (BH) or neutron star (NS), and a companion star which transfers material to the compact object through an accretion disk.

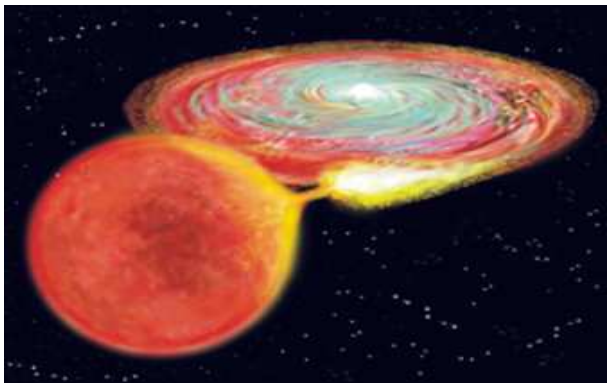

Figure 1. Image of a XRB. The donor star fills its Roche Lobe and transfers material to the compact object through the Lagrangian point. The material forms an accretion disk and finally is accreted by the compact object.

According to the mass of the companion star, they classically were classified in Low-Mass (LMXBs) and High-Mass X-ray Binaries (HMXBs), but in new reviews the Intermediate-Mass (IMXBs) have been considered (Casares, 2006).

We are just interested in LMXBs and inside this class, the Soft X-Ray Transients (SXTs). These systems have a low mass transfer rate and consequently

they stay in quiescence most of the time. They provide the best evidence for stellar-mass BHs based on dynamical studies which have demonstrated that ∼75% of SXTs contain accreting BHs.

There are only 17 galactic BHs confirmed by dynamical studies and all of them were discovered when they went into outburst. However, these 17 are just the tip of an iceberg of an estimated population of a few thousands XRBs in the Galaxy (Casares, 2006).

In the Figure 2 we can see the distribution of XRBs in the Galaxy. Since most of them are located in the Galactic Plane we propose to use the IPHAS survey to unveil new quiescent BHs.

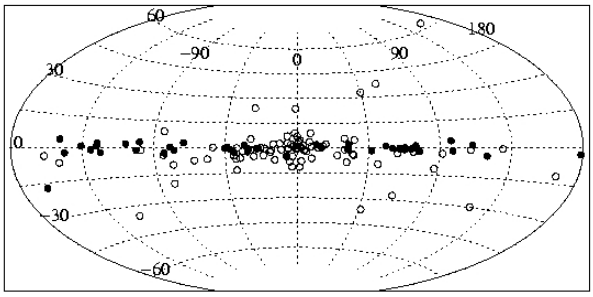

Figure 2. Distribution of XRBs in the galaxy. HMXBs are in solid dots, while LMXBs are represented in open circles. HMXBs are located around the Galactic Plane, LMXBs are mainly in the bulk, however most of them are between $-10^\circ < b < 10^\circ$, the rest of them are associated to globular clusters or have a NS as accreting object.

2. What is IPHAS...?

It is the acronym of *The Isaac Newton Telescope Photometric Hα survey*. It is an Hα map of the Galactic Plane between $-5^\circ < b < 5^\circ$ galactic latitude that is visible from La Palma.

It is made with the Wide Field Camera (WFC) mounted at the 2.5m Isaac Newton Telescope (INT) on the Observatorio del Roque de los Muchachos, in the Canary Island of La Palma (Spain), using 2 broad-band Sloan r' and i' filters and a narrow-band Hα. The magnitude range is between 13 and 20 (10σ) magnitudes in the r'-band (Drew et al., 2005).

The first catalogue has 200 million objects and, at this moment, more than 90% of 1800 deg^2 have been observed and it is expected to conclude during this year (González-Solares et al., 2008).

There are other surveys in progress to extend IPHAS, for instance:

- **UVEX**: *The Northern Galactic Plane UV-excess Survey* will complete IPHAS in the blue range using u',g' and r'.

- **VPHAS+**: *VST/OMEGACAM Photometric Hα and broad-band Survey of the Southern Galactic Plane*, will complete IPHAS and UVEX but in the Southern Hemisphere.

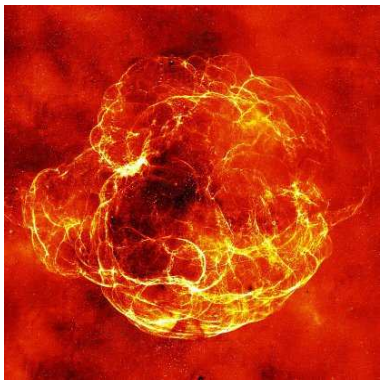

Figure 3. Beautiful image of SNR S147 composed by hundreds of IPHAS fields in Hα.

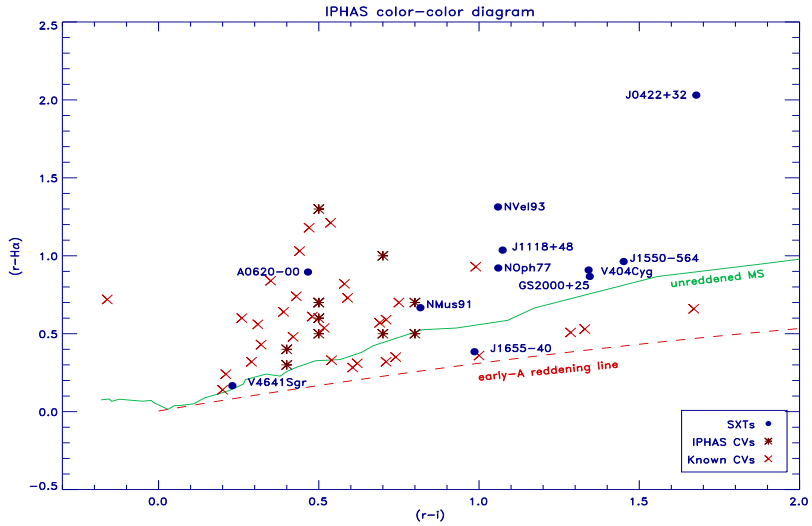

Figure 4. IPHAS color-color diagram with CVs and SXTs. Those CVs discovered using IPHAS are represented in red stars, while other CVs previously known in the Galactic Plane are in red crosses. Most of the SXTs (blue dots) are bluer than (r'-i')=0.9 while CVs with Hα excess are bluer than 0.9.

3. Preliminary results

As it has been said, all the 17 confirmed galactic BHs along the last 37 years, were discovered when the binary system went into outburst and being detected in

X-rays and this is the reason why the number is so small. In order to significantly increase the known sample, we are trying to establish several diagnostic diagrams to unveil new quiescent BHs present in the catalogue using their strong Hα emission.

As a first step, we tried to distinguish between SXTs and cataclysmic variables (CVs). We have collected 11 confirmed BHs and through convolving their spectra with IPHAS filters, we obtain their r', i' and Hα magnitudes. Then, we plotted their positions in a color-color diagram (r'-Hα)-(r'-i'), together with known CVs, finding that there is a separation between these populations: SXTs tend to be redder than (r'-i')=0.9 while CVs are bluer than 0.9.(Figure 4). In this diagram we have also plotted the 11 CVs already discovered using IPHAS (Witham et al., 2007) and they agree with this criteria.

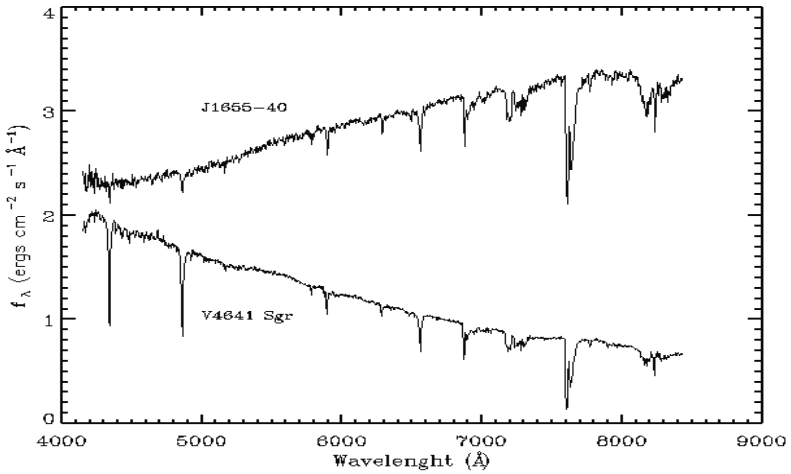

Figure 5. V4641 Sgr and J655-40 are IMXBs, so their spectra are completelly dominated by their donor stars (B9III and F6IV respectively). This is the reason why they are under the unreddened main-sequence track.

However two of our SXTs are below the unreddened Main-Sequence track. This synthetic line represents the Hα no-emission line for each spectral type at E(B-V)=0, so any object above this line has an Hα excess. V4641 Sgr and J1655-40 are below this track because they are IMXBs (we are just interested in LMXBs) and their optical spectra are totally dominated by their donor stars as seen in Figure 5.

We also expect a fraction of SXTs to lie in the CVs region and these will be difficult to identify. We see here some examples, the BH system A0620-00 which is only at 1kpc and NMus 91.

There are other kind of objects than could contaminate our sample, such as (see Figure 6):

- **Miras**: A type of variable stars, but they are all under the Main Sequence track
- **Symbiotic stars**: They usually have larger EWs of tipically 400 Å while SXTs used to have EW$\sim$10-40 Å(Corradi et al., 2008).

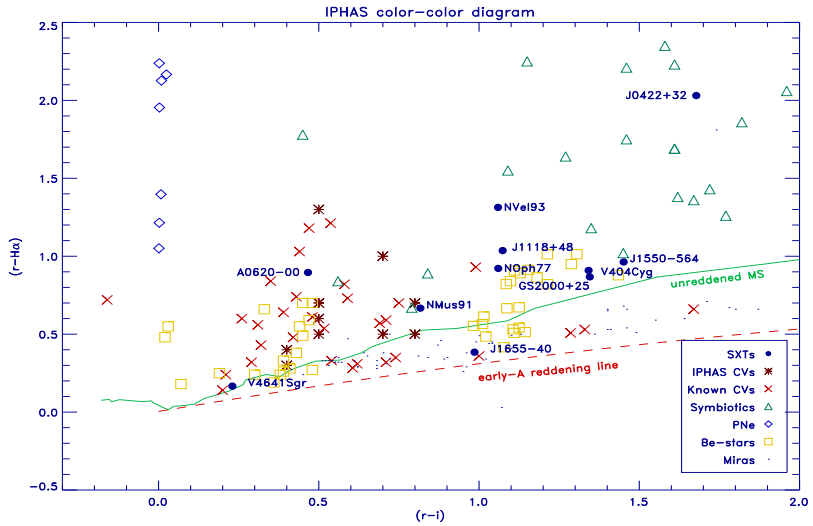

Figure 6. (r'-i')-(r'-Hα) diagram. The green line represents de unreddened Main-Sequence track and the dashed red line is the early-A reddening line. In this diagram are represented almost any kind of object we can find in the Galactic Plane than can be confused with SXTs. CVs (see Figure 4), Planetary Nebulae in blue diamonds, Symbiotics in green triangles, Miras in dots and Be-star in yellow squares. These last ones are probably the objects more similar to ours due to their colors.

- **Planetary Nebulae**: but they are non-stellar objects and are bluer than SXTs. Most of them are located in the top left of the diagram or even outside its limits (Viironen et al., 2008).
- **Be-stars**: These are probably our potential overlaps. We need to go to bluer colors (provided by UVEX survey) and/or IR to distinguish these from SXTs.
- **CVs**: It is possible to have some CVs in the SXTs region (Witham et al., 2006 ; Witham et al., 2007), but we hope to be able to distinguish them by means of the Balmer decrements (the $H\alpha/H\beta$ ratio) that are more extreme in SXTs than CVs (Horne et al., 1986).

J0422+32 and J1118+480 were reddened to E(B-V)=1.5 and 0.8, respectively, because they are out of the Galactic Plane. These reddening were taken according to their distances.

4. Future work

Our aim is to confirm these diagnostics combining IPHAS diagram with IR information using 2MASS or UKIDSS GPS as well as X-ray using ROSAT, blue range using UVEX and Radio properties. Once we have a cleaned sample, we will do follow-up spectroscopy to confirm the nature of the objects and finally calculate the orbital period and mass function of those SXTs.

References

Casares, J. 2006, astro-ph:061231
Corradi, R. L. M., et al. 2008, A&A 480, 409
Drew, J. E., et al. 2005, MNRAS 362, 753
González-Solares, E. A., et al. 2008, MNRAS 288, 89
Horne, K. and Marsh, T. R. 1986, MNRAS 218, 761
Viironen, K. et al. 2008, A&A, in preparation
Witham, A. R., et al. 2006, MNRAS 369, 581
Witham, A. R., et al. 2007, MNRAS 382, 1158

First La Plata International School, 2008
Compact Object and their Emission, 2009
Ileana Andruchow & Gustavo E. Romero, eds.

Accretion discs in compact interacting binaries: optical spectroscopy of X1822-371

Auni Somero

Observatory, P.O. Box 14, FIN-00014 University of Helsinki, Finland. Nordic Optical Telescope, Apartado 474, 38700 Santa Cruz de La Palma, Spain. auni@not.iac.es

Abstract. X1822-371 is a low-mass X-ray binary where a neutron star accretes mass from a low-mass normal star. In addition to the accretion disc around the neutron star, the system contains an accretion disc corona. This has made it maybe the strongest case for existence of thick, or warped, accretion discs as opposed to the standard, geometrically thin, Shakura-Sunyaev accretion disc model. We present preliminary results of phase-resolved high time and medium spectral resolution optical observations.

1. Introduction

Low-mass X-ray binaries (LMXBs) are interacting binary systems consisting of an accreting compact object, which is a neutron star (NS) or a black hole (BH), and a mass donating late type normal star. The mass transfer between the components occurs via the Roche Lobe overflow creating an accretion disc around the primary. The release of the gravitational potential energy of the in-falling matter is converted to X-ray radiation which in turn produces optical emission via X-ray heating (Lewin, van Paradijs & van den Heuvel, 1997).

X1822-371 (V691 CrA) is an LMXB with an accretion disc corona (ADC), an extended X-ray emitting region above and below the accretion disc. The primary of X1822-371 is a neutron star with the X-ray pulse period of 0.59 s (Jonker & van der Klis, 2001). The 5.57 h orbital period of the system can be seen both in optical (Mason et al. 1980) and in X-rays (White et al. 1981). The light curve in both wavelength ranges contains a partial eclipse indicating that the secondary is not able to obscure the whole emitting region (the ADC in X-rays and the accretion disc in the optical).

The modulation of the light curve outside the eclipse is explained to be due to the varying height of a thick accretion disc rim. The inclination of the system ($i = 81 - 84°$, Heinz & Nowak 2001) has been determined by light curve modelling. Due to the high inclination and a presumably high vertical extent of the accretion disc rim (Hellier & Mason, 1989), we are not able to see the inner accretion disc and the actual X-ray source. Thus we see only X-rays scattered from the accretion disc corona, which also explains the low ratio of $L_X/L_{\rm opt}$ ~ 20 of the system compared to the usual value of LMXBs ($\sim 100 - 1000$).

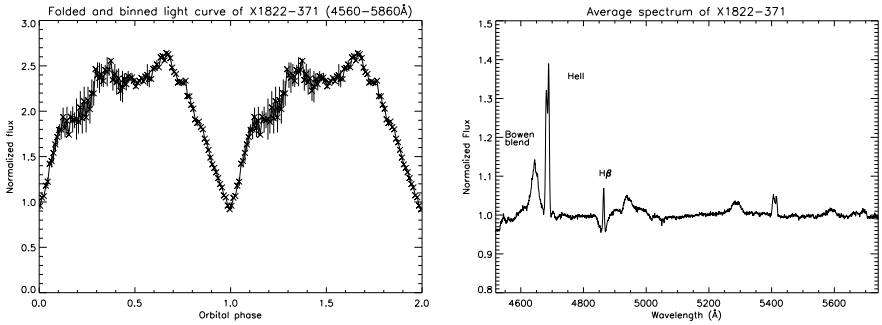

Figure 1. *Letf:* The light curve of the integrated flux of the individual VLT spectra normalized at phase 0. The data are shown twice for clarity. *Right:* The average of the 224 spectra. The emission lines of the Bowen blend, HeII and Hβ are marked.

2. Observations and data analysis

X1822-371 was observed with FORS2 (Appenzeller et al., 1998) at the Very Large Telescope of the European Southern Observatory in Chile on June 15 2006. In total 224 spectra were obtained with the grism 1400V (4560-5860 Å) and a 0.7" slit yielding a resolution of 80 km/s (FWHM). The observations cover approximately 1.6 times the orbital period of the target and the time resolution is about 2 minutes. The wavelength range of the grism contains the strongest optical emission lines of the target: HeII (4686 Å), Hβ (4861Å) and the Bowen blend at 4640 Å. A comparison star was put into the slit in order to monitor slit losses and to obtain relative flux calibration.

The spectra were reduced using standard IRAF[1]/PyRAF packages. Further data preparation and Doppler mapping were done with the MOLLY and DOPPLER software packages provided by Tom Marsh.

3. Results

In Fig. 1 are presented the folded and binned light curve integrated from the individual spectra and the normalized average spectrum. The partial eclipse and the out of eclipse modulation is clearly seen in the light curve. In the average spectrum the lines of main interest (the Bowen blend, HeII and Hβ) are clearly visible.

Fig. 2 shows the trailed spectrogram of the 224 spectra over the wavelength range of 4600-4900 Å. There are clear variations in the shape and strength of all the lines, the Bowen blend being fainter than the other lines. The behaviour of

[1]IRAF is distributed by the National Optical Astronomy Observatories, which are operated by the Association of Universities for Research in Astronomy, Inc., under cooperative agreement with the National Science Foundation.

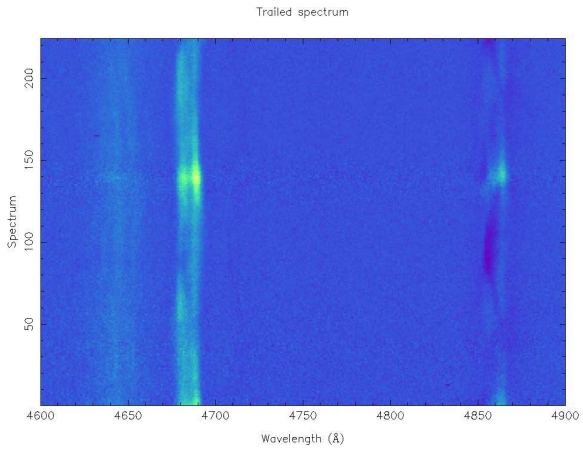

Figure 2. Trailed spectrogram of the wavelength range of 4600-4900 Å. Brighter colour refers to higher intensity.

the Hβ line is more complex, with P Cygni like profiles appearing at some phases (the darker colour in the spectrogram is absorption), this possibly indicates the existence of a disc wind in the system.

The phase-resolved profiles of the emission lines of HeII and the Bowen blend were used to map the location of the emission in the system by using Doppler tomography (Marsh & Horne, 1988). This technique uses the emission line profiles of different orbital phases to create a map of the emission region in the velocity space of the binary system. The Hβ line could not be used for Doppler tomography because it contains a superimposed absorption component and it is impossible to distinguish the underlying emission component.

The resulting Doppler maps are shown in Fig. 3. The HeII line emanates from the accretion disc, and as the Doppler map shows it is clearly not smoothly distributed over the accretion disc which is an indication of asymmetric structure, but the emission is stronger in the negative $V_{\rm x}$. That is the side of the accretion disc where the accretion stream from the companion hits the disc. The Doppler map for the Bowen blend shows a bright spot at positive $V_{\rm y}$ of few hundred km/s. This refers to the companion star and is in accordance with the fact that usually the Bowen blend originates in the X-ray heated face of the companion. These results are consistent with previous studies of the system (Casares et al., 2003).

4. Summary and perspectives

In this paper, preliminary results of phase-resolved high time and medium spectral resolution optical observations of X1822-371 are presented. We used the Doppler tomography technique to create maps of the emission regions of the HeII (4686 Å) and the Bowen blend lines. The maps show that the Bowen blend originates from the secondary star as expected and the HeII emission comes from the accretion disc and is asymmetrically distributed.

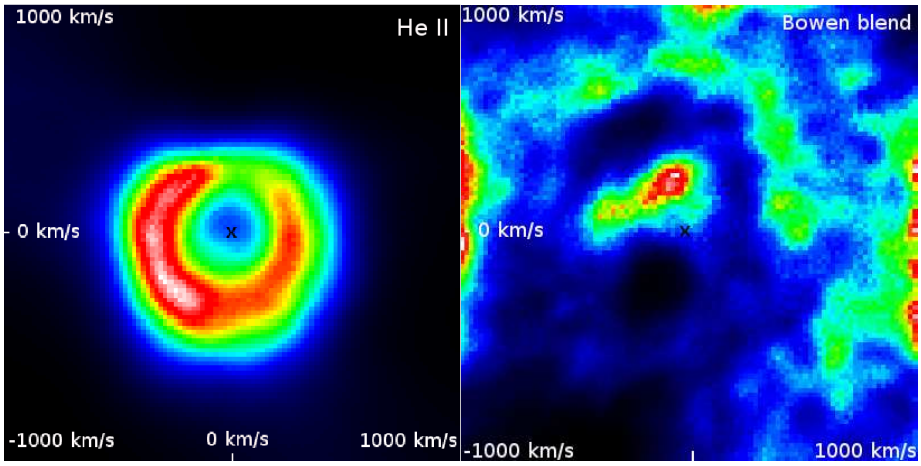

Figure 3. *Letf:* The Doppler map of the HeII line. *Right:* The Doppler map of the Bowen blend.

The main limitation of the present results is the fact that the Doppler tomography analysis assumes the accretion disc to be flat, so in case of a thick and structured disc, the resulting maps are affected. The work on analysing the data in more detail will continue and further analysis will be carried out taking into account the shading of the thick accretion disc rim.

Acknowledgments. We thank Tom Marsh for the use of MOLLY and DOPPLER softwares. A.S. would like to thank the organizers of the La Plata school and the Vilho, Yrjö ja Kalle Väisälä Foundation for the financial support.

References

Appenzeller, I., et al. 1998, The Messenger, 94, 1
Casares, J., et al. 2003, ApJ, 590, 1041
Heinz, S., & Nowak, M. A. 2001, MNRAS, 320, 249
Hellier, C., & Mason, K. O. 1989, MNRAS, 239, 715
Jonker, P. G., & van der Klis, M. 2001, ApJL, 553, 43
Lewin, W. G., van Paradijs, J., & van den Heuvel, E. P. J. (eds.) 1997, *X-ray binaries*, Cambridge University Press
Marsh, T. R., & Horne, K. 1988, MNRAS, 235, 269
Mason, K. O., et al. 1980, ApJL, 242, 109
White, N. E., et al. 1981, ApJ, 247, 994

First La Plata International School, 2008
Compact Object and their Emission, 2009
Ileana Andruchow & Gustavo E. Romero, eds.

High-energy emission from low-mass microquasars

Gabriela S. Vila[1] & Gustavo E. Romero[1,2]

[1] *Instituto Argentino de Radioastronomía (IAR-CCT La Plata-CONICET), C.C.5, 1894 Villa Elisa, Buenos Aires, Argentina. gvila@iar-conicet.gov.ar*

[2] *Facultad de Ciencias Astronómicas y Geofísicas, UNLP, Paseo del Bosque s/n, 1900 La Plata, Buenos Aires, Argentina.*

Abstract. Microquasars are binary systems with a compact object accreting from a donor star, characterised by the presence of relativistic jets. The electromagnetic spectra of microquasars can range from radio to gamma-rays. In this work we explore the possibility of obtaining high-energy emission from microquasars where the donor star is a low-mass, old and dim star without strong winds. We propose that the interaction of relativistic particles with radiation and magnetic fields in the jet can be an efficient channel of gamma-ray production in such systems. We focus particularly in proton-dominated jets. We develop a simple model to characterise the jet and the distribution of relativistic particles in steady state. We then calculate the emission spectrum due to different processes: synchrotron radiation, inverse Compton scattering and proton-photon interaction. The contribution of secondary leptons is also estimated. Our results indicate that, under some conditions, low-mass microquasars might be gamma-ray sources detectable by high-energy instruments like GLAST.

1. Introduction

There exists a group of variable gamma-ray sources in the galactic halo whose nature still remains unidentified. They are located at high galactic latitudes, typically from 2 to 8 kpc, and they present variability on all time scales. The luminosity of these sources in gamma-rays is in the range $\sim 10^{33-36}$ erg/s, 10-100 times higher than their luminosity in X-rays. They display soft spectra, with spectral indices ~ 2.5 (if S_γ is the measured photon flux, then $S_\gamma \propto E_\gamma^{-2.5}$). Among the possible counterparts of some of these halo sources are low-mass microquasars (LMMQs). Microquasars are binary systems composed by a black hole accreting from a companion star. They present jets of relativistic particles. In the case of a LMMQ, the donor star is a low-mass, old and dim star, without strong winds. The microquasar scenario can account for several of the general characteristics of the halo sources. The rapid variablity observed in these sources implies the presence of a compact object, and it is known that microquasars might be the site of efficient particle acceleration and high-energy emission, as demonstrated by the detection of three of them at TeV energies (Aharonian et al. 2005; Albert et al. 2006; Albert et al. 2007). LMMQs in particular, have

large proper motions and they can be found outside the galactic plane (Mirabel et al. 2001; Ribó et al. 2002). An example is XTE J1118+480, the firmest black hole candidate in the galactic halo.

Several models have been proposed for the production of gamma-rays in LMMQs. Grenier et al. (2005) developed a model based on inverse Compton scattering (IC) of external photon fields by relativistic leptons in the jets. The photons are provided by the star, and the accretion disk and the corona of hot plasma that surround the black hole. However, in a LMMQ these fields are too weak for this mechanism to explain the observed luminosities. As an alternative, synchrotron self-Compton (SSC) interactions were considered by Aharonian & Atoyan (1998), Atoyan & Aharonian (1999) and Bosch-Ramon et al. (2006). In this case, the target photons for IC scattering are produced by the same electrons in the jet through synchrotron radiation. Models based on hadronic interactions were introduced as well. Romero et al. (2003) studied the production of gamma-rays in LMMQs through proton-proton inelastic collisions between relativistic protons in the jet and the matter field of the wind of the star. Photohadronic interactions were introduced in the context of microquasars by Levinson & Waxman (2001).

In this work we propose that high-energy electromagnetic emission in low-mass microquasars can be produced through the interaction of relativistic leptons and hadrons with the radiation field and the magnetic field in the jet, and not with external fields. We develop a simple model of jet, obtain the distribution of relativistic particles, and calculate the emission spectra taking into account several radiation processes. Finally, we asses the possible detection of these sources by future gamma-ray instruments.

2. Jet model

We consider a conical jet, launched perpendicular to the orbital plane. It is injected at a distance $z_0 \approx 10^8$ cm from the compact object, where z is the jet axis. The jet radius grows as $r(z) = r_0(z/z_0)$, with $r_0 = 0.1z_0$. The outflow is only mildly relativistic, with a bulk Lorentz factor of $\Gamma_{\rm jet} = 1.5$. We assume that a fraction $q_{\rm jet} = 0.1$ of the accretion luminosity $L_{\rm accr} = 2 \times 10^{39}$ erg s^{-1} powers the jet, $L_{\rm jet} = q_{\rm jet} L_{\rm accr}$. This energy is divided between the relativistic hadrons and leptons that populate the jet, $L_{\rm jet} = L_p + L_e$. We relate the energy budget of both species as $L_p = aL_e$. Since we want to study proton-dominated jets, we only consider the case $a \geq 1$.

Although not completely understood, the mechanism of ejection of the jets is thought to be magnetohydrodynamic. If this is the case, there must be at least as much energy stored in the magnetic field as kinetic energy in the plasma that is being ejected. Therefore, the magnetic field at the base of the jet can be estimated assuming equipartition of energy between the magnetic energy density and the kinetic energy density of the jet at z_0, $U_B(z_0) = U_{\rm kin}(z_0)$. The value of $B_0 = B(z_0)$ can be obtained from the relation

$$\frac{B_0^2}{8\pi} = \frac{L_{\rm jet}}{\pi r_0^2 v_{\rm jet}}, \qquad (1)$$

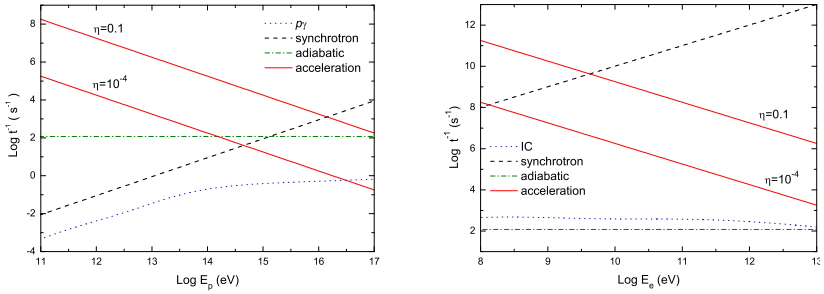

Figure 1. Acceleration and cooling rates at the base of the jet for protons (left panel) and electrons (right panel), calculated for representative values of the model parameters ($E^{\rm min} = 100\,mc^2$, $a = 1$ and $\alpha = 2.2$).

where $v_{\rm jet}$ is the jet's bulk velocity. This yields a value of $B_0 \approx 10^7$ G. For $z > z_0$, the magnetic field decays as the jet expands,

$$B(z) = B_0 \frac{z_0}{z}. \tag{2}$$

The acceleration of particles takes place in a compact region that extends from z_0 to $z_{\rm max} = 5z_0$. Relativistic particles are injected at a rate

$$Q = Q_0 \frac{E^{-\alpha}}{z} \qquad [\mathrm{Q}] = \mathrm{erg}^{-1}\mathrm{cm}^{-3}\mathrm{s}^{-1}. \tag{3}$$

Diffusive shock acceleration naturally leads to this type of power-law injection function. We consider two different values for the spectral index, $\alpha = 1.5$ and $\alpha = 2.2$, hard and soft injection spectrum, respectively. The z-dependence in Eq. 3 was added to take into account that the injection is reduced as the distance from the compact object increases.

The maximum energy of a relativistic particle in the jet can be estimated equating the acceleration rate and the rate of cooling, $t_{\rm acc}^{-1} = t_{\rm cool}^{-1}$. The acceleration rate for a particle of charge e in a magnetic field B is given by

$$t_{\rm acc}^{-1} = \eta ceBE^{-1}. \tag{4}$$

The parameter η characterises the efficiency of the acceleration. We studied two cases, $\eta = 0.1$ and $\eta = 10^{-4}$, that describe a very efficient and a poor acceleration, respectively.

Particles lose energy through adiabatic and radiative losses, $t_{\rm cool}^{-1} = t_{\rm ad}^{-1} + t_{\rm rad}^{-1}$. As can be seen from Fig. 1, the main radiative process of energy loss is synchrotron radiation, with a cooling rate

$$t_{\rm synchr}^{-1} = \frac{4}{3}\left(\frac{m_e}{m}\right)^3 \frac{c\sigma_T U_B}{m_e c^2}\frac{E}{mc^2}. \tag{5}$$

This is the only relevant cooling channel for electrons. For protons, adiabatic losses must also be taken into account,

$$t_{\rm ad}^{-1} = \frac{2}{3}\frac{v_{\rm jet}}{z}. \tag{6}$$

We obtain a maximum proton energy of $E_p^{\rm max} \sim 10^{17}\eta^{1/2}$ eV, whereas for electrons $E_e^{\rm max} \sim 3 \times 10^{10}\eta^{1/2}$ eV.

The distibution in energy of the relativistic particles, $N(E,z)$ (erg^{-1} cm^{-3}), was calculated as in Khangulyan et al. (2007), solving the transport equation in steady state in the "one-zone" approximation,

$$\frac{\partial}{\partial E}\left[\left.\frac{dE}{dt}\right|_{\rm cool} N\left(E,z\right)\right] + \frac{N\left(E,z\right)}{t_{\rm esc}} = Q\left(E,z\right). \tag{7}$$

Here, $dE/dt|_{\rm cool} = Et_{\rm cool}^{-1}$, and $t_{\rm esc} = z_{\rm max}/v_{\rm jet}$ is the particle escape time from the acceleration region. This equation describes an homogeneus jet, and it is valid as long as the acceleration region is compact. The resulting distributions have a power-law dependence in the particle energy. For protons, N_p mimics the injection function, $N_p \propto E_p^{-\alpha}$; for electrons strong synchrotron losses produce a break in the spectrum, and $N_e \propto E_e^{-(\alpha+1)}$.

3. Radiative processes

We consider three contributions to the emission spectrum: synchrotron radiation of primary protons and primary and secondary leptons, leptonic inverse Compton scattering and photohadronic interactions.

The synchrotron spectra is calculated using standard formulae, as can be found for example in Blumenthal & Gould (1970). The power radiated by a single particle of energy E, mass m and charge e is given by

$$P_{\rm synchr}\left(E_\gamma, E, z, \alpha\right) = \frac{\sqrt{3}e^3 B(z)}{4\pi mc^2 h}\frac{E_\gamma}{E_{\rm c}}\int_{E_\gamma/E_{\rm c}}^{\infty} {\rm d}\xi\, K_{5/3}(\zeta). \tag{8}$$

Here E_γ is the energy of the emitted photon, α is the pitch angle (angle between the particle momentum and the magnetic field), and $K_{5/3}(\zeta)$ is a modified Besell function. Most of the energy is radiated in photons of energy near the characteristic value E_c,

$$E_{\rm c} = \frac{3heB(z)\sin\alpha}{4\pi mc}\left(\frac{E}{mc^2}\right)^2. \tag{9}$$

The total power $L_{\rm synchr}\left(E_\gamma\right)$ radiated by an isotropic distribution of particles $N(E,z)$ can then be found as

$$L_{\rm synchr}\left(E_\gamma\right) = E_\gamma \int_V {\rm d}^3 r \int_{\Omega_\alpha} {\rm d}\Omega_\alpha \sin\alpha \int_{E^{\rm min}}^{E^{\rm max}(z)} {\rm d}E\, N(E,z)\, P_{\rm synchr}. \tag{10}$$

The inverse Compton scattering of synchrotron photons by leptons yields a second contribution to the emission spectrum. For a single electron of energy

$E_e = \gamma_e m_e c^2$ in a photon field of density $n\left(\epsilon, z\right)$, the IC emissivity is (Blumenthal & Gould 1970)

$$P_{\rm IC}\left(E_\gamma, E_{\rm e}, \epsilon, z\right) = \frac{3\sigma_{\rm T} c}{4\gamma_{\rm e}^2} \frac{n\left(\epsilon, z\right)}{\epsilon} F\left(q\right). \tag{11}$$

Here $\sigma_{\rm T}$ is the Thomson cross section, and the function $F(q)$ is given by

$$F\left(q\right) = 2q\ln q + \left(1+2q\right)\left(1-q\right) + \frac{1}{2}\left(1-q\right)\frac{\left(q\Gamma_{\rm e}\right)^2}{\left(1+\Gamma_{\rm e}q\right)}, \tag{12}$$

where $\Gamma_{\rm e} = 4\epsilon\gamma_{\rm e}/m_{\rm e}c^2$ and $q = E_\gamma/[\Gamma_{\rm e}E_{\rm e}\left(1 - E_\gamma/E_{\rm e}\right)]$. These expressions are valid even in the Klein-Nishina regime ($\Gamma_e \gg 1$), where the relativistic lepton losses most of its energy in a single collision. The total IC luminosity $L_{\rm IC}(E_\gamma)$ can be calculated as in Eq. (10), integrating in the energy E_e of the electrons and in the energy ϵ of the target photons.

Synchrotron photons also serve as a target field for photohadronic ($p\gamma$) interactions. This process has two main branches: photopair and photomeson production. Photopair production,

$$p + \gamma \rightarrow p + e^- + e^+, \tag{13}$$

was studied among others by Chodorowski et al. (1992), Mücke et al. (2000) and Mastichiadis et al. (2005). In the δ-functional approximation, where each lepton is created with an energy $E_{e^\pm} \sim (m_e/m_p)E_p$, the pair emissivity can be written as

$$\begin{aligned} Q_{e^\pm}\left(E_{e^\pm}, z\right) &= 2\int {\rm d}E_p N_p\left(E_p, z\right)\omega_{p\gamma,\,e^\pm}\left(E_p\right)\delta\left(E_{e^\pm} - \frac{m_e}{m_p}E_p\right) \\ &= 2\frac{m_p}{m_e}N_p\left(\frac{m_p}{m_e}E_{e^\pm}\right)\omega_{p\gamma,\,e^\pm}\left(\frac{m_p}{m_e}E_{e^\pm}\right). \end{aligned} \tag{14}$$

In this expression $N_p(E_p, z)$ is the proton distribution and $\omega_{p\gamma,\,e^\pm}$ is the collision rate,

$$\omega_{p\gamma,\,e^\pm}(\gamma_p) = \frac{c}{2\gamma_p^2}\int_{\frac{\epsilon_{\rm th}}{2\gamma_p}}^{\infty} {\rm d}\epsilon \frac{n\left(\epsilon\right)}{\epsilon^2}\int_{\epsilon_{\rm th}}^{2\epsilon\gamma_p} {\rm d}\epsilon' \sigma_{p\gamma,\,e^\pm}\left(\epsilon'\right)\epsilon'. \tag{15}$$

In our case, $n(\epsilon)$ is the density of the synchrotron photon fields. The threshold energy is $\epsilon_{\rm th} \sim 1$ MeV, and we use the parametrization of the cross section $\sigma_{p\gamma,\,e^\pm}$ given by Maximon (1968).

Photomeson production procceds via two main branches with approximately the same probability,

$$p + \gamma \rightarrow p + a\pi^0 + b\left(\pi^+ + \pi^-\right) \tag{16}$$

and

$$p + \gamma \rightarrow n + \pi^+ + a\pi^0 + b\left(\pi^+ + \pi^-\right), \tag{17}$$

followed by the decays

$$\pi^+ \rightarrow \mu^+ + \nu_\mu, \quad \mu^+ \rightarrow e^+ + \nu_\mathrm{e} + \overline{\nu}_\mu, \tag{18}$$

$$\pi^- \rightarrow \mu^- + \overline{\nu}_\mu, \quad \mu^- \rightarrow e^- + \overline{\nu}_\mathrm{e} + \nu_\mu \tag{19}$$

and

$$\pi^0 \rightarrow 2\gamma. \tag{20}$$

Following Atoyan & Dermer (2003), we calculate the photon and pair emissivity product of the pion decay in the δ-functional approximation,

$$Q_\gamma\left(E_\gamma\right) = 20 N_p\left(10E_\gamma\right) \omega_{p\gamma,\,\pi}\left(10E_\gamma\right) n_{\pi^0}\left(10E_\gamma\right), \tag{21}$$

$$Q_{e^\pm}\left(E_{e^\pm}\right) = 20 N_p\left(20E_{e^\pm}\right) \omega_{p\gamma,\,\pi}\left(20E_{e^\pm}\right) n_{\pi^\pm}\left(20E_{e^\pm}\right). \tag{22}$$

The collision rate $\omega_{p\gamma,\,\pi}$ is given by (14) with the cross section replaced by the correspondent for photomeson production, and n_{π^0} and $n_{\pi^\pm}$ are the mean number of π^0 and $\pi^\pm$ created per proton-photon interaction, respectively. Expressions for all this quantities can be found in Atoyan & Dermer (2003).

All the expressions given above are valid in the comoving reference frame of the jet. To transform them to the observer frame, we must take into account the viewing angle θ and the Lorentz factor of the jet Γ_jet, through the Doppler factor D,

$$D = \frac{1}{\Gamma_\mathrm{jet}\left(1 - \beta_\mathrm{jet}\cos\theta\right)}. \tag{23}$$

Energies and luminosities in the comoving (primed) and the observer (non-primed) frames are then related as

$$E_\gamma = D E'_\gamma \tag{24}$$

and

$$L_\gamma\left(E_\gamma\right) = D^2 L'_\gamma\left(E'_\gamma\right). \tag{25}$$

We fix a moderate value for the viewing angle, $\theta = 30\,\mathrm{deg}$. None of the results depend strongly on this value as long as Γ_jet remains small.

4. Results and discussion

Figure 2 shows some of the calculated spectral energy distributions (SEDs). Proton synchrotron radiation yields a peak in the spectrum around 10 GeV or 10 MeV, depending on the efficiency of the acceleration η, that in turn fixes the proton maximum energy. This component can reach luminosities of $\sim 10^{37}$

erg s^{-1}, almost independently of the value of a. The synchrotron spectra of primary leptons does depend on a, since these particles radiate almost all their energy budget, reaching luminosities in the range $10^{37} - 10^{34}$. Different spectral shapes are obtained depending on the injection spectral index α. The decay of neutral pions and the synchrotron radiation of secondary leptons created through $p\gamma$ collisions contribute to the SEDs at very high energies, up to 10^{16} eV for $\eta = 0.1$. The three contributions are of the same order of magnitude. In any case IC scattering is relevant.

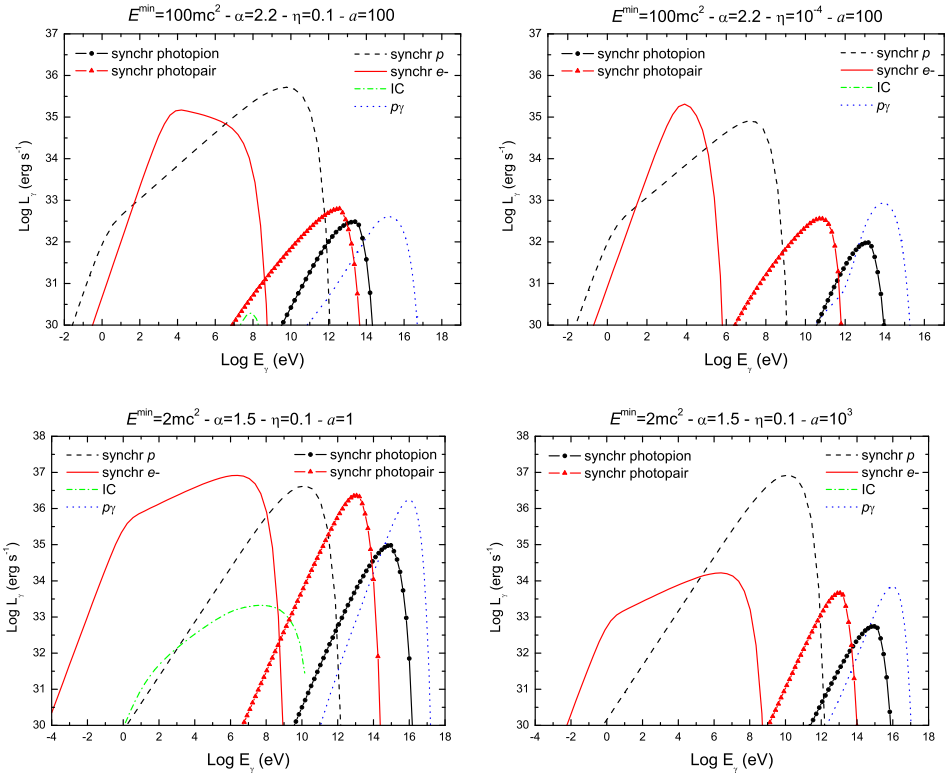

Figure 2. Spectral energy distributions obtained for different values of the parameters.

Since the proton synchrotron peak is always below 1 TeV, its detection by ground-based Cherenkov telescopes is difficult. This componenent might be detected by future gamma-ray satellites like GLAST, that operates in the range 100 MeV to 300 GeV. In cases like the one in the bottom left panel of Fig. 2, however, the contribution of secondary leptons could be detectable by HESS II and MAGIC II. Neutrinos of energies above 1 TeV, a by-product of our model through photomeson production, can also be expected with a luminosity similar to that of the high-energy tail of the calculated SEDs. It is important to note that internal photon-photon absorption can introduce modifications in the production spectra, particularly in cases with a high lepton component ($a = 1$). High-energy photons are very effectively absorbed in the synchrotron field of

primary electrons, leading to the supression of the emission above 10 GeV. For detailed results on this aspect, see Romero & Vila (2008).

5. Conclusions

We have showed that, under certain physical conditions, low-mass microquasars can be efficient gamma-ray sources. This opens up the possibility that some of the unidentified sources in the galactic halo can belong to this class of objects. In future works, we expect to improve our model including refinements in the radiative calculations (see for example Kelner et al. 2008 for the case of $p\gamma$ interactions). We will also go beyond the one-zone model, to achieve a more consistent description of the particle distributions. Finally, we expect to introduce time dependence effects to try to reproduce the observed variability. Observations with forthcoming gamma-ray instruments wil de useful to contrast our predictions, and will contribute with new data that can help to constrain the model parameters.

References

Aharonian, F. A., & Atoyan, A. M. 1998, New Astron. Rev., 42, 579
Aharonian, F. A., et al. 2005, Science, 309, 746
Albert, J., et al. 2006, Science, 312, 1771
Albert, J., et al. 2007, ApJ, 665, L51
Atoyan, A. M., & Aharonian, F. A. 1999, MNRAS, 302, 253
Blumenthal, G. R. & Gould, R. J. 1970, Rev. Mod. Phys., 42, 237
Bosch-Ramon, V., et al. 2006, A&A, 447, 263
Chodorowski, M. J., et al. 1992, ApJ, 400, 181
Grenier, I. A., Kaufman Bernadó, M. M., & Romero, G. E. 2005, Ap&SS, 297, 109
Khangulyan, D., et al. 2007, MNRAS, 380, 320
Levinson, A., & Waxman, E. 2001, Phys. Rev. Lett., 87, 171101
Mastichiadis, A., et al. 2005, A&A, 433, 765
Maximon, L. C. 1968, J. Res. NBS, 72B, 79
Mirabel, I. F., et al. 2001, Nature, 413, 139
Mücke, A., et al. 2000, Comm. Phys. Comp., 124, 290
Ribó, M. et al. 2002, A&A, 384, 954
Romero, G. E., & Vila, G. S. 2008, A&A, astro-ph 0804.4606
Romero, G. E., et al. 2003, A&A, 410, L1

First La Plata International School, 2008
Compact Object and their Emission, 2009
Ileana Andruchow & Gustavo E. Romero, eds.

Spherically-symmetric Accretion onto a Super Massive Black Hole at the Center of a Young Stellar Cluster

Filiberto Hueyotl Zahuantitla, Sergiy Silich & Guillermo Tenorio Tagle

Instituto Nacional de Astrofísica, Óptica y Electrónica , Tonantzintla, 72000 Puebla, México.
hueyotl@inaoep.mx

Abstract. Here we present a self-consistent, bimodal stationary solution for spherically-symmetric flows driven by young massive stellar clusters with a central supermassive black hole (SMBH). We show that the gravity of the BH separates the flow into two distinct zones: the inner accretion zone and the outer zone where the star cluster wind is formed.

We compared the calculated accretion rates with those predicted by the classic Bondi accretion theory and found that Bondi's theory is in good agreement with our results in the case of low mass clusters. However, it substantially underestimates the accretion rates and then the BH luminosities if the star cluster mechanical luminosity $L_{\rm SC} \geq 0.1 L_{\rm crit}$.

1. Introduction

Intensive studies of active galactic nuclei (AGNs) in the optical, radio (Baum et al. 1993), infrared (Rodríguez Espinosa et al. 1987) and X-ray regimes (Levenson et al. 2001), have unveiled the presence of a massive starburst around the central SMBH in a number of Seyfert galaxies.

Heckman et al. (1997) and González Delgado et al. (1998) found in the optical regime, absorption line features associated with the photospheres of O and B stars and their stellar winds in the spectra of four Seyfert 2 galaxies and thus presented direct evidence for the existence of nuclear starbursts in these galaxies.

On the other hand, compact, bright stellar clusters, were found in the centers of local spirals and Virgo dwarf elliptical galaxies (Côte et al. 2006). Their radii (a few parsecs) are similar to those of globular clusters, however they are 1–2 orders of magnitude brighter and more massive. Seth et al. (2008) found that in many cases masses of the nuclear clusters and the embedded BHs are quite similar, whereas Ferrarese et al. (2006) claimed that massive galaxies host SMBHs whereas less massive galaxies host only nuclear clusters.

Tan & Blackman (2005, see also references therein) have shown that accretion disks are gravitationally unstable outside of $r \sim 10^{-2}$ pc, and must fragment into self-gravitating clumps that eventually form stars. It was suggested that star formation reduces the accretion rate and thus the luminosity of the SMBH by removing mass from the accretion flows and also due to radiative heating of the accretion disk. However none of these models considered the negative feedback provided by the mechanical energy of the central starburst on the accretion flow.

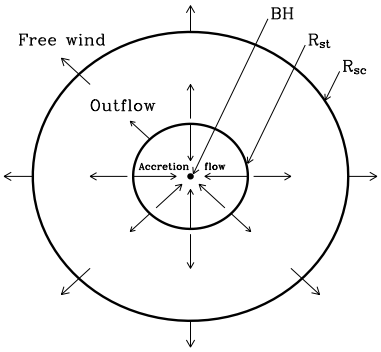

Figure 1. The structure of the bimodal flow that results from the thermalization of the supernova ejecta and stellar winds inside a young stellar cluster with a central SMBH. The radii of the internal and the external circles represent the stagnation radius $R_{\rm st}$ and the star cluster radius $R_{\rm SC}$, respectively. The arrows indicate the direction of the flow. The black dot at the center marks the position of the black hole.

Here we note that the mechanical power of young nuclear starbursts might prevent, through the cluster winds, the accretion of interstellar matter from the bulges and disks of their host galaxies onto the BH. In such cases the BHs are fed with the matter injected by the massive members of the nuclear cluster. This implies that nuclear starbursts might strongly affect and perhaps even control the power of the central BH. In fact, it may be the dominant factor to be considered to estimate the energy budget of the composite AGN/starburst galaxies.

The classic spherically-symmetric accretion model (Bondi, 1952; Frank et al. 2002) should be modified if one is to apply it to the case of a massive BH at the center of a young stellar cluster. First, it should take into consideration the energy and mass supplied by massive stars within the cluster volume. Second, it should account for radiative losses of energy from the hot plasma. Third, the models should incorporate the appropriate initial and boundary conditions as those described by the star cluster wind theory (Chevalier & Clegg, 1985; Cantó et al. 2000; Silich et al. 2004; Tenorio-Tagle et al. 2007).

Here we present a self-consistent model for stationary, spherically-symmetric flows driven by the thermalization of the kinetic energy supplied by massive stars inside stellar clusters, which includes the outflow of the injected matter and its accretion onto a central massive BH.

The paper is organized as follows. In section 2 we formulate our model and discuss the input physics and major simplifications. In section 3 we present a set of major equations. Boundary conditions and the selection of the proper solution are discussed in section 4. In section 5 we use our model to calculate the accretion rates, and compare them to those predicted in the classic Bondi accretion theory. Section 6 summarizes our results and gives our conclusions.

2. The model

Following Chevalier & Clegg (1985) we assume that massive stars are homogeneously distributed inside a spherical volume of radius $R_{\rm SC}$ and that the mechanical energy deposited through stellar winds and supernovae, $L_{\rm SC}$, is thermalized via random collisions of the gaseous streams from neighboring sources. This results in a high temperature and a high thermal pressure that leads to a fast outflow of the injected matter, while composing a stationary star cluster wind.

In presence of a massive, central black hole, a fraction of the deposited matter is to remain bound inside the cluster to eventually fall onto the center. This implies that in presence of a BH, the stagnation point, the point where the expansion velocity u is zero is at a distance $R_{\rm st}$, from the center. The position of the stagnation point thus becomes an important issue that defines both the upper limit for the accretion rate onto the BH, and the amount of matter that the cluster returns, in the form of a wind, to the ISM (see Silich et al. 2008).

We neglect all effects associated with the redistribution of the residual angular momentum. We do not consider relativistic effects and stop our integration at the last stable orbit around the central BH, the Schwarzschild radius $R_{\rm Sh} = 2GM_{\rm BH}/c^2$, where, $M_{\rm BH}$ is the black hole mass, c is the speed of light and G is the gravitational constant. Throughout the calculations the parameters of the cluster, and the mass of the central BH, are not allowed to change and thus only stationary solutions are discussed.

We consider only star clusters for which the stationary solution exists ($L_{\rm SC} \leq L_{\rm crit}$), see Silich et al. 2004. Above the critical luminosity, the thermalized plasma inside the cluster is thermally unstable and the flow has a very complicated time-dependent velocity pattern and is expected to be re-processed into new generation of stars (Tenorio-Tagle et al. 2007, Wünsch et al. 2008).

Figure 1 presents a schematic representation of the structure of the bimodal flow. A fraction of the mater supplied by SNe and stellar winds is captured by the BH and the rest is ejected as a star cluster wind into the ambient ISM.

3. Main Equations

The hydrodynamic equations for the model described above in the case of a massive cluster with radius $R_{\rm SC}$, mass $M_{\rm SC}$, mechanical luminosity $L_{\rm SC}$ and with a central BH with mass $M_{\rm BH}$, are

$$\frac{1}{r^2}\frac{d}{dr}\left(\rho u r^2\right) = q_{\rm m}, \tag{1}$$

$$\rho u \frac{du}{dr} = -\frac{dP}{dr} - q_{\rm m} u - \frac{G\rho(M_{\rm BH} + M(r))}{r^2}, \tag{2}$$

$$\frac{1}{r^2}\frac{d}{dr}\left[\rho u r^2 \left(\frac{u^2}{2} + \frac{\gamma}{\gamma - 1}\frac{P}{\rho}\right)\right] = q_{\rm e} - Q - \frac{G\rho u(M_{\rm BH} + M(r))}{r^2}, \tag{3}$$

and

$$\frac{1}{r^2}\frac{d}{dr}\left(\rho u r^2\right) = 0, \tag{4}$$

$$\rho u\frac{du}{dr} = -\frac{dP}{dr} - \frac{G\rho(M_{\rm BH}+M_{\rm SC})}{r^2}, \tag{5}$$

$$\frac{1}{r^2}\frac{d}{dr}\left[\rho u r^2\left(\frac{u^2}{2}+\frac{\gamma}{\gamma-1}\frac{P}{\rho}\right)\right] = -Q - \frac{G\rho u(M_{\rm BH}+M_{\rm SC})}{r^2}, \tag{6}$$

for $r < R_{\rm SC}$ and $r \geq R_{\rm SC}$, respectively. P, u, and ρ in equations (1–6) are the thermal pressure, velocity and density of the thermalized matter. $q_{\rm m} = 3\dot{M}_{\rm SC}/4\pi R_{\rm SC}^3$ and $q_{\rm e} = 3L_{\rm SC}/4\pi R_{\rm SC}^3$ are the mass and the energy deposition rates per unit volume. $Q = n_{\rm e}n_{\rm i}\Lambda(T,Z)$ is the cooling rate, where $n_{\rm e}$ and $n_{\rm i}$ are the electron and ion number densities, respectively; $\Lambda(T,Z)$ is the cooling function, T is the temperature and Z is the metallicity of the plasma. The mechanical luminosity is $L_{\rm SC} = \dot{M}_{\rm SC}V_{A\infty}^2/2$, where $V_{A\infty}$ is the adiabatic wind terminal speed. $M(r) = M_{\rm SC}(r/R_{\rm SC})^3$ tracks the stellar mass distribution within the spherically-symmetric cluster, and $M_{\rm BH}$ is the mass of the BH. We have taken into consideration the gravitational pull provided by the BH and the cluster and neglected the self-gravity of the reinserted gas.

One can rewrite equations (1–6) in form:

$$\frac{du}{dr} = \frac{1}{\rho}\frac{(\gamma-1)(q_{\rm e}-Q)+q_{\rm m}\left[\frac{\gamma+1}{2}u^2 - \frac{2}{3}\left(1-\frac{R_{\rm st}^3}{r^3}\right)\left(c_s^2 - V_{esc}^2(r)/4\right)\right]}{c_{\rm s}^2-u^2}, \tag{7}$$

$$\frac{dP}{dr} = -\rho u\frac{du}{dr} - q_{\rm m}u - \frac{G\rho(M(r)+M_{\rm BH})}{r^2}, \tag{8}$$

$$\rho = \frac{q_m r}{3u}\left(1-\frac{R_{\rm st}^3}{r^3}\right), \tag{9}$$

within the cluster volume, $r \leq R_{\rm SC}$, and

$$\frac{du}{dr} = \frac{2u}{r}\frac{2\pi(\gamma-1)Qr^3/\dot{M}_{\rm SC} + c_{\rm s}^2 - V_{\rm esc}^2/4}{u^2-c_{\rm s}^2}, \tag{10}$$

$$\frac{dP}{dr} = -\frac{\dot{M}_{\rm SC}}{4\pi r^2}\frac{du}{dr} - \frac{G\dot{M}_{\rm SC}(M_{\rm SC}+M_{\rm BH})}{4\pi r^4 u} = -\frac{\dot{M}_{\rm SC}}{4\pi r^2}\left[\frac{du}{dr}+\frac{V_{\rm esc}^2}{2ru}\right], \tag{11}$$

$$\rho = \frac{\dot{M}_{\rm SC}}{4\pi u r^2}, \tag{12}$$

in the region $r > R_{\rm SC}$. The escape velocity is $V_{esc} = [2G(M(r)+M_{\rm BH})/r]^{1/2}$ if $r \leq R_{\rm SC}$, and $V_{\rm esc} = [2G(M_{\rm SC}+M_{\rm BH})/r]^{1/2}$ if $r > R_{\rm SC}$.

The presence of the BH does not affect the relation between the gas number density and the temperature at the stagnation point found in Silich et al. (2004):

$$n_{\rm st} = q_{\rm m}^{1/2}\left[\frac{V_{A\infty}^2/2 - c_{\rm st}^2/(\gamma-1)}{\Lambda(Z,T_{\rm st})}\right]^{1/2}. \tag{13}$$

Note that Sarazin & White (1987) obtained a similar relation from the energy conservation equation in their cooling flow model.

In all calculations we use the equilibrium cooling function for optically thin plasma tabulated by Plewa (1995) and assume that the metallicity of the plasma is solar.

4. Boundary conditions and the appropriate integral curve

The smooth transition from the subsonic expansion of the thermalized ejecta, inside the star cluster, to the supersonic free wind at $r > R_{\rm SC}$, requires (see equations 7 and 10) the sonic point to be located at the star cluster surface (see Cantó et al. 2000; Silich et al. 2004). Hereafter we will refer to this sonic point as the *outer* sonic point.

The presence of the central BH, prevents the escape of the injected matter from the central zones of the cluster and thus shifts the stagnation point out of the star cluster center. In this case all mass continuously deposited by the cluster inside the stagnation radius, cannot escape from the gravitational well of the BH and composes the accretion flow. The presence of the BH results also in the existence of a second sonic point, inside the stagnation radius. We will refer to it as the *inner* sonic point.

Thus, the stagnation radius defines the upper limit to the accretion rate onto the central BH, and also the fraction of mass that the cluster returns to the ambient ISM. This implies that the major problem that one has to solve in order to build a self-consistent solution for the flow is reduced to the calculation of the stagnation radius.

In order to select a proper integral curve we take a trial stagnation radius and then select $T_{\rm st}$ from our first boundary condition which requires the outer sonic point to be located at the star cluster surface (see Silich et al. 2004; Tenorio-Tagle et al. 2007). We calculate then the number density of the plasma at the stagnation radius from equation (13) and use these $R_{\rm st}$, $T_{\rm st}$ and $n_{\rm st}$ as initial conditions to the backward integration from $R_{\rm st}$ towards the center (Silich et al. 2008). The right panel in Figure 2, shows that the *inner* sonic point moves inwards to the star cluster center, as one considers smaller stagnation radii. To avoid numerical problems associated with the central singularity and relativistic effects, we stop the integration at the last stable orbit associated with the BH. Then, the second boundary condition is: $R_{\rm sonic,in} = 3R_{\rm Sh}$.

Figure 2 (left panel), presents the backward integral curves for different values of the trial stagnation radius. If the selected $R_{\rm st}$ is too large, the backward integration leads to a double-valued, unphysical solution, marked by the dashed line. In this case the velocity turnoff point (marked by a cross symbol) coincides with the inner sonic point far from the cluster center. The turnoff point moves towards $r = 3R_{\rm Sh}$ when the considered $R_{\rm st}$ is smaller (Figure 2 right panel). This finally leads to an integral curve (solid line) with the sound speed at $r = 3R_{\rm Sh}$. For even smaller $R_{\rm st}$ the stagnation density is larger and the accretion velocity may even go to zero (dotted line). We select as the proper solution, the integral curve for which the parameters at the stagnation radius fulfill the two boundary conditions.

Figure 3 (left panel), presents the proper solution for a particular case of a $10^8 M_\odot$ black hole located at the center of a young stellar cluster whose mass and radius are $M_{\rm SC} = 10^8 M_\odot$ and $R_{\rm SC} = 40$pc. In this case the stagnation radius, marked by the inner dotted line, is $R_{\rm st} = 2.7$pc. At larger radius the velocity grows almost linearly to reach the sonic value at the star cluster surface and then becomes supersonic outside the cluster approaching to the terminal value.

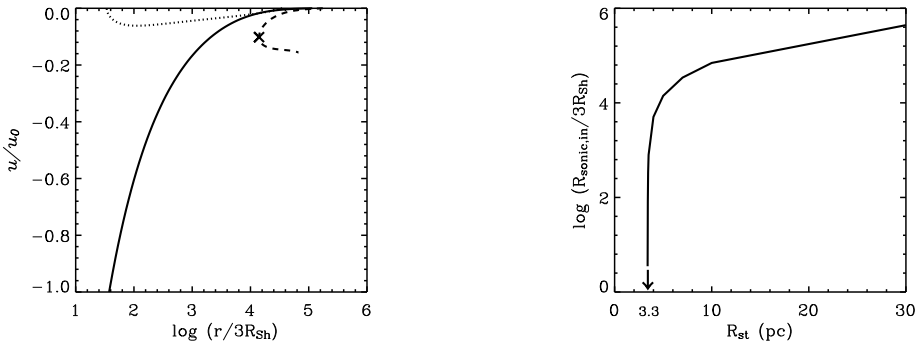

Figure 2. *Left:* possible integral curves. Dashed, solid and dotted lines corresponds to different stagnation radii: 5 pc, 3.3 pc and 1 pc, respectively. The description of these integral curves is given in the text. We assumed in the calculations $R_{\rm SC} = 100$ pc, $M_{\rm SC} = 10^8 M_\odot = M_{\rm BH}$ and $V_{A\infty} = 1500$ km s^{-1}. The normalization velocity is $u_0 = 10^4$ km s^{-1} for the solid line, the dashed and dotted lines are scaled conveniently just to compare the shape of the profiles. *Right:* location of the inner sonic point for different stagnation radius. In this particular case $R_{\rm sonic,in} = 3R_{\rm Sh}$ for $R_{\rm st} = 3.3$ pc. The parameters for the star cluster and the BH are the same as in the left panel.

In the region between the stagnation radius and the black hole, the matter deposited by stellar winds and SNe composes a stationary accretion flow.

5. Accretion rates

The mass deposited by stellar winds and SNe inside $R_{\rm st}$ is not able to escape and, in the stationary regime, falls to the center providing fuel to the BH. Thus in the stationary regime the stagnation radius, $R_{\rm st}$, defines the accretion rate onto de BH:

$$\dot{M}_{\rm acc} = \dot{M}_{\rm SC} \left(\frac{R_{\rm st}}{R_{\rm SC}} \right)^3 . \tag{14}$$

In this respect it is instructive to compare our model with the classic Bondi accretion theory (Bondi, 1952; see Frank et al. 2002 and references therein). If the polytropic index is $\gamma = 5/3$, the Bondi accretion rate is:

$$\dot{M}_{\rm B} = \pi G^2 M_{\rm BH}^2 \frac{\rho_{\rm ISM}}{c_{\rm ISM}^3}, \tag{15}$$

where $\rho_{\rm ISM}$ and $c_{\rm ISM}$ are the density of the ISM and the speed of sound at infinity, respectively. To compare with our model and to see the effect of the star cluster on the accretion rates we associate $\rho_{\rm ISM}$ and $c_{\rm ISM}$ with Chevalier & Clegg's central values (see Cantó et al. 2000) :

$$\rho_c = \frac{2}{4\pi A} \frac{L_{\rm SC}}{R_{\rm SC}^2 V_{A\infty}^3}, \quad c_c = \sqrt{\frac{\gamma-1}{2}} V_{A\infty}, \quad A = \left(\frac{\gamma-1}{\gamma+1} \right)^{1/2} \left(\frac{\gamma+1}{6\gamma+2} \right)^{(3\gamma+1)/(5\gamma+1)} . \tag{16}$$

In Figure 3, right panel, we compare our semi-analytic results (equation 14) with the "modified" Bondi accretion rates (equation 15) using $\rho_{\rm c}$ and $c_{\rm c}$. The

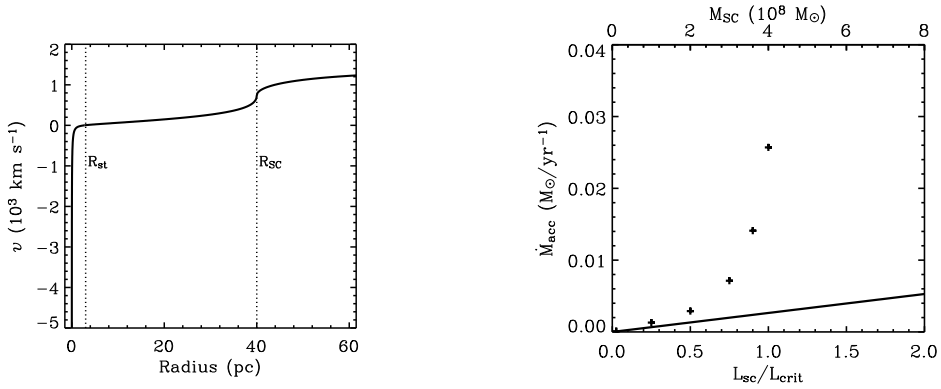

Figure 3. *Left:* the bimodal flow that results from the thermalization of the supernova ejecta and stellar winds inside a star forming region with a SMBH at the center. In this case $R_{\rm SC} = 40$ pc and $M_{\rm SC} = 10^8 M_\odot = M_{\rm BH}$, the stationary solution sets in for $R_{\rm st} = 2.7$ pc. *Right:* comparison of the approximate analytic formulae with our semi-analytic accretion rates. Cross symbols, represent the semi-analytic results for a $10^8 M_\odot$ BH embedded into stellar clusters of different masses, all having radius of $R_{\rm SC} = 40$ pc. Solid line displays the accretion rates calculated using the Bondi approximation with the adiabatic input parameters.

semi-analytic results are marked by the cross symbols and the accretion rates predicted by the Bondi equation are shown by the solid line. Note that for low mass star clusters Bondi's formula is in good agreement with our results.

One can then use equation (15) with equations (16) in order to obtain an analytic expression for the stagnation radius in the case of low mass star clusters ($L_{\rm SC} \ll L_{\rm crit}$). Indeed, the mass accretion rate is

$$\dot{M}_{\rm acc} = 4\pi q_{\rm m} R_{\rm st}^3/3, \tag{17}$$

by doing $M_{\rm B} = M_{\rm acc}$, one can obtain:

$$R_{\rm st} = \left(\frac{\pi G^2 V_{A\infty}^2 M_{\rm BH}^2 \rho_{\rm c}}{2 L_{\rm SC} c_{\rm c}^3}\right)^{1/3} R_{\rm SC}. \tag{18}$$

For star clusters whose mechanical luminosity is comparable to the critical value, $L_{\rm crit}$, the calculated accretion rates exceed substantially those predicted by Bondi's formula. In this case one must use the semi-analytic model in order to find the size of the stagnation zone and then, equation (14) in order to derive the accretion rate.

6. Conclusions

We have developed a self-consistent, stationary solution for spherically symmetric flows which are formed inside young stellar clusters with a central SMBH. We have shown that the thermalization of the kinetic energy inside young stellar

clusters results in a bimodal solution which presents an accretion of the injected matter onto a central BH in the inner zones, and the ejection of the deposited matter from the outer zones of the cluster in the form of a fast superwind. We suggest that superwinds prevent the accretion of the ambient interstellar gas from the bulges and disks of their host galaxies onto the central BHs and that in such cases the BHs are fed with the matter re-inserted by massive stars via stellar winds and SN ejecta. Thus, both the BH and the central starburst compete in defining the accretion rate and the BH luminosity.

The classic, Bondi's accretion formula shows a good agreement with our semi-analytic model, but only in the case of low mass clusters ($L_{\rm SC} \leq 0.1 L_{\rm crit}$). Thus one has to use a semi-analytic approach in order to calculate the accretion rates and BH luminosities in the case of more energetic clusters.

For star clusters with $L_{\rm SC} \geq L_{\rm crit}$, the strong radiative cooling makes the flow thermally unstable and thus the solution of the hydrodynamic equations requires fully numerical calculations.

The model, here developed, is required in order to improve our knowledge regarding the relative contributions of super massive BHs and central starbursts in composite, AGN/starburst galaxies, and will be used for the interpretation of observational properties of such objects in a further communication.

Acknowledgments. FHZ wishes to express his thanks to CONACyT - México for the financial support by the master grant 12442.

References

Baum, S. A. et al. 1993, ApJ, 419, 553
Bondi, H. 1952, MNRAS, 112, 195
Cantó, J., Raga, A. C., & Rodríguez, L. F. 2000, ApJ, 536, 896
Chevalier, R. A., & Clegg, A. W. 1985, Nature, 317, 44
Côte, P. et al. 2006, ApJS, 165, 57
Ferrarese, L., et al. 2006, ApJ, 644, L21
Frank, J., King, A., & Raine, D. 2002, "Accretion Power in Astrophysics.", Cambridge University Press.
González Delgado, R. M. et al. 1998, ApJ, 505, 174
Heckman, T. et al. 1997, ApJ, 482, 114
Leitherer, C. et al. 1999, ApJS, 123, 3
Levenson, N. A., Weaver, K. A., & Heckman, T. M. 2001, ApJ, 550,230
Plewa, T. 1995, MNRAS, 275, 143
Rodríguez Espinoza, J. M., Rudy, R. J. & Jones, B. 1987, ApJ, 312, 555
Sarazin, C. L. & White, R. E. III 1987, ApJ, 320, 32
Seth, A., et al. 2008, ApJ, 678, 116
Silich, S., Tenorio-Tagle, G., & Rodríguez-González, A. 2004, ApJ, 610, 226
Silich, S., Tenorio-Tagle, G., & Hueyotl-Zahuantitla, F. 2008, ApJ, 686, 172
Tan, J. C. & Blackman, E. G. 2005, MNRAS, 362, 983
Tenorio-Tagle, G., et al. 2007, ApJ, 658, 1196
Wünsch, R., et al. 2008, ApJ, 683, 683

First La Plata International School, 2008
Compact Object and their Emission, 2009
Ileana Andruchow & Gustavo E. Romero, eds.

Power and morphology of AGN Hosts

Sol Molina [1], Diego García Lambas[2,3,5], M. Sol Alonso[3,4] & Carlos Bornancini[2,5]

[1] *FCEFyN;* [2] *IATE;* [3] *CONICET;* [4] *CASLEO,* [5] *UNC*
atenea-snm@yahoo.com.ar

Abstract.

The aim of this work is the study of the relation between nuclear activity in AGNs and Host morphology. For this purpose we extracted AGN data from Kauffmann et al. (2003) catalogue and we analysed two AGN subsamples absolute r band magnitude -21<Mr<-22 and redshifts in the range 0.03<z<0.1. We extracted i band images of these AGNs from the Sloan Digital Sky Survey Data release 5 (SDSS-DR5) and used SExtractor routines to calculate the concentration (C) and the asymmetry (A) parameter given in Conselice (2003). We adopted the photometric system in SDSS-DR5, u,g,r,i and z bands (Fukuyita et al. 1996; Gunn et al. 1998; Hogg et al. 2001; Smith et al. 2002).The concentration index provides a useful measure of the light distribution across the galaxy, while the asymmetry index is sensitive to signs of interactions or mergers. By analysing the specific star formation rate (SFR/M∗) and the population age diagnostic index Dn_{4000} we find that powerful AGN hosts exhibit some signs of interactions, high values for SFR/M∗ and younger stellar population. Thus, our results indicate that galaxy-galaxy interactions or strong tidal perturbations play a crucial role in triggering and powering AGN phenomena.

1. Introduction

In order to explain powerful AGNs it is central to understand the processes that can feed effectively the black holes in the center of galaxies. These processes must be able to transfer material to the center of the galaxy and then this material must lose angular momentum to feed the central black hole. The most accepted mechanisms are interactions or processes related with the morphology of the galaxy such bars and nuclear spirals.

Ho et al. (1997) showed that different activity types have different distributions of morphological types. A significant percentage of LINERs and transition galaxies are found in elliptical or S0 host, and almost all HII galaxies and high percentage of Seyferts have morphological types Sa or later. Kauffmann et al. (2003) found that type 2 AGNs reside almost exclusively in massive galaxies, and the AGN fraction declines very strongly at stellar masses below 10^{10} solar masses. They obtain similar sizes and stellar mass distribution for AGNs and for normal early-types galaxies, and the age distribution in AGNs is a strong function of [OIII] luminosity. High power AGNs (Log (Lum[OIII]) > 7) show

somewhat younger stellar populations, and these high power AGNs have lower density environments.

2. Mechanisms to feed central black holes

2.1. Bars and nuclear spirals

According to Márquez (2008) a bar is described as a component that ridigly rotates on a differentially rotating disk, giving rise to different resonances usually associated to ring features. Bars dynamically heat the disk and produce net inflows to the central regions. There is no consensus about the importance of bars in the feeding of black holes. There are studies (Maia et al. 2004) that shown a higher proportion of Seyfert galaxies with bars compared to the proportion of normal galaxies with bars. On the other hand, in several works it is concluded that there is not an excess of Seyfert galaxies with bars (Mulchaey et al., 1997). These different results could be originated by sample selection effects, image bands, etc. Márquez (2008) proposes an scenario where late type spirals may suffers a small disk perturbation, a minor merger or interaction where a bar is generated inducing the transport of some disk material to the center. However, this process enhances the bulge component and destroys the bars themselves so that the galaxy ends up as an earlier unbarred galaxy.

2.2. Interactions

Interactions between galaxies can play an important role in feeding AGNs. N-body simulations by Mihos et al. (1994), Taniguchi & Wada (1996), and others, have concluded that mergers, minor mergers and flybys can effectively bring gas from the disk to the central region. During this process the gas is shocked and compressed, temperature and density increase and the star formation is enhanced, then the gas loses more angular momentum and is accreted by the black hole, and the galaxy is detected as an AGN. There is evidence that high luminosity sources, like quasars, are related to interacting systems (Canalizo & Stockton 2001). But in the case of lower luminosity sources there is no consensus on the importance of interactions in feeding the nuclear region.

In some observational works (e.g.,Fuentes-Williams & Stocke 1988, De Robetis et al. 1998, etc.) it was found a similar relative number of AGNs and normal galaxy companions of Seyfert or normal galaxies. Nevertheless, other works (Laurikainen et al., 1995) indicate a larger number of companions around Seyfert 2 than in Seyfert 1 galaxies, while Simkin, Su & Schwarz (1980), Laurikainen et al. (1994), and others, find an excess of Seyfert galaxies with companions relative to normal galaxies. Furthermore, Alonso et al. (2007) estimate the mean accretion rates onto the black holes finding that AGNs in pairs ongoing a merging process (projected relative distance $r_p < 100$ kpc h^{-1}, relative velocity $\Delta V < 350$ km s^{-1} and with evidence of an ongoing merging process) have more active black holes than other types of pairs. This means that the proximity between galaxies can affect the central black hole activity.

In order to explain these diverse results Corbin (2000) and Schmitt (2001) argue that there is a delay between the time when the interaction moves toward the nucleus and that when the gas is being accreted by the nuclear black hole

implying a strong time evolution of AGNs. Schmitt (2004) proposes that when an interaction happens galaxies can pass through different periods of activity. First, it is possible to detect an HII nucleus region, when the gas is being accreted by the black hole at a high rate, then the galaxy could evolve into Seyfert activity, and finally become a LINER or transition galaxy when the amount of gas is small. To test the importance of interaction in this scenario it is important to compare the asymmetry indices (Conselice 2003) estimated for Seyfert and normal galaxies. Thus, we would expect to find larger asymmetries in Seyfert galaxies compared to normal ones if interactions play an important role in feeding AGNs.

While galaxies undergoing mergers or interactions may exhibit peculiar morphological disturbances, such as tidal tails, merger remnants may also show relic structures from their previous interactions, such as shells or ripples. De Propis et al. (2007) use this fact to compare the use of galaxy asymmetry and pair proximity for measuring galaxy merger fractions. They find that galaxies in close pairs are generally more asymmetric than isolated galaxies and the degree of asymmetry increases for closer pairs. Furthermore they find that among asymmetric galaxies at least 80 percent are either interacting systems or merger remnants. The most important of this facts is that the asymmetry is a suitable indicator of interactions between galaxies. This is our main reason to study the asymmetry/concentration parameters in AGNs.

3. SDSS-DR5 data and Kauffmann et al. (2003) catalogue

The Sloan Digital Sky Survey (SDSS) mapped one quarter of the entire sky in five optical bands and perform a redshift survey of galaxies, quasars and stars. The Data Releases 5, DR5 (Adelman-McCarthy et al., 2007) is the fifth major data release and provides images, imaging catalogs, spectra, and redshifts for download. The imaging portion comprises 8000 square degrees of sky imaged in five wave-bands u, g, r, i and z (Fukuyita et al. 1996; Gunn et al. 1998; Hogg et al. 2001; Smith et al. 2002) containing photom

From SDSS, Kauffmann et al. (2003) have constructed a catalogue with a subset of 122.808, narrow emission line galaxies, within redshift range $0.02 < z < 0.3$. Kauffmann et al. (2003) obtain 22.623 galaxies classified as AGN and take into account the relation between spectral lines [OIII]λ 5007/Hβ[OIII] and [NII]λ 6583/Hα to define an AGN.

$$log([OIII]/H\beta) > 0.61/(log([NII]/H\alpha) - 0.05) + 1.3 \quad (1)$$

They exclude type 1 AGN from their initial sample and take into account only type 2 AGN where only the narrow line region can be observed due to the obscuring medium.

3.1. Our sample

We extracted a sample of type 2 AGN$'s$ from the Kauffmann et al. (2003) catalogue. We selected galaxies with magnitudes in the r filter $-21 < M_{\rm r} < -22$ and redshift in the range $0.03 < z < 0.1$. Kauffmann et al. (2003) use the [OIII] λ 5007 emission line as a tracer of the strength of activity in the

nucleus. We selected galaxies with log(Lum[OIII]) > 8 (powerful AGNs) and log(Lum[OIII]) < 5.5 (weak AGNs) and we create two subsamples with these galaxies. The purpose of this division is to compare morphological properties and nuclear activity between galaxies with high and low central activity.

3.2. Concentration and asymmetry parameters

We performed a photometrical analysis of the AGN sample by the application of SExtractor routines in images extracted from SDSS DR5. We measure the concentration (C) and asymmetry (A), parameters defined by Conselice (2003), in galaxies nearly face-on which provide the best conditions to extract useful information.

In accordance with Conselice (2003) these two parameters and the clumpiness (S) index define a new classification system that set objects according to their most salient physical or evolutionary properties and processes.

The concentration index is a measure of the relative galaxy components scale and reveals the past formation history of a galaxy.

The asymmetry index is sensitive to any signs of interactions or merger.

Finally, the clumpiness index measures the patchiness of the light distribution in a galaxy. We applied SExtractor routines for measuring the concentration (C) and the asymmetry (A) index, on 100 images, 50 powerful and 50 weak AGNs. We have chosen the objects at random to exclude possible selection effects. The results are shown in Figure 1 where we can observe a systematic difference between hosts of powerful (red points) and weak (black points) AGNs. Powerful AGN hosts have larger asymmetries than weak AGN hosts. In order to quantify the robustness of our results, we have computed the fraction of A values in the powerful AGN subsample that are greater than the median of the weak AGN subsample. We find 40 objects which correspond to 3 standard deviations with respect to the 25 expected if the distributions where similar. Therefore we estimate that the two distributions differ at a 99 % confidence level. As we know the asymmetry parameter is related with galaxy perturbations and in accordance with De Propis et al. (2007), larger asymmetry values can be identified with both merger remnants as well as ongoing mergers. We conclude that powerful AGNs have either been significantly perturbed or have suffered a strong interaction.

3.3. The specific star formation rate (SFR/M$*$)

Galaxy interactions are known to be an effective mechanism that regulate the star formation activity in galaxies. Since AGN activity and star formation frequently appear together in galaxies, they could both be physically connected to interactions.

In Figure 2-a we show the relation between log[Lum[OIII]] and the specific star formation rate (SFR/M$*$). The blue points correspond to all AGNs in Kauffmann et al. (2003) catalogue with -21 < $M_{\rm r}$ < -22 and 0.03 < z < 0.1. We can see that AGNs with low log[L[OIII]] values have a large range of SFR/M$*$, while powerful AGNs only show high SFR/M$*$ values. We also show in this figure these parameters for our powerful (red points) and weak (black points) AGN samples.

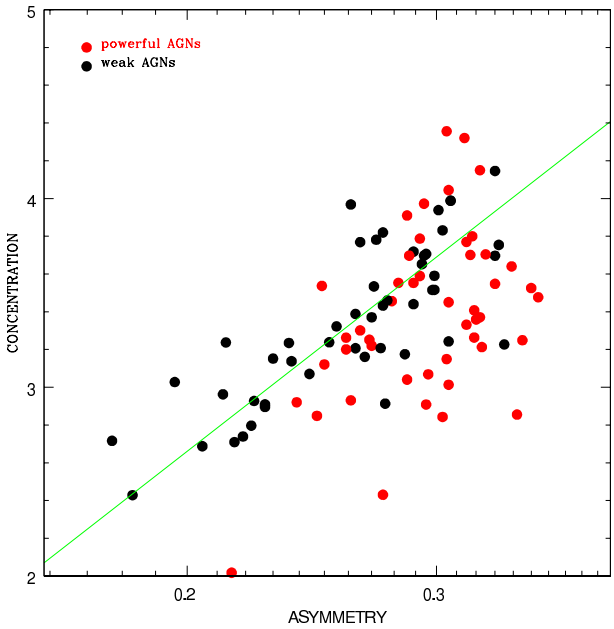

Figure 1. Concentration as a function of the asymmetry. Red points represent powerful AGNs and black points represent weak AGNs. Green line is the median of the weak AGN subsample.

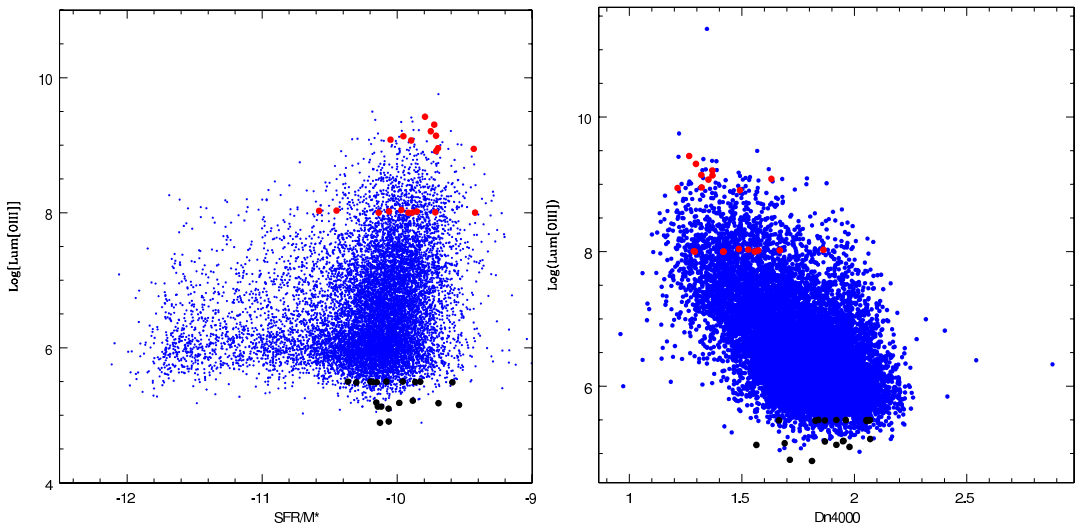

Figure 2. *Left:* a. log(Lum[OIII]) as function of SFR/M∗.
Right: b. log(Lum[OIII]) as function of Dn_{4000}.

3.4. The Dn_{4000} parameter

The Dn_{4000} parameter provides a suitable age indicator of the star population, in the sense that low values correspond to population of recently formed stars.

We show in Figure 2-b the relation between log[Lum[OIII]] and Dn_{4000}. Colours are as in Figure 2-a. In agreement with results obtained from Kauffmann et al. (2003), we see that powerful AGNs have younger stellar populations than weak AGNs.

We argue that the powerful AGNs have experienced strong perturbations by galaxy interactions, exhibiting high frequency structures, strong star formation activity and younger stellar populations.

4. Conclusion

The purpose of this analysis is to contribute to the understanding of the host morphologic signatures that keep clues on nuclear activity. We have compared host properties of powerful and weak AGNs. We found that powerful AGN hosts have larger asymmetries than weak AGN hosts, larger SFR/M* and younger stellar populations. This scenario can be generated by galaxy interactions in agreement with Alonso et al. (2007) findings. Our results show that a strong nuclear activity is correlated with high frequency structures, high star formation rates and young stellar population. These results are in general agreement with current structure formation models where the interactions are the principal processes for feeding the central black hole in AGNs.

References

Adelman-McCarthy, et al. 2007, ApJS, 172, 634
Alonso, et al. 2007, MNRAS, 375, 1017
Canalizo, G. & Stockton, A. 2001, ApJ, 555, 719
Conselice, C. J. 2003, ApJS, 147, 1
Corbin, M. R. 2000, ApJ, 536, L73
De Propis, R., et al. 2007, ApJ, 666, 212
De Robetis, M., et al. 1998, ApJ, 496,43
Fukugita, M., et al. 1996, AJ, 111, 1748
Fuentes-Williams, T. & Stocke, J. T. 1988, AJ,96,1235
Gunn, J., Carr, M., et al. 1998, ApJ, 116, 3040
Ho, et al. 1997, ApJ,487,568
Hogg, D., et al. 2001, AJ, 122, 2129
Kauffmann, G., et al. 2003, MNRAS, 346, 1055
Laurikainen, E., et al. 1994, A&AS, 108,491
Laurikainen, E., et al. 1995, A&A, 293,683
Maia, M., et al. 2004, IAUS, 222, 435N
Márquez, I. 2008, RevMexAA, 32, 150-154
Mihos, J. C., et al. 1994, ApJ, 425, L13
Mulchaey, J. S., et al. 1997, ApJ, 482, 135
Schmitt, H. 2001, AJ, 122, 2243

Schmitt, H. 2004, IAUS, 222,395S
Simkin, S. M., Su, H. J., & Schwarz, M. P. 1980, ApJ, 237,404
Smith, J. A., et al. 2002, AJ, 123, 2121
Strauss, M., et al. 2002, AJ,124,1810.
Taniguchi, Y. & Wada, K. 1996, ApJ, 469, 581

First La Plata International School, 2008
Compact Object and their Emission, 2009
Ileana Andruchow & Gustavo E. Romero, eds.

Broad-line region size and black hole mass in high-z AGN

Ismael Botti [1], Paulina Lira[1], José Maza[1], Hagai Netzer[2], Shai Kaspi[2] & Dan Maoz[2]

[1] *Departamento de Astronomía, Universidad de Chile, Casilla 36-D, Santiago, Chile.*

[2] *School of Physics and Astronomy and the Wise Observatory, Tel-Aviv University, Tel-Aviv 69978, Israel*

Abstract. In this contribution we briefly review the reverberation mapping technique and its results for low and intermediate luminosity AGNs. Then we present a monitoring campaign of high-luminosity high-redshift quasars which will extend these results by two orders of magnitude, probing the broad-line region size and black hole (BH) mass of luminous AGN at redshift ∼2-3.

1. Introduction

The Broad-Line Region (BLR) is one of the main components of an unobscured AGN (ie, those where we have an unimpaired view torwards the nucleus), and is charactized by very broad emission lines in the UV/optical spectra (Figure 1) with typical widths of several thounsands km/sec due to the proximity to the central BH. One of the features of this region is that the observable UV/optical continuum flux variations are closely related to variations of the emission-lines fluxes. Combining the correlation between continuum and line fluxes variations with the widths of the lines, the mass of the central black hole can be estimated through the reverberation mapping technique (see §2).
In these days, when it is widely accepted that all massive galaxies harbor a black hole in their centers, reverberation has allowed real physical comparison between active and dormants BHs in the local universe, but so far has not probed the high end of the AGN luminosity range.
In the next section we describe briefly the basic theory and results from previous reverberation mapping studies leading to the motivation for a high-luminosity high-redshift quasars monitoring campaign that we are performing since the beggining of 2005. Our main aim is to extend these results by two orders of magnitude, giving the firsts measurement of the largest BHs, and thus extending our knowledge of the physics of AGN and their hosts into an epoch crucial for the understanding of galaxy evolution.

2. Reverberation Mapping Basics

Reverberation mapping is a technique based on the response of the BLR gas to changes in the central continuum source. It is based on three basic assumptions:

1. *The ionizing continuum originates in a single central source.*

This holds because the BLR size is ∼2 orders of magnitude larger than the continuum source.

2. *The light travel time across the BLR is the most important time scale.*

   Which means that the clouds response is practically "instantaneous". Indeed, the recombination time is related with the electron density n_e by the relation $\tau_{rec} \approx 0.1(10^{10}\ \mathrm{cm}^{-3}/n_e)$ hr ≈ 0.1 hr, which is much less than the typical light travel time across the BLR.

3. *There is a simple but not necessary linear relationship between the observed continuum and the ionizing continuum (which gives rise to the emission lines).*

From these points one can construct a simple 1D linear model given by

$$L(t) = \int \Psi(\tau) C(t-\tau) d\tau \tag{1}$$

where $L(t)$ and $C(t)$ are the line and continuum light curves respectively. $\Psi(\tau)$ is the *transfer function* (TF) which holds the information about the geometry and kinematics of the BLR gas. Due to technical limitations, the TF is collapsed to one single parameter: the time lag τ between both continuum and line light curve variations which is obtained through a cross-correlation analysis between them (Peterson 2001). This lag τ is used to directly measure the BLR size from

$$R_{BLR} = c\tau \tag{2}$$

(Peterson et al., 2004, Kaspi et al., 2005). Assuming a gravitationally bound system (proven to be correct for those objects with measurements from several lines, where the observed anticorrelation between the distance r to the BH and the line Doppler widths is consistent with virialized motions of the BLR gas) and measuring the BLR line widths σ, it is possible to infer the mass of the central BH through

$$M_{BH} = \frac{f\ \sigma^2\ R_{BLR}}{G} \tag{3}$$

where f depends on the geometry of the BLR and it is expected to be ∼1.

3. Reverberation Results from low and intermidiate luminosity AGN

Many important results have been found from reverberation mapping studies, such as the stratification of the BLR and black hole masses. Also, an empirical relation between the BLR size and the AGN luminosity has been determined, which shows that *the size of the broad-line region scales with luminosity.* This is not far from the $R_{BLR} \propto L^{0.5}$ relation expected if the BLR in all AGN have similar n_e value and ionization conditions. Kaspi et al. (2005) found that the scaling relation has the form

$$R_{BLR} \simeq 0.4 \left[\frac{\lambda L_\lambda (5100\ \mathring{\mathrm{A}})}{10^{46}\ \mathrm{erg/sec}} \right]^{0.6\pm0.1} \quad \mathrm{pc} \tag{4}$$

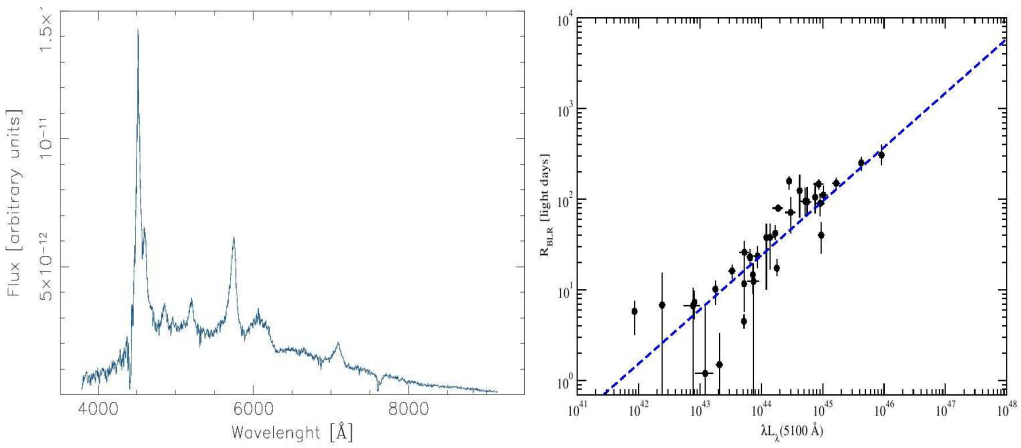

Figure 1. *Left:* Optical spectrum of quasar CT260. Several UV broad-lines (Lyα, SiIV, CIV, CIII) can be seen in the optical window indicating the high redshift of the object ($z = 3$). *Right:* Size-Luminosity relation for AGN with reverberation mapping from Kaspi et al. (2005). All our sources fall above the most luminous object in this diagram.

(as it is shown in Figure 1b). Preliminary results by Bentz et al. (2006) suggest a smaller slope of about 0.52. Using $R_{\rm BLR} - L$ relation is thus possible to estimate the BLR radius using L alone, hence making BH mass estimation accessible for a large number of AGN. Such results cannot be directly applied to high-z, high-L sources that contain the most massive BHs, since measuring their BLR size requires an extrapolation by up to two orders of magnitude in luminosity in eq. (4), which would be subject of a large uncertainty in the measured R_{BLR} (and then in the BH mass). This is the starting point of our quasars monitoring program.

4. Expanding the Luminosity Range: *Quasar Monitoring Campaing*

The few attempts to extend the luminosity range of AGN with reverberation mapping results to high-luminosity AGNs have failed for two reasons: 1. Most high-L sources are very slow variables with very low amplitude ($< 20\%$). 2. The line luminosity amplitude is even smaller than the continuum amplitude because the emission line response is averaged over the very large (~ 1 pc) BLR geometry. Since 2005 we are undertaking a novel strategy that uses optical broad band imaging to trigger spectroscopic follow up on a time scale of about one year. The idea is to identify high-L sources with large enough continuum variations that will enable accurate and meaningful measurement of emission line variations. Only a small fraction of high-L sources show such variations at any given time, hence, a large number of sources must be constantly monitored to identify the onset of such events. Given large enough continuum variations of a certain AGN, the event must be followed spectroscopically. The expected BLR size suggests that the spectroscopy phase should continue for at least four

years.
Our sample consists of 56 quasars which are the brighest from the Calan-Tololo, 2dF and SDSS catalogues spread over all RAs, with $\lambda L_\lambda(5100) \geq 10^{46.5}$ erg/sec, redshifts that range from 2.3 to 3.3 and mean R magnitude about ∼18.2. Until today, black hole mass estimations using reverberation mapping analysis have been mainly based in the variability of the Hβ (λ4861Å) emission line which lies in the optical. In our optical monitoring program we are looking for the CIV (λ1549Å) emission line variability which, because of the the high redshifts of the ojects, falls into the optical window. Reverberation mapping based in the Hβ line can be made for these objects going to the IR.

4.1. Imaging monitoring

Imaging is obtained with the 0.9m Telescope at Cerro Tololo Interamerican Observatory (CTIO) every month for a sub-sample of quasars to monitor their continuum emission in the R band. Monthly datasets allow us to have from 4 to 5 light curves points in average per object in a year, enough to detect the onset of a high variation in their fluxes.
We use differential photometry respect 8 to 13 field stars which allows a photometry independent of the weather conditions, since the object and the field stars are observed simultaneously. These field stars are selected near to the quasar in order to appear in all the observations and have a magnitude cut-off of order of the quasar magnitude. To apply differential photometry we average the field star magnitudes in order to minimize the random variability of each of them, then

$$\langle\ S\ \rangle\,(t) = \frac{1}{N}\sum_{i=1}^{N} m_i(t) \tag{5}$$

is the average field star magnitude. The *rms* of each field star light curve is also checked periodically to look for intrinsically variable objects. This procedure gives us an average magnitude almost constant within the error bars ($\langle S\rangle \sim 3\%$ variable with a typical value of $\sim 2\%$). The quasar Differential Light Curve (DLC) is given by

$$\delta(t_j) = m^{QSO}(t_j) - \langle\ S\ \rangle\,(t_j) = -2.5\log\left(\frac{f_j^{QSO}}{\sqrt[N]{\Pi_i f_{ij}}}\right) \tag{6}$$

where $\delta(t_j)$ is the difference in magnitude between the quasar and the average of field stars at time t_j (in flux it reads as the ratio of the object flux with the geometrical average of the field stars). So, as $\langle S\rangle\,(t)$ is almost flat, the time series of $\delta(t_j)$ gives us the quasar light curve with respect to a constant standard and then variations of δ are exclusively atributted to the quasar. To quantify variability we define the parameter

$$\mathcal{PP}_{\rm var}(\%) = \left(\frac{F_{\rm max}}{F_{\rm min}} - 1\right)\cdot 100\% \tag{7}$$

where $F_{\rm max}$ and $F_{\rm min}$ are the maximum and minimum flux in the DLC, then $\mathcal{PP}_{\rm var}$ is a function of the difference $\delta_{\rm min} - \delta_{\rm max}$ (because $\Delta m \propto \log(F_1/F_2)$).

In this way, the $\mathcal{PP}_{\rm var}$ parameter is just the peak-to-peak variation in flux.
A minimum variability is needed in the continuum to detect a correlated variability in the emission lines (which variation is weaker because is averaged in a larger geometry than the continuum source). Previous reverberation campaigns have concluded that this minimum is ∼15%, then, objects with variability larger than that trigger the spectroscopic follow-up.

4.2. Spectroscopic follow-up

As mentioned before, we are triggering the spectroscopy follow up whenever we detect 15% variability using the 2.5m DuPont Telescope at Las Campanas Obseratory (LCO). We note that at such quasar luminosity, the typical intrinsic continuum variability time scale is 5–10 months. Given the $(1+z)$ factor, in the observed frame the lines are expected to follow the continuum after 1–2 years. During 2005-2006 we obtained spectroscopic observations for the whole sample to establish a zero baseline for future spectroscopy and evaluate the spectroscopic accuracy of our method. In 2007 we have started the actual spectroscopic follow-up of the first quasars. Currently, there are 5 targets which have been followed up since 2007 and there are 3 more quasars reciently (2008) selected for the spectroscopic monitoring.

4.3. Preliminary results

After 3 years of monitoring we can confirm that, in general, quasars are very slow and low amplitude variables (<0.1 mag). However, our strategy has allowed us to identify a subsample of 8 quasars that present a variability greater than 15% (about 0.2 magnitudes, shown in Figure 2) which correspond to the 14.2% of the sample. The variability in some of the objects has been seen to reach up to 20% and spectroscopic follow up has began for them. On the other hand, the varibility of the field stars $\langle\ S\ \rangle$ is lower than 3%. This range is represented in Figure 2 using dot-dashed lines. All points of $\langle\ S\ \rangle$ fall within this region.
Up to date DLC for our targets can be found at the website of the program `http://www.cec.uchile.cl/∼ibotti/reverberation/`.

5. Summary and Perspectives

We reviewed the basis of reverberation mapping technique which is a powerful tool to obtain black hole masses in AGN and the Size-Luminosity ($R_{BLR} - L$) relation from which we can estimate the size of the BLR (and then estimate the BH mass) from a single epoch observation. Currently this relation covers almost 5 magnitudes in luminosity, but it is subjected to large uncertainties when is extrapolated to high luminosity AGN. For a better determination of the slope of this relation we need to span the luminosity range of AGN with reverberation mapping results of $10^{40} - 10^{48}$ erg/sec. To achieve that aim we present a monitoring campaing of a large sample of high-z quasars which will extend these results by two orders of magnitude, measuring the broad-line region size and black hole mass of luminous AGN at high redshifts. Our strategy has been successful identifying a subsample of high variability (≥15%) quasars which are being followed spectroscopically since 2007.
We expect that in the next 3-6 years reverberation mapping analysis will finally

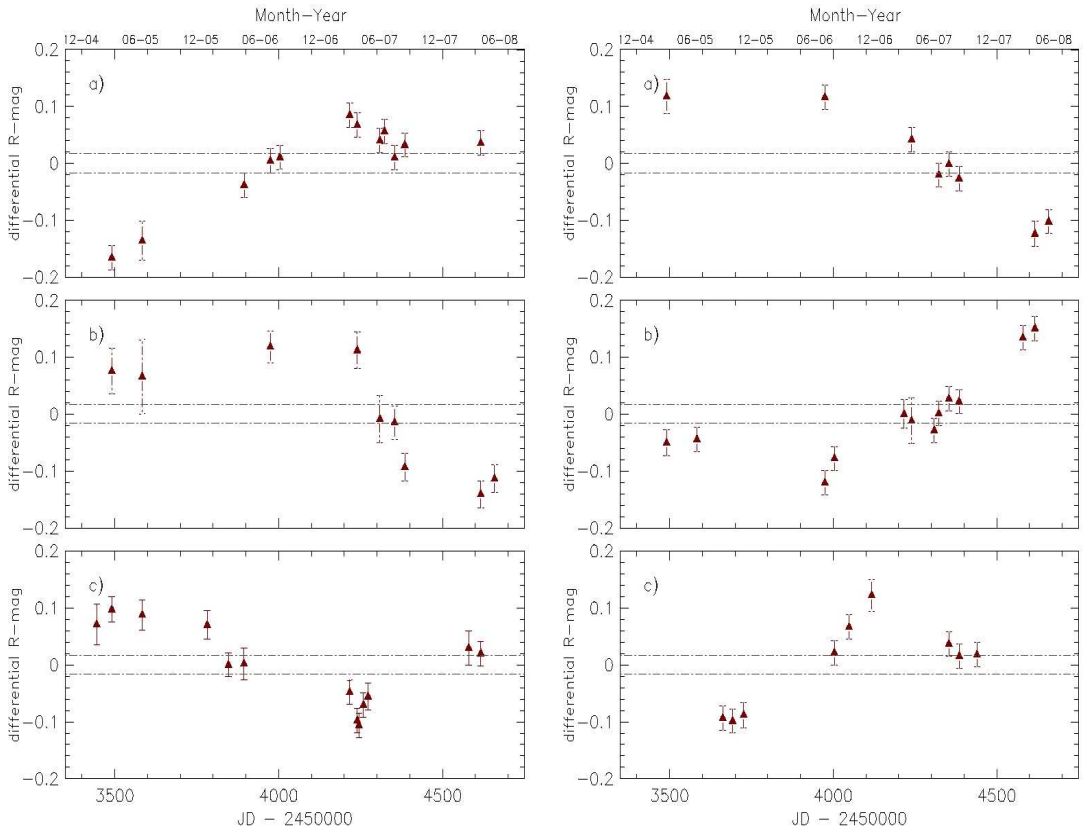

Figure 2. DLCs of some of our most variable objects. *Left:* CTQ953 (*a*), CTQ975 (*b*) and CTQ320 (*c*). Notice that the curves not only show monotonic flux variations, but also peaks, crucial features to apply reverberation mapping analysis. *Right:* DLCs of J224743 (*a*), J214355 (*b*) and CTQ803 (*c*).

yield the highly anticipated measurement of BH masses in some of the most luminous quasars in our Universe.

Acknowledgments. We acknowledge the financial support from the Fondecyt grant no. 1080603 and Proyecto Fondap de Astrofísica 15010003.

References

Bentz, M., et al. 2006, ApJ, 644, 133.

Kaspi, S., et al. 2005, ApJ, 629, 61.

Peterson, B. 2001, in "The Starburst-AGN Connection", ed. by I. Arextaga, D. Kunth, R. Mújica., 3.

Peterson, B., et al. 2004, ApJ, 613, 682.

First La Plata International School, 2008
Compact Object and their Emission, 2009
Ileana Andruchow & Gustavo E. Romero, eds.

Spin paradigm: Is the black hole spin related with galaxy morphology?

Claudia Lagos U.[1], Nelson D. Padilla[1] & Sofía A. Cora[2,3]

[1] *Departamento Astronomía y Astrofísica, Pontificia Universidad Católica de Chile, Av. Vicuña Mackenna 4860, Stgo., Chile*

[2] *Facultad de Ciencias Astronómicas y Geofísicas de la Universidad Nacional de La Plata, and Instituto de Astrofísica de La Plata (CCT La Plata, CONICET, UNLP), Observatorio Astronómico, Paseo del Bosque S/N, 1900 La Plata, Argentina*

[3] *Consejo Nacional de Investigaciones Científicas y Técnicas, Rivadavia 1917, Buenos Aires, Argentina.*

Abstract. We present a study of the revised version of the "spin paradigm" by Sikora & Lasota (2007) which follows the conjecture that the observed AGN-radioloudness bimodality can be explained by a morphology-related bimodality of the distribution of black-hole (BH) spins in the centres of galaxies: central BHs in giant elliptical galaxies may have (on average) much larger spins than BHs in disk galaxies. We use a combination of a cosmological *N*-body simulation of the concordance Λ cold dark matter (ΛCDM) paradigm and a semi-analytic model of galaxy formation (Lagos, Cora & Padilla 2008). This new semi-analitic model (SAG hereafter) takes into account Active Galactic Nuclei (AGN) associated with the presence of super massive BHs (SMBH). The computation of the BH spin is done taking into account several works on the subject (Shakura & Sunyaev; King et al.; Volonteri, Sikora & Lasota). In this model, BH spins are determined exclusively by the accretion history. Here we show how the accretion from a warped disc influences the evolution of BH spins with a detailed study on the contribution from each accretion mechanism. We find that our model follows the "spin paradigm".

1. Introduction

It has been known for many years that the radio loudness of AGN hosted by disc galaxies is on average three orders of magnitude lower than the radio loudness of AGN hosted by giant ellipticals (see Xu et al. 1999 and references therein). Nonetheless, the presence of radio-quiet or radio-loud AGN is not "one-to-one": observational studies indicate that at low luminosities the radio-loudness is a monothonic function of the accretion luminosity (Gallo, Fender & Pooley 2003), whereas at the highest luminosities it may jump by a large factor, following transitions between two accretion states (Fender, Belloni, & Gallo 2004). The observed huge differences of radio-loudness for AGN with similar Eddington ratio, especially at its lowest values, indicate that yet another parameter in addition to the accretion rate must play a role in determining the jet production

efficiency. This is opposite to the "accretion paradigm" which postulates that the existence of jet production is exclusively related to the state of the accretion rate (see for instance Ulvestad & Ho 2001). In addition, the two parallel sequences in the radio-loudness - Eddington ratio plane found by Sikora et al. (2007) can not be explained by the accretion paradigm. In this way, Sikora et al. (2007) proposed a revised version of the "spin paradigm" suggesting that giant elliptical galaxies host, on average, BHs with spins larger than those hosted by spiral galaxies. This morphology-related radio dichotomy breaks down at high accretion rates where the dominant fraction of luminous quasars hosted by elliptical galaxies is radio quiet.

These new observational insights have been studied in theoretical works (e.g. Krolik 2007) that relate rotating BHs with powerfull relativistic jets. Nonetheless, the great advantage of using a semi-analytic model of galaxy formation and evolution is to follow a more realistic BH growth history directly linked with the star formation history (SFH) of host galaxies, also giving the posibility to follow the contribution of all accretion mechanisms to the final BH spin. We follow this approach using the SAG model , which includes gas cooling, star formation, the contribution of energy and metals from different types of supernovae, the growth of BHs and the associated AGN feedback.

2. Computing the black hole spin

Considering the "spin paradigm", Blandford & Znajek (1977) suggested that the efficiency of jet production is determined by the dimensionless BH spin: â $\equiv J_{\rm h}/J_{\rm max} = cJ_{\rm h}/GM_{\rm BH}^2$, where $J_{\rm h}$ is the angular momentum of the BH and $M_{\rm BH}$ its mass. Taking into account the presence of a warped disc characterized by the angular momentum of the disc at the warp radius, $J_{\rm d} = J_{\rm d}(R_w)$, King et al. (2005, hereafter K05) proposed that the amount $J_{\rm d}/J_{\rm h}$ defines the (counter) alignment. The counter-alingment condition is satisfied when $\cos(\phi) < -0.5\, J_{\rm d}/J_{\rm h}$, being ϕ the angle between the disc angular momentum and the BH spin; otherwise, the disc is aligned with the BH spin. We use this criterion to evaluate the BH spin-up or down in the presence of a warped disc.

In a Shakura & Sunyaev (1973, SS73 hereafter) middle-region disc, R_w can be written in terms of the Schwarzschild radius as,

$$\frac{R_{\rm w}}{R_{\rm s}} = 3.6\times10^3 \hat{\rm a} \left(\frac{M_{\rm BH}}{10^8 M_\odot}\right)^{1/8} f_{\rm Edd}^{-1/4} \left(\frac{\nu_2}{\nu_1}\right)^{-5/8} \alpha^{-1/2} \qquad (1)$$

where $f_{\rm Edd} \equiv \eta \times \dot{M}c^2/L_{\rm Edd}$, with $\eta = 0.1$ the standard efficiency of energy production and $L_{\rm Edd}$ the Eddington luminosity, ν_2 is the warp propagation viscosity and ν_1 is the accretion driving viscosity, described in terms of α by SS73 (where ν_2 can be different from ν_1). It can be shown that in a thin disc, $H/R < \alpha \ll 1$ (Papaloizou & Pringle 1983), where H is the disc thickness; therefore, $\nu_2/\nu_1 \approx \alpha^2$. Nonetheless, at high accretion rates (i.e. hot/thick accretion discs) there are indications that $\alpha > 0.1$ (Kumar & Pringle 1985). In this model, both possibilities are explored, that is, $\nu_2/\nu_1 \approx 1$ and $\nu_2/\nu_1 \approx \alpha^2$.

Defining $M_{\rm d}(R_{\rm w}) = \dot{M} t_{\rm acc}(R_{\rm w})$, we have

$$\frac{J_{\rm d}}{J_{\rm h}} = \frac{M_{\rm d}}{\hat{\rm a} M_{\rm BH}} \left(\frac{R_{\rm w}}{R_{\rm s}} \right)^{1/2}, \tag{2}$$

where R_w/R_s is given by Eq. 1, and the rest of the variables are known (i.e. $M_{\rm d}$, $M_{\rm BH}$ and, therefore, $t_{\rm acc}$, are inferred from the SAG model). In this way, we calculate $J_{\rm d}$.

With the information of $J_{\rm d}$, we determine the (counter) alignment to finally (subtract) sum $J_{\rm d}$ to $J_{\rm h}$. This is examined with the following criteria,

→ (C1) if $M_{\rm d} \gg m_{\rm aling} \simeq M_{\rm BH}$ â $\left(\frac{R_{\rm s}}{R_{\rm w}}\right)^{1/2}$, with $m_{\rm aling}$ the mass accreted during the alignment time (Volonteri et al. 2007), alignment is satisfied.
→ (C2) when $M_{\rm BH}$ and $M_{\rm d}$ are massive enough, so that $\mid 0.5 J_{\rm d}/J_{\rm h} \mid > 1$ is always satisfied (Volonteri et al. 2007).
→ If neither C1 nor C2 are satisfied, we calculate a random angle, ϕ, and then review the condition by K05: $\cos(\phi)^{>\rm aling}_{<\rm counter} - 0.5\, J_{\rm d}/J_{\rm h}$.

With this new model we can completely characterize a BH, since we now have information of â as well as the BH mass. We remark that the BH spin in this model is determined exclusively by the BH growth history (without MHD/GR effects).

3. The nature of the BH host galaxies

The main purpose of this work is to find a link between the properties of BHs and those of their host galaxies.

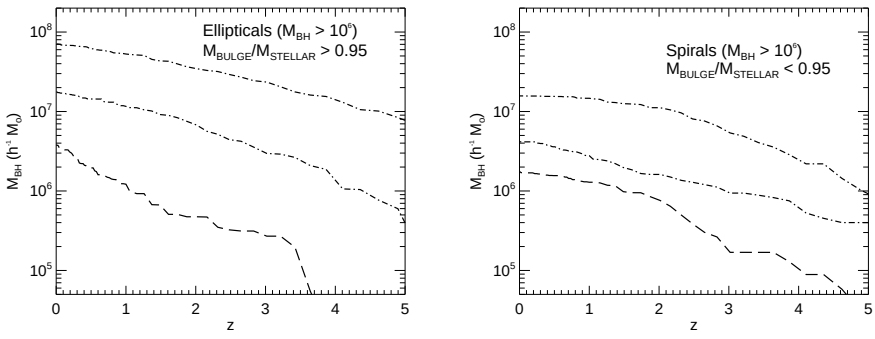

Figure 1. *Left:* Average growth history of BHs hosted by elliptical galaxies ($M_{\rm Bulge}/M_{\rm StellarTotal} > 0.95$) for different mass ranges. *Right:* same as left panel but for BHs hosted by spiral galaxies ($0 < M_{\rm Bulge}/M_{\rm StellarTotal} < 0.95$).

Fig. 1 shows BH growth tracks for BHs hosted by elliptical (left) and spiral galaxies (right). In both cases, we only show BHs with masses $M_{\rm BH} > 10^6\, M_{\odot}$, separated in three mass bins, each containing the same number of BHs. It is evident that BHs hosted by ellipticals have "violent" growth histories compared

with BHs hosted by spirals; besides, the latter stop their growth earlier. This means that ellipticals host more massive BHs. The morphological criteria to distinguish between elliptical and spirals is defined in Lagos, Cora & Padilla (2008, hereafter LCP08).

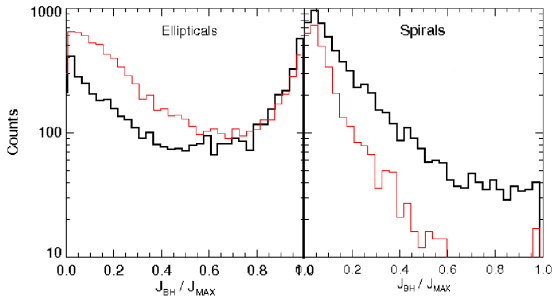

Figure 2. Black hole spin distribution separated by BHs hosted in elliptical (left) and spiral galaxies (right). The red histogram represents the BH spin resulting from setting $\nu_2/\nu_1 \approx \alpha^2$, with $\alpha = 0.01$; the black histogram corresponds to $\nu_2/\nu_1 \approx 1$.

Fig. 2 shows the BH spin distribution for BHs hosted in ellipticals (left) and spirals (right), where the black and red lines represent $\nu_2/\nu_1 \approx 1$ and $\nu_2/\nu_1 \approx \alpha^2$, respectively. Elliptical galaxies host BHs with both rapidly and non-rotating BHs (i.e. the distribution shows two clear peaks), while spirals only host slow and non-rotating BHs (only one peak at $\hat{a} \simeq 0$). We remark that the lower peak in ellipticals corresponds to low-mass galaxies ($M_{\rm Stellar} < 10^{10}\,M_{\odot}$). This implies that, no matter the assumptions on ν_2 and ν_1, massive ellipticals host BHs rotating faster than those hosted by spirals. This is also seen in Fig. 3 where rapidly-rotating BHs reside exclusively in red galaxies, whereas blue galaxies host exclusively slowly rotating BHs.

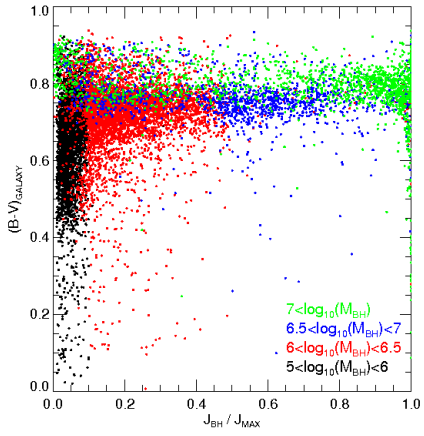

Figure 3. Galaxy colour $B-V$ as a function of central BH spin. Different colours reepresent different BH masses (black points, $10^5 - 10^6\,M_{\odot}$; red points, $10^6 - 10^{6.5}\,M_{\odot}$; blue points, $10^{6.5} - 10^7\,M_{\odot}$; green points, $> 10^7\,M_{\odot}$).

4. The origin of the BH spin

We evaluate the contribution of each BH growth mechanism in the final spin value (see LCP08 for more details). Fig. 4 (left) shows the contribution of each BH growth mechanism to the $z = 0$ BH spin. Main spin-up mechanisms in rapidly rotating BHs are galaxy major mergers and disc instabilities suffered by galaxies with enough massive/slowly rotating discs. Mergers between BHs are negligible in the final spin of rapidly rotating BHs. However, this mechanism is important in low final BH spins. This is in agreement with previous works that indicate that high spins are achieved by accretion of baryonic matter, which is very efficient in spin-up (e.g. Peirani & de Freitas 2008); while mergers between BHs account for the number of BHs at the required low spin (e.g. Moderski, Sikora & Lasota 1998).

It is important to remark that accretion driven by gas cooling processes and minor galaxy mergers randomly help to spin-up or spin-down, giving a net negligible contribution to the final BH spin (Fig. 4, left).

Major mergers and disc instabilities in the SAG model, not only give rapidly rotating BHs, but also produce high accretion rates that finally produce more massive BHs (described in detail by LCP08). Fig 4 (right) shows that massive BHs have higher spins in average when comparing with less massive counterparts. Moreover, the lowest mass bin has a distribution peak at $\hat{a} \simeq 0$. This result is not sensitive to the assumptions on ν_2 and ν_1. This implies that the BH growth histories and the way in which they acquire angular momentum are intimately linked with the host galaxy SFHs and therefore, their morphologies.

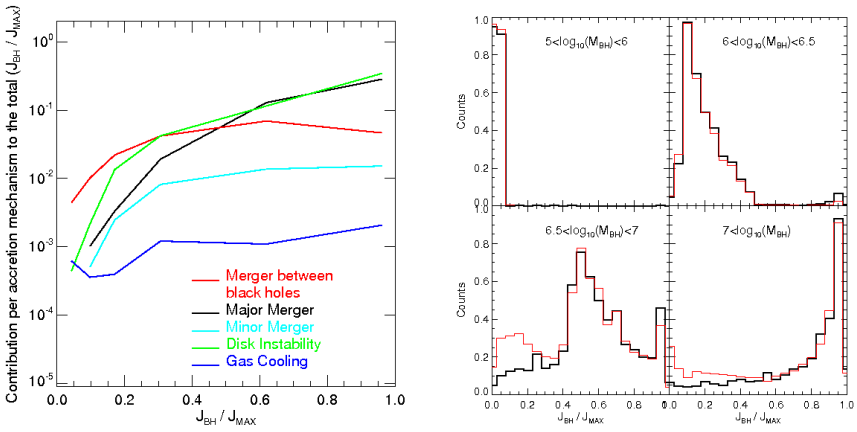

Figure 4. *Left:* Contribution of the five different mechanisms that contribute to the final BH spin (BH growth due to merger between BHs, red line; accretion driven by galaxy major merger, black line; accretion driven by galaxy minor merger, cyan line; when driven by galaxy disc instability, green line; when driven by gas cooling, blue line). The x-axis corresponds to the z=0 BH spin while the y-axis shows the fractional contribution from each mechanism. *Right:* Histograms of black hole spin in four different BH mass bins (indicated in the figure in units of $M_\odot$). The red and black histograms represent the BH spin considering $\nu_2/\nu_1 \approx \alpha^2$ with $\alpha = 0.01$, and $\nu_2/\nu_1 \approx 1$, respectively.

5. Summary and perspectives

In this work we have used the semi-analytic model described by LCP08 to include a simple calculation of the BH spin, thus characterizing a BH completely, with its mass and spin. A main advantage in using a semi-analytic model is to follow for the first time the contribution in the final spin of each BH growth mechanism.

The main results and conclusions of this work reside in the link "galaxy mophology - BH mass - BH spin" summarized as follows: (i) massive BHs are preferentially formed in elliptical galaxies with more violent growth histories compared with BHs hosted by spiral galaxies. (ii) Those massive BHs have high spins compared with low mass BHs that have systematically low spin values. (iii) Massive elliptical galaxies at z=0 host massive and rapidly rotating BHs, whereas dwarf ellipticals host low-mass / slow BHs, consistent with the above mentioned results. This is in concordance with the revised "spin paradigm" proposed by Sikora et al. (2007). (iv) Until now, models could only indicate that accretion of baryonic matter was the main source of BH spin-up (e.g. Peirani & de Freitas 2008). However, with the semi-analytic model we can "split hairs" and predict that the main sources of BH spin-up are accretion driven by galaxy major mergers and disc instabilities.

We remark that this BH spin model is still under improvement. Further work is needed to make predictions about the fraction of radio-loud galaxies as a function of galaxy stellar mass and BH mass using the information of accretion rate and BH spin.

Acknowledgments. We would like to thank A. Reisenegger and J.M. Paredes for usefull comments and dicussions. We also thank "First La Plata International school: Compact objects and their emission" for giving us the possibility to present this work. CL thanks Dirección de posgrado, PUC for travel grants.

References

Blandford, R. D., & Znajek, R. L. 1977, MNRAS, 179, 433
Fender, R. P., Belloni, T. M., & Gallo, E. 2004, MNRAS, 355, 1105
Gallo, E., Fender, R. P., & Pooley, G. G. 2003, MNRAS, 344, 60
King, A. R., et al. 2005, MNRAS, 363, 49
Kroliki, J. H., & Hawley J. F. 2007, AIPC, 924, 801
Kumar, S., & Pringle, J. E. 1985, MNRAS, 213, 435
Moderski, R., Sikora, M., & Lasota, J. P. 1998, MNRAS, 301, 142
Lagos C., Cora, S. A., & Padilla N. D. 2008, MNRAS, 388, 587
Papaloizou, J. C. B., & Pringle, J. E. 1983, MNRAS, 202, 1181
Peirani S., de Freitas Pacheco J. A. 2008, PhRvD, 77, 4023
Shakura, N. I., & Syunyaev, R. A. 1973, A&A, 24, 337
Sikora, M., Stawarz, L. & Lasota J. P. 2007, ApJ, 658, 815
Volonteri, M., Sikora, M., & Lasota J. P. 2007, ApJ, 667, 704
Ulvestad, J. S., & Ho, L. C. 2001, ApJ, 562, 133
Xu, C., Livio, M., & Baum, S. 1999, AJ, 118, 1169

First La Plata International School, 2008
Compact Object and their Emission, 2009
Ileana Andruchow & Gustavo E. Romero, eds.

Evolution of the chemical properties of Milky Way type galaxies in a hierarchical ΛCDM scenario

María Emilia De Rossi[1,2], Patricia B. Tissera[1,2], Gabriella De Lucia[3] and Guinevere Kauffmann[3]

[1] *Consejo Nacional de Investigaciones Científicas, y Técnicas, Rivadavia 1917 (1428), Buenos Aires, Argentina.*

[2] *Instituto de Astronomía y Física del Espacio, Argentina, CC67 Suc28, Buenos Aires (1428), Argentina. derossi@iafe.uba.ar*

[3] *Max-Planck-Institut für Astrophysik, Karl-Schwarzschild-Str. 1, D-85748, Garching, Germany.*

Abstract. We studied the formation and chemical evolution of a sample of Milky Way type galaxies selected from the public database of the Millennium simulation. We found that Milky Way type galaxies in this model may be described by a main progenitor which evolves accreting smaller systems. Only 9 % of the total sample suffers stellar major mergers along their formation paths. We compare this evolution with that of giant elliptical galaxies and dwarf irregular systems extracted from the same catalogue finding strong differences in their assembly histories. The percentage of stellar mass at z=0 coming from accretions ranges from 0 in the case of dwarf irregulars to approximately 50% for giant ellipticals, while for Milky Way type galaxies it is around 15%. These different accretion histories affect the gas consumption and the star formation processes in the main progenitors of the systems leading to very different chemical evolution.

1. Introduction

In the last decade, there has been important progress in the understanding of the chemical enrichment histories of galaxies largely due to the development of more sophisticated surveys which do not only allow for the exploration of vaster regions of the spectra but also provide with insights into the high redshift Universe. Moreover, with the advent of more complex numerical codes and semi-analytical models which include detailed algorithms for the treatment of stellar evolution, it has been possible to start studying the physical processes involved in the chemical evolution of galaxies.

In particular, over the last decade many research projects have tried to link the chemical and dynamical features of galaxies with the aim at finding clues for their evolution. In the local Universe, there is a clear correlation between the stellar mass and metallicity of galaxies in the sense that brighter and more massive systems are more metal-enriched (e.g. Tremonti et al. 2004; Lee et al. 2006). Moreover, this correlation seems to evolve with time in such a way

that, at a given stellar mass, galaxies exhibit lower abundances in the past (e.g. Savaglio et al. 2005; Erb et al. 2006).

Numerical simulations which can describe the non-linear evolution of the matter and its chemical enrichment self-consistently (e.g. Mosconi et al. 2001) and semi-analytical models of galaxy formation (e.g. De Lucia et al. 2004), have proved to be an adequate tool to tackle galaxy evolution from a theoretical point of view. In particular, Tissera et al. (2005) and De Rossi et al. (2007) performed numerical galactic wind-free simulations within a ΛCDM scenario showing that the mass-metallicity relation (MZR) arises naturally as a consequence of the hierarchical building up of the structure.

In this work, we make use of the Millennium Simulation, which is currently the largest simulation of structure formation ever carried out, to study the chemical evolution of galaxies focusing on Milky Way-type systems with the aim at understanding their formation and chemical enrichment histories.

2. The simulation and the galaxy catalogue

This work takes advantage of the public database of the Millennium Simulation. This simulation (Springel et al. 2005) follows $N = 2160^3$ particles of mass $8.6 \times 10^8 M_\odot h^{-1}$ in a comoving periodic box of 500 Mpc h^{-1} on a side, and with a spatial resolution of 5 kpc h^{-1} in the whole box. The cosmological model is consistent with the first-year data from the Wilkinson Microwave Anisotropy Probe (Spergel et al. 2003): $\Omega_{\rm m} = 0.25$, $\Omega_{\rm b} = 0.045$, $h = 0.73$, $\Omega_\Lambda = 0.75$, $n = 1$, and $\sigma_8 = 0.9$.

The galaxy catalogue was generated by using the semi-analytical model described in Croton et al. (2006) and De Lucia & Blaizot (2007). It includes treatment for star formation, gas cooling, metal enrichment, mergers, Supernova and active galactic nuclei (AGN) feedbacks.

3. Sample definitions

For this study we selected the central galaxies of dark matter haloes to define three different galaxy samples:

- A Milky Way (MW) sample built up with galaxies with $200<V_{\rm c}<240$ km s^{-1} and $1.5 < \Delta M < 2.6$, where $V_{\rm c}$ is the circular velocity and ΔM is the difference between the bulge and the total magnitude in the B-band respectively (Simien & de Vaucouleurs 1986).

- A dwarf irregulars sample (DIS) defined selecting all galaxies with $10^9 < M_* < 10^{9.5} M_\odot$. Since there is no evidence of a nucleus in typical dwarf irregulars, we also restricted the DIS to galaxies without a bulge component. Finally, only objects residing in halos with more than 100 particles are included in this sample.

- A giant ellipticals sample (GES) defined selecting all galaxies with $M_* > 10^{11} M_\odot$ and $\Delta M < 0.4$.

4. Results and analysis

For all model galaxies in the three samples, we have reconstructed the full galaxy merger trees by using the public database. We defined a 'main branch' by connecting the galaxy to its most massive progenitor (the main progenitor) at each node of the tree.

By analysing the merger histories of MW-type galaxies, we encountered that at z=0 the percentage of stellar mass accreted by mergers represents around 8-23 per cent of the final stellar mass of these systems. Thus, for all galaxies in the MW sample, more than 80 per cent of the stars were formed in the main branch. Furthermore, only 9 % of the total Milky Way sample experienced a stellar major merger during its evolution. These results indicate that the evolution of the main progenitors of model MW galaxies provides a good representation of the galaxy history itself.

In order to investigate the chemical evolution of MW galaxies, we analyse their distribution on the mass-metallicity plane [1]. At $z = 3$ these systems have a growing mass-metallicity relation (MZR) with metallicities ranging from -1 to 0.7 dex and stellar masses covering the range from 10^8 to $10^{11}\mathrm{M}_{\odot}\mathrm{h}^{-1}$. At $z < 1$, the great majority of the systems reached stellar masses between 10^{10} and $10^{11}\mathrm{M}_{\odot}\mathrm{h}^{-1}$ exhibiting metallicities in the range -0.5-0.5 dex (see De Rossi et al. 2008 for details). Therefore, we see that since $z = 3$ to $z = 1$ the distribution has significantly shrinked showing dispersions lower than 1 dex in both quatities at lower redshifts. At $z = 1$, the mean stellar mass of MW progenitors already represents 75% of the final stellar mass. This fact can only be explained if small mass systems at $z = 3$ evolved more significantly than massive ones. In fact, more massive systems have lower gas fractions and consequently lower specific star formation rates which prevent further enrichment after $z \sim 3$. Moreover, massive progenitors complete most of their accretion histories at $z > 3$. So the largest change in the chemical enrichment level since $z \sim 3$ occurs for the lowest stellar mass systems which exhibit an increase in metallicity of ~ 0.2 dex since $z = 1$. Gas-rich progenitors at $z = 3$, exhibit a more significant chemical evolution at $z > 1$ as a consequence of their higher specific star formation rates and the fact that they accreted a factor of two more stellar mass than gas-poor progenitors in the same redshift range.

Comparing the evolution of Milky Way type galaxies with that of the DIS and the GES, we found that the main differences correspond to their accretion histories. Dwarf irregular galaxies evolve quietly only by minor mergers. They are gas rich systems with a mean gas fraction of ≈ 0.6 at $z = 0$. These galaxies are affected by important galactic winds capable of ejecting large fractions of material outside the systems at $z < 3$. Taking into account the total amount of baryonic mass associated to a dwarf irregular galaxy, we found that the ejected mass represents approximately more than 60% since $z = 3$. Massive elliptical systems accreted approximately 50% of their final stellar mass with major mergers playing an important role in their assembly. By $z = 2$ they have 80 per cent of their final stellar mass formed, reaching $z = 0$ with almost no cold

[1] In this work we defined the metallicity Z as the total mass of all elements heavier than helium contained in the cold gas phase over the total cold gas mass.

gas. Galaxies in the GES are strongly affected by AGN feedback (Croton et al. 2006). Model MW galaxies have a medium behaviour with a dominant SN feedback at high redshift when their progenitors are smaller. According to our results, SN feedback affects strongly the progenitors of MW-type galaxies down to $z \approx 1$.

In the light of these results, we conclude that massive elliptical galaxies seem to have died having formed most of their stellar mass at $z > 2$ and hence they are only able to change their location in the MZR via mergers at lower redshifts. In the case of the MW galaxies, although the gas fractions (~ 0.1) are larger than those of giant elliptical galaxies, they are low for feeding further significant starbursts. On the other hand, dwarf irregular galaxies are yet star-forming galaxies having enough fuel for increasing their stellar content and chemical abundance.

5. Conclusions

We studied the evolution of Milky Way type galaxies within a hierarchical scenario. We found that MW systems in this model may be described by a main progenitor which evolves accreting smaller subtructures. More than 80 % of their final stellar masses were formed within the main branchs of their merger trees. Comparing this results with those obtained for dwarf irregular and giant elliptical galaxies drawn from the same catalogue, we found that the main differences correspond to the accretion histories. These different merger histories affects the way in which gas is consumed in these galaxies modulating the star formation process and AGN and SN feedbacks and leading to very different chemical evolution (De Rossi et al. 2008).

Acknowledgments. MEDR would like to thank the Organizing Committe of this meeting for their financial support. We are grateful to CONICET and LENAC. The Millennium Simulation databases used in this paper and the web application providing online access to them were constructed as part of the activities of the German Astrophysical Virtual Observatory.

References

Croton, D. J., et al. 2006, MNRAS, 365, 11
De Lucia G., Kauffmann G., & White S. D. M. 2004, MNRAS, 349, 1101
De Lucia, G., & Blaizot, J. 2007, MNRAS, 375, 2
De Rossi, M. E., Tissera, P. B., & Scannapieco, C. 2007, MNRAS, 374, 323
De Rossi, M. E., et al. 2008, MNRAS, submitted
Erb, D. K., et al. 2006, ApJ, 644, 813
Lee, H., et al. 2006, ApJ, 647, 970
Lemson, G., & the Virgo Consortium, astro-ph/0608019
Mosconi M. B., et al. 2001, MNRAS, 325, 34
Savaglio, S., et al. 2005, ApJ, 635, 260
Simien, F., & de Vaucouleurs, G. 1986, ApJ, 302, 564
Spergel, D. N., et al. 2003, ApJS, 148, 175
Springel, V., et al. 2005, Nat, 435, 629S

Tissera, P. B., De Rossi, M. E., & Scannapieco, C. 2005, MNRAS, 364L, 38
Tremonti, C. A., et al., 2004, ApJ, 613, 898

First La Plata International School, 2008
Compact Object and their Emission, 2009
Ileana Andruchow & Gustavo E. Romero, eds.

The progenitors of long gamma-ray bursts

Leonardo J. Pellizza[1], Sebastián E. Nuza[1], Patricia Tissera[1], Cecilia Scannapieco[2] & I. Félix Mirabel[3]

[1]*Instituto de Astronomía y Física del Espacio, C.C. 67, Suc. 28, 1428, Buenos Aires, Argentina,*

[2]*Max-Planck-Institut für Astrophysik, Karl-Schwarzschild-Str. 1, D-85748 Garching, Germany*

[3]*European Southern Observatory, Alonso de Córdova 3107, Santiago 19, Chile. pellizza@iafe.uba.ar*

Abstract. We present a scenario for long-duration gamma-ray burst (LGRB) production and energetics, which coupled to cosmological numerical simulations of structure formation in hierarchical models allow us to synthesize LGRB populations and compare their observables to high-energy data from different observatories. Our preliminary results indicate that a simple proportionality between the LGRB rate and the cosmic star formation rate can not explain consistently all observed data currently gathered, although it can separately explain *CGRO* and *Swift* data. At present we are exploring more exotic scenarios, in which the metallicity of the stellar progenitors influences the generation and properties of LGRBs.

1. Introduction

Gamma-ray bursts (GRBs) are brief pulses of gamma-ray radiation observed about once per day at random directions in the sky, followed by fading *afterglows* at longer wavelengths (from X-rays to radio) which can last from days to months or even years. The population of GRBs comprises two subsamples that differ in duration and gamma-ray spectra. Those lasting more than 2 s and showing soft spectra are called LGRBs. The cosmological origin of LGRBs was first suggested by the isotropic distribution of their directions (Kouveliotou et al. 1993), and confirmed by the direct measurement of their redshifts through afterglow absorption lines (van Paradijs et al. 1997). Their measured fluxes at Earth, together with their typical redshifts ($z \sim 1$–2) imply huge luminosities ($L \sim 10^{52}$ erg s^{-1}, if isotropic emission is assumed). Precise positioning of their afterglows allowed their location in star-forming, low-metallicity galaxies (e.g, Le Floch et al. 2003; Savaglio et al. 2008) and their association to simultaneous Type Ib/c supernovae (Galama et al. 1998).

Given these observational results, theoretical models were developed in which LGRBs are produced during the last stages of the evolution of massive stars (e.g., Fryer et al. 1999, Yoon et al. 2006). In these models, the LGRB is a result of accretion onto the black hole formed inside the star by the collapse of its core. However, at present it is not clear if the production of a LGRB depends

on other properties of its stellar progenitor, besides mass. Understanding the relationship between LGRBs and massive stars is important, as it could shed light onto the late evolution of these stars and the mechanisms of stellar black hole formation. Moreover, LGRBs could become an important tool to study the star formation in the early Universe, as they can be easily detected up to high redshifts (e.g., Tagliaferri et al. 2005). If an universal initial stellar mass function is assumed, a direct consequence of the lack of a dependence of LGRB production on quantities other than progenitor mass, is the proportionality between comoving LGRB and star formation rates. Previous works suggest that, using reasonable hypotheses for the LGRB luminosity function and spectral parameters, the flux and redshift distributions observed at Earth do not support this hypothesis (Daigné et al. 2006). Hence, either LGRBs are produced in environments with special stellar initial mass functions, or their production or energetics depend on other parameters of their progenitors.

In this work we explore the predictions made by a scenario for LGRBs based on the hypothesis that these phenomena are produced by stars above some threshold stellar mass. This scenario, coupled to cosmological hydrodynamical simulations of hierarchical structure formation (Scannapieco et al. 2005; 2006), allows us to construct synthetic LGRB populations and predict their observable properties. We investigate the ability of this scenario to fit the corresponding observed properties to assess the plausibility of its main hypothesis.

This paper is organized as follows. Section 2. describes our scenario for LGRBs, while Section 3. shows an discusses our preliminary results.

2. LGRB production scenarios

2.1. LGRB population synthesis

In order to construct synthetic LGRB populations that reproduce the properties of the observed sample of LGRBs, we must put together three ingredients. The first one is a comoving LGRB formation rate $\Psi(z)$ that describes the production of these phenomena as the Universe evolves with redshift z. The choice of $\Psi(z)$ is the main ingredient of our scenario, and will be discussed later in this section. Using $\Psi(z)$ we might construct a population of LGRBs produced in a fixed comoving volume during a fixed comoving time interval. However, the observed sample of LGRBs to which we will compare the predictions of our scenario, was obtained by detectors that monitor a constant solid angle in the sky during a fixed observer frame time interval. Hence, to make a meaningful comparison we need to correct the comoving LGRB rate by the variation with redshift z of the comoving volume element dV/dz and the time dilation factor $(1+z)^{-1}$. It is easily shown that

$$\Psi'(z) = \frac{\Psi(z)}{1+z}\frac{dV}{dz}, \tag{1}$$

is, up to a constant factor, the redshift distribution of a LGRB population with comoving rate $\Psi(z)$, that would observe an ideal detector at the Earth (i.e., one that detects every LGRB independent of its flux). Given this recipe, we devised a Monte Carlo code to generate, for any $\Psi'(z)$, the redshifts of a sample of N

LGRBs. For computing $\Psi'(z)$ from $\Psi(z)$ we assumed the concordance cosmology WMAP 1 ($\Omega_\Lambda = 0.7$, $\Omega_\mathrm{m} = 0.3$, $H_0 = 70$ km s^{-1} Mpc^{-1}).

However, real detectors have peak flux dependent detection efficiencies, hence the observed sample of LGRBs would be different from the population generated by the above method. To take this effect into account, two other ingredients are needed: a LGRB luminosity function $\Phi(L)$, where L stands here for the peak isotropic luminosity in the 1 keV–10 MeV band (hereafter referred simply as luminosity), and a LGRB spectrum. For the first one, and following previous works (e.g., Daigné et al. 2006), we assumed a power-law distribution, $\Phi(L) \propto L^\delta$ for $L_\mathrm{min} \leq L \leq L_\mathrm{max}$. The parameters δ, L_min and L_max are free, and are fitted to obtain the best match to observations. For the LGRB spectrum we assumed a Band function (Band et al. 1993),

$$f(E) \propto \begin{cases} \left(\frac{E}{100\ \mathrm{keV}}\right)^\alpha e^{-E/E_0} & E \leq (\alpha-\beta)E_0, \\ \left(\frac{E}{100\ \mathrm{keV}}\right)^\beta e^{\beta-\alpha} \left(\frac{(\alpha-\beta)E_0}{100\ \mathrm{keV}}\right)^{\alpha-\beta} & E > (\alpha-\beta)E_0, \end{cases} \tag{2}$$

with fixed low and high energy spectral slopes $\alpha = -1$ and $\beta = -2.25$, respectively. The spectral parameter E_0, identical in this case to the spectral peak energy E_p, was assumed to be lognormally distributed, with mean $\langle \log E_0 \rangle$ and standard deviation $\sigma_{\log E_0}$ left free to fit the observations. Monte Carlo codes were devised following this prescription, to assign each LGRB in the synthetic sample a value of L and E_0.

From the three properties of each LGRB in our synthetic sample (z, L and E_0), we can compute their observables. Peak flux P in any desired detector bandpass $[E_1, E_2]$ is obtained from

$$P = \frac{L}{4\pi d_L^2(z)} K(z, E_1, E_2, E_0, \alpha, \beta), \tag{3}$$

where d_L is the luminosity distance at redshift z, and K the correction needed to account for the redshift of the bandpass. For each LGRB in the synthetic population, we compute P for the bandpasses of BATSE detector onboard *Compton Gamma-Ray Observatory* and BAT instrument onboard *Swift* (50–300 keV and 15–150 keV respectively). Once P is computed for a given instrument, its detection efficiency can be taken into account, and the probability of detection of each LGRB can be computed. We use a simple Monte Carlo code to select LGRBs from the synthetic population according to their detection probability, hence construct two samples of synthetic LGRBs containing events detectable by *CGRO* and *Swift*. We used the recipes of Stern et al. (2001) and Daigné et al. (2006), for the detection efficiencies of *CGRO* and *Swift*, respectively. We also computed for each LGRB the observer-frame spectral peak energy $E_\mathrm{p,obs}$ from E_0, z and α. With these samples we construct the four observables of our synthetic LGRB population, namely the P and $E_\mathrm{p,obs}$ distributions for the LGRBs detectable by each satellite. We put our scenario to test by comparing these observables with the corresponding ones of the observed LGRB population.

2.2. LGRB generation scenario

In this paper we explore a main scenario based on the hypothesis that LGRBs are produced by stars above some threshold mass. Then, the main assumption of our LGRB scenario is that

$$\Psi(z) = k_0 \dot{\rho}_*(z), \tag{4}$$

where $\dot{\rho}_*(z)$ is the cosmic star formation rate at redshift z, and k_0 a constant whose value is unimportant because we are only interested in comparing distributions, not in the total number of LGRBs produced. For this scenario, a Markov-Chain Monte Carlo scheme was used to explore its parameter space and find the best fit to observations. For each set of parameter values, a population of 10^7 synthetic LGRBs was computed in order to minimize the statistial fluctuations in the final observables down to a level at which they have no influence on the fit. More than 10^4 steps in the Markov Chain were used to ensure the convergence of the fit.

The cosmic star formation rate $\dot{\rho}_*(z)$ was taken from cosmological hydrodynamical simulations of hierarchical structure formation (Scannapieco et al. 2005; 2006). These simulations take into account the chemical and energy feedback produced by Type Ia and Type II Supernovae in the interstellar medium (ISM) as the structure is assembled in consistency with the adopted cosmology. The simulated volume corresponds to a periodic box of 10 Mpc h^{-1} comoving size resolved with 2×160^3 total particles with an initial mass of 2.7×10^6 $\mathrm{M}_\odot h^{-1}$ and 1.4×10^7 $\mathrm{M}_\odot h^{-1}$ for the gas and dark matter particles, respectively. Gas particles are transformed into star particles in star formation episodes. We assume a Salpeter Initial Mass Function and apply it to each single stellar population represented by a star particle. Hence, the number of stars of a given stellar mass can be easily calculated. The choice of these simulations was dictated by the need of an accurate and self-consistent description of the cosmic star formation rate as a function of redshift.

3. Preliminary results and discussion

Table 1 and Figure 1 show the preliminary results of our simulations. Table 1 presents the best-fit values of the free parameters for our scenarios. Figure 1 shows the observables of synthetic LGRB population (solid lines), compared to actual LGRB data (circles). Top panels show the LGRB peak flux distributions, while bottom ones show the $E_{\mathrm{p,obs}}$ distribution. In both cases, left panels correspond to the distributions observable by *CGRO*, while right ones correspond to those observable by *Swift*. As it can be seen, none of these scenarios is capable of explaining the full set of data. The reduced goodness-of-fit (χ^2/dof) for the best-fit parameters is about 10 in both cases. Successful attempts were made to fit *CGRO* and *Swift* data separately (dotted and dashed lines in Fig. 1, respectively), but no set of parameters could attain a good fit for both at the same time.

Our preliminary results indicate that this simple scenario can not explain the current data, in agreement with previous works (e.g., Daigné et al. 2006). At the same time, our results give some insight into the nature of the problem. As,

δ	$\log L_{\rm min}$ erg s^{-1}	$\log L_{\rm max}$ erg s^{-1}	$\langle \log E_0 \rangle$ keV	$\sigma_{\log E_0}$ keV
-1.44	50.15	53.02	2.92	0.32

Table 1. Best-fit values for the free parameters of our LGRB production scenario.

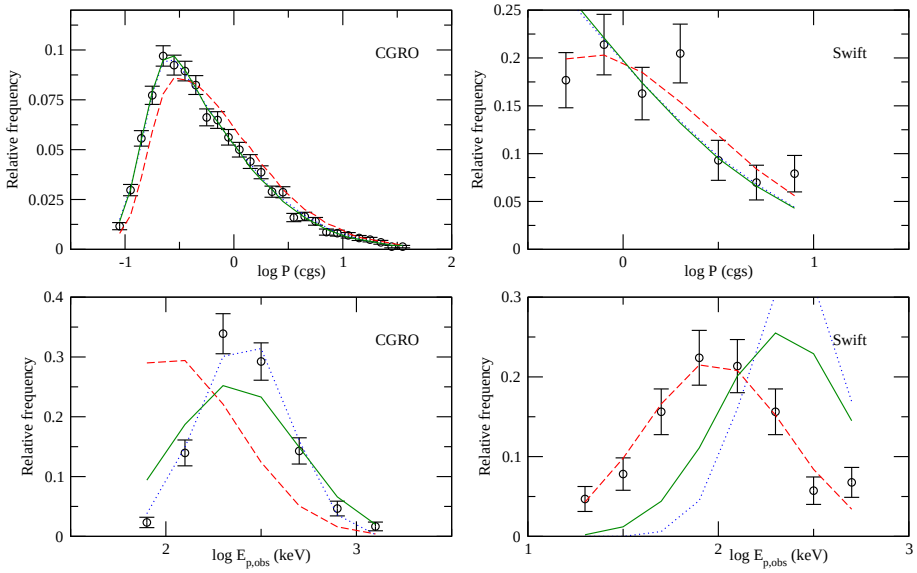

Figure 1. Best-fit peak flux P (top) and spectral parameter $E_{p,\rm obs}$ (bottom) distributions observable by *CGRO*–BATSE (left) and *Swift*–BAT (right), as predicted by our scenario (solid lines), compared to actual data (circles). Dotted and dashed lines correspond to the separate fits to *CGRO* and *Swift* datasets, respectively.

given a fixed E_0 distribution, the observed $E_{\rm p,obs}$ distribution is a proxy for the redshift distribution, Fig. 1 suggests that both detectors are, under this simple scenario, observing the same part of the synthetic LGRB redshift distribution. However, the observed data clearly show that this is not actually the case, as *CGRO* and *Swift* data can be fitted separately with different sets of parameters. Hence, our results suggest that a LGRB production scenario that decouples *CGRO* and *Swift* redshift distributions is needed to solve the problem. In order to achieve this decoupling, more sophisticated scenarios in which the LGRB rate or energetics depend on the metallicity of their progenitor (Nuza et al., in preparation) could be important to explore, taking into account observational results that suggest a link between the energy of the GRB to its metallicity content. Completely different scenarios, in which the production of LGRBs depends on its environment via a non-universal initial mass function, or LGRBs are not formed from single stellar progenitors but rather from binaries are also worth being explored. At present, we are working on these alternative scenarios.

Acknowledgments. We would like to thank C. Dermer and G.E. Romero for useful talks during the School.

References

Band, D., et al. 1993, ApJ, 413, 281
Daigne, F., Rossi, E. M., & Mochkovitch, R. 2006, MNRAS, 372, 1034
Fryer, C. L., Woosley, S. E., & Hartmann, D. H. 1999, ApJ, 526, 152
Galama, T.J., et al. 1998, Nature, 395, 670
Kouveliotou, C., et al. 1993, ApJ, 413, L101.
Le Floc'h, E., et al., 2003, A&A, 400, 499
Savaglio, S., Glazebrook, K., & Le Borgne, D. 2008, arXiv0803.2718
Scannapieco C., et al. 2005, MNRAS, 364, 552
Scannapieco C., et al. 2006, MNRAS, 371, 1125
Stern, B. E., et al. 2001, ApJ, 563, 80
Tagliaferri, G., et al. 2005, A&A, 443, L1
van Paradijs, J., Groot, P. J., & Galama, T. 1997, Nature, 386, 686
Yoon S.C., Langer N., & Norman C. 2006, A&A, 460, 199

First La Plata International School, 2008
Compact Object and their Emission, 2009
Ileana Andruchow & Gustavo E. Romero, eds.

First buried muon counter prototype for the Auger Observatory

I. P. Sidelnik[1,2], B. Wundheiler[1], E. Colombo[1], A. Etchegoyen[1,2], A. Ferrero[1], M. Platino[1] & O. Wainberg [1,3]

[1] *Laboratorio Tandar, Centro Atómico Constituyentes, Comisión Nacional de Energía Atómica, Avenida Gral. Paz 1499, (1650) Buenos Aires, Argentina*

[2] *CONICET, Argentina*

[3] *UTN-FRBA, Argentina*

Abstract. AMIGA (Auger Muons and Infill for the Ground Array) constitutes an enhancement for the Pierre Auger Observatory. It consists of a denser array of surface detectors and muon counters whose objective is both to extend the detection range down to 10^{17} eV and to help towards mass composition determination. The latter is to be achieved with muon counters since the shower muon content is one of the best parameter for particle type identification. In this work, we present the study of a muon counter prototype. The prototype was buried 3 m deep in an effort to avoid signal contamination from the shower electromagnetic component. We study the performance of the detector before and after burying it with its associated electronic components. The detector validation is performed from signal analysis of charged particles traversing the counter.

1. Introduction

The cosmic ray energy spectrum presents four main features (Nagano & Watson, 2000) which give rise to abrupt spectral index changes: the knee, the second knee, the ankle and the GZK cutoff. The knee is at $\sim 4 \times 10^{15}$ eV, the second knee at $\sim 4 \times 10^{17}$ eV, the ankle at $\sim 3 \times 10^{18}$, and finally the GZK cutoff, i.e. the suppression of the cosmic ray flux at energies above $\sim 4 \times 10^{19}$ eV. The Auger collaboration has recently shown experimental evidence of the ankle (Tokonatsu, 2007), the GZK-cutoff (Abraham, 2008a), and of the anisotropy in the arrival direction of the cosmic rays with energies above $\sim 6 \times 10^{19}$ eV (Abraham 2008b) wich is a further confirmation of the flux cutoff.

The ankle region may actually be considered as a dip raging from the second knee up to $\sim 10^{19}$ eV and in an attempt to fully study these two spectrum traits Auger is building two detector enhancements: AMIGA (Etchegoyen, 2007) and HEAT (High Elevation Auger Telescopes) (Klages, 2007). The physical interpretations of the second knee and ankle are not yet clear but still they are closely linked. They are assumed to be related to the transition from galactic to extra-galactic cosmic ray sources and from dominant heavy to dominant light primary compositions (Allard et al. 2005, Berezinsky et al. 2004, Wibig and Wolfendale 2005).

The Pierre Auger Observatory (Abraham et al., 2004) is built to detect cosmic rays from the second knee up to the highest energy cosmic rays known with two distinct design features, a large size and a hybrid detection system in an effort to detect a large number of events per year with minimum systematic uncertainties. It will have a southern and a northern component. The former is located in the west of Argentina, in the Province of Mendoza where it spans an area of 3000 km^2 covered with a surface detector (SD) system of 1600 water Cherenkov detectors (Allekotte et al., 2008) deployed on a 1500 m triangular grid plus four buildings on the array periphery lodging six fluorescence detector (FD) telescopes each one with a $30^\circ \times 30^\circ$ elevation and azimuth field of view. As above mentioned it now encompasses two enhancements and in this work we are going to concentrate on the AMIGA muon counters.

2. AMIGA muon counters

The Observatory was original designed to be fully efficient at $\sim 3{\times}10^{18}$ eV for the surface array and at $\sim 10^{18}$ eV for the hybrid mode. The enhancements (see Fig. 1) will extend these efficiencies down to 10^{17} eV and $\sim 2 \times 10^{17}$ eV, respectively. Decreasing energies imply both a flux increment and a smaller shower lateral distribution spread and therefore AMIGA will encompass a smaller area with a denser array (Etchegoyen 2007).

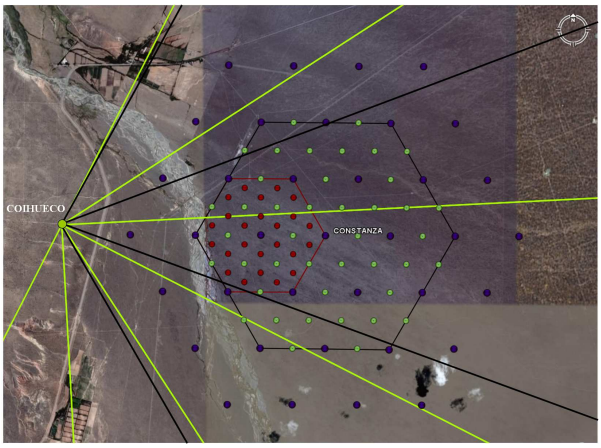

Figure 1. Auger enhancements layout. Light and dark lines limit the $0^\circ - 30^\circ \times 0^\circ - 30^\circ$ and $30^\circ - 60^\circ \times 0^\circ - 30^\circ$ elevation and azimuth field of view for the original 6 fluorescence telescopes and the HEAT 3 telescopes on Cerro Coihueco, respectively. The two hexagons limit the AMIGA areas of 5.9 and 23.5 km^2 with 433 and 750 m triangular grid detector spacings, respectively. Each dot within these hexagons represents a pair of a water Cherenkov tank and a muon counter. The center dot is the Constanza pair placed ∼6.0 km away from Cerro Coihueco.

The muon number and X_{max} (the position where the airshower attains its maximum development) are the best two indicators of the chemical composition of cosmic rays. Auger measures X_{max} using its fluorescence telescopes and it

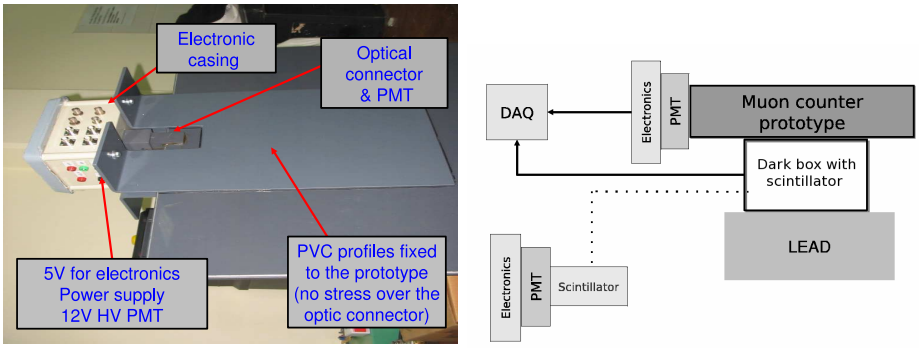

Figure 2. Muon counter main features and schematics of the experimental setup. *lhs*: Detail of the electronic underground enclosure. *rhs*: Coincidence box used as an external trigger, dash line points to experimental setup inside the box.

will measure the shower muon content (Supanitsky et al., 2008) with plastic scintillators. To achieve this objective, along with each SD of the graded denser array, a 30 m^2 area muon counter will be buried 2.25 $\pm$ 0.05 m underground in order to avoid electromagnetic contamination. The scintillator modules are not supposed to reconstruct the shower parameters (which will be performed by the FD and SD systems) but just to count muons.

The scintillator strips were developed following the MINOS design (MINOS, 1998) at the "Scintillator Fabrication Facility" at the Fermi National Accelerator Laboratory (FNAL). Each counter will have four modules with 4.1 cm wide $\times$ 1.0 cm high strips, two of them 400 cm long and the other two 200 cm long, in order to check pileup close to the shower core. They are made of extruded polystyrene doped with fluors and co-extruded with a TiO_2 reflecting coating with a groove in where a wave length shifter (WLS) fiber is glued and covered with a reflective foil (Etchegoyen 2007). Each module will consist of 64 strips with the fibers ending in an optical connector matched to a 64 multianode photo multiplier tube (PMT) from the Hamamatsu ultra bialkali H8804-200MOD series (2 mm $\times$ 2 mm pixel size). The module enclosure will be made of PVC.

Before proceeding to install muon counters at the field in the Observatory site, it is convenient to bury and deploy a prototype in a field close to a laboratory environment within which the process can be conveniently validated under emulated AMIGA working conditions. The main objective of this work is to report on such a buried muon counter prototype.

3. Main objective & Procedure

A prototype was developed for AMIGA in collaboration with Argonne National Laboratory (ANL) and FNAL. This module is 135 cm long, 75 cm wide (16 strips), and 1 cm thick with 1.2 mm WLS KURARAY green optical fiber glued

Figure 3. Setup A & B: laboratory conditions and buried detector. *lhs:* suspended lead column on the module prototype in the laboratory, *rhs:* service pipe to gain access to the electronics.

in each strip groove. A 16 multianode Hamamatsu H8711-06 PMT was used with an 8 channel associated electronic board in order to acquire the PMT analogic signals.

To protect the electronic board and connections from humidity and corrosion, an ad-hoc enclosure box capable to endure buried conditions was designed and assembled. Figure 2 (*lhs*) shows details of the electronic enclosure with output (top wall) and power supply (side wall) connectors. The box is connected to the PMT which in turns links to the module via the optical connector to which the WLS fibers are glued. Data acquisition was performed with a Tektronix TDS 3032 digital oscilloscope (300 MHz of band width and 2.5 GS/s of sample rate).

The experiment was set to measure quasi-vertical impinging atmospheric muons and to ensure this, a time coincidence was requested. This coincidence was attained by adding to the experimental setup a short scintillator strip connected to a PMT inside a dark box. Its signals were channelled to the oscilloscope external trigger (see Figure 2 (*rhs*)).

With the purpose of understanding the effect of the soil over the muon counter (the baseline design calls to bury the counters at 540 g/cm^2, i.e. $\sim$ 3 m for a standard soil density of 1.8 g/cm^3 or $\sim$ 2.3 m for the Observatory high density soil of 2.38 g/cm^3) we carried out two different experiments, with the counter set in the laboratory (setup A) and afterwards with the same counter buried in soil (setup B).

In setup A we set off by subjecting the prototype under stress for a period of a month by placing it underneath a 45 cm lead column in order to simulate the 540 g/cm^2 soil pressure. Experiments were performed after this test in an effort to discard any module mechanical damage prior to burring it, stress damages over longer period of time were to be tested after burying the module. The lead stress was applied at the module center over an area four strip wide $\times$ 30 cm long. The coincidence box was designed to cover such an area as to make certain that the muon signals originated there. Also, and in order to avoid ground electromagnetic contamination, a lead shielding under the detector was used.

A test comparison was performed under the same shielding (i.e. amount of lead) causing and no causing stress, i.e. directly resting on the module or suspended just above it (see Figure 3 (*lhs*)). Results will be discussed in Sec. 4.

In setup B we repeated these conditions in a 3 m well excavated near the Tandar Laboratory, first making the measurements without dirt and then covering the detector with it. For a month the counter was kept buried during this stage of the experiment.

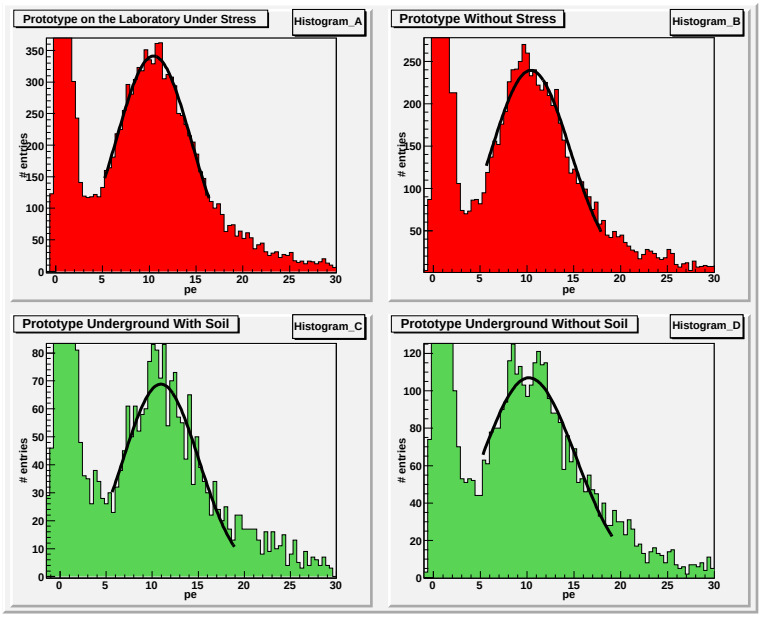

Figure 4. Charge Histograms as a result of the measurements made with setup A & B: comparison between results show similar features in all cases. *Top:* laboratory setup tested with and without stress. *Bottom:* buried prototype with and without dirt.

As a result of these different setups we had four different experimental conditions: lead suspended above and resting on the prototype, and underground with and without soil. On the *lhs* of Figure 3 we show the experimental setup mounted in the laboratory with a column of lead and the coincidence box, while on the *rhs* we show a detail of the service pipe (3 m tall 1 m diameter) installed to gain access to the buried electronics.

4. Results

Total charge histograms were performed integrating the pulses generated by each traversing muon. In order to study and compare different scenarios the histograms were normalized to the single photoelectron (spe) charge so the comparison can be made in terms of the spe produced for each of the four setups.

Figure 4 shows the normalized charge histograms for the prototype for each experiment layout, using one representative pixel of the PMT used. Fitting the zone associated with muon signals, we found a mean value of 10.55 $\pm$ 2.19

pe for the four setups, in agreement with our previous results (Krieger, 2008). The analyses show that the response of the buried prototype is the same as in laboratory conditions. So we conclude that the muon signal provided by our counter appears not been affected by neither applying stress or burying it in a 3 m well covered with soil, supporting the baseline AMIGA muon counters as a tool to establish the muon content of an extended air shower.

5. Conclusions

We made the first positive experiment in working conditions testing a muon counter and its electronic and showing that burying the detector 3 m deep will not affect the measurements for the AMIGA muon counters.

We also shown that measured muon signals main features do not change in both laboratory conditions (with and without stress) and buried underground in much rougher conditions.

A new design and construction of an underground electronic enclosure and its assembly on to the muon counter case was developed as well as the design and commissioning of a service pipe allowing the operation of the buried electronics; it would be used on the AMIGA Unitary Cell.

References

Abraham, J. et al. (The Auger Collaboration) 2004, Nucl. Inst. & Meth., A523, 50

Abraham, J. et al. (The Auger Collaboration) 2008a, PhRvL., 101 (061101),1

Abraham, J. et al. (The Auger Collaboration) 2008b, Astropart. Phys.,29 188

Allekotte, I., et al. (for The Auger Collaboration) 2008, Nucl. Inst. & Meth., A586 409

Allard, D., et al. 2007, Astropart. Phys., 27, 61

Berezinsky, V., et al. 2004, Astropart. Phys., 21, 617

Etchegoyen, A. (for The Pierre Auger Collaboration) 2007, Proceedings of 30th ICRC (Mérida-México), 1307

Klages, H. (for The Pierre Auger Collaboration) 2007, Proceedings of 30th ICRC (Mérida-México), 65

Krieger, A. 2008 (personal communication)

MINOS Collaboration, October 1998 "The MINOS Detectors Technical Design Report", Version 1.0.

Nagano, M., & Watson, A. 2000, Rev. Mod. Phys.,72, 692

Supanitsky, A. D., et al. 2008, Astropart. Phys., accepted for publication (arXiv:0804.1068)

Tokonatsu, Y. (for the Pierre Auger Collaboration) 2007, Proceedings of 30th ICRC (Mérida-México), 318.

Wibig, T., & Wolfendale, A. 2005, J. Phys. **G**, 31, 255

First La Plata International School, 2008
Compact Object and their Emission, 2009
Ileana Andruchow & Gustavo E. Romero, eds.

Constraint preserving boundary conditions for the Ideal Newtonian MHD equations

Mariana Cécere[1], Luis Lehner[2] & Oscar Reula[1]

[1] *FaMAF, Universidad Nacional de Córdoba, Córdoba, 5000 (Argentina)*

[2] *Department of Physics and Astronomy, Louisiana State University, Baton Rouge, LA 70803-4001 (USA). cm4@famaf.unc.edu.ar*

Abstract. We study and develop constraint preserving boundary conditions for the Newtonian magnetohydrodynamic equations and analyze the behavior of the numerical solution upon considering different possible options. We concentrate on both the standard ideal MHD system and the one augmented by a "pseudo potential" to control the divergence free constraint. We show how the boundary conditions developed significantly reduce the violations generated at the boundaries at the numerical level and how lessen their influence in the interior of the computational domain by making use of the available freedom in the equations.

1. Introduction

Magnetic fields play an important role in the behavior of plasmas and are thought mediate important effects like dynamos in the core of planets and the formation of jets in active galactic nuclei and gamma ray bursts; induce a variety of magnetic instabilities; realize solar flares, etc (Goedbloed & Poedts, 2004; Davidson, 2001). The non-linear nature of MHD equations, implies that solutions for complex systems must be obtained by numerical means and a suitable numerical implementation must be constructed for this purpose. Such implementation must be able to evolve the solution to the future of some initial configuration and guarantee its quality. A subsidiary quantity, the "monopole magnetic" $\nabla_i B^i$, can be monitored in part to estimate this. This quantity must be zero at the analytical level for a consistent solution; but this is only true in an unbounded domain, and it is not when boundaries are present. There are formulations in which the constraint propagates along the boundary and so, no extra boundary condition is needed but that formulation, is not symmetric hyperbolic and presents some problems of convergence. The symmetric hyperbolic formulations have the constraint propagating, in and out of the boundary and so appropriate boundary conditions must be given in order to ensure constraint would remain null. To controls the constraint at truncation-error level, we use *divergence cleaning*, which controls the constraint not on the algorithm to be employed but rather on the system of equations to be solved itself. This is achieved by considering an additional variable suitably coupled to the system through another equation so that, through the evolution, the constraint behavior is kept under control. In the present work we concentrate on formulating constraint preserving boundary conditions for the Newtonian ideal MHD equations. Such

a task is intimately related to the hyperbolic properties of the equations and so we re-analyze the system of equations and discuss alternatives for controlling the constraints through the divergence cleaning technique.

We organize our presentation along the following lines. In section 2 we analyze the system of equations and the formulation of boundary conditions to apply in the complete MHD system. Section 3 presents a series of tests that highlight the benefits gained by our construction. We conclude in section 4 with some final comments.

2. The Newtonian equations & constraint hyperbolic cleaning

2.1. Preliminaries

The equations describing the ideal Newtonian MHD equations in terms of the variables (ρ, p, v^i, B^i) are [1,2]:

$$\begin{aligned}
\partial_t \rho &= -\nabla_i(\rho v^i)\,, &(1)\\
\partial_t p &= -v^i\nabla_i p - \gamma p \nabla_j v^j\,, &(2)\\
\rho\partial_t v^i &= -\rho v^j\nabla_j v^i - \nabla^i p - \nabla_j(e^{ij}\frac{1}{2}B_k B^k - B^j B^i)\,, &(3)\\
\partial_t B^i &= -\nabla_j(v^j B^i - v^i B^j)\,. &(4)
\end{aligned}$$

In this form, this system of equations is *weakly hyperbolic* since there is no complete set of eigenvectors. This indicates instabilities are likely to arise unless some modes are carefully controlled. The constraint transport technique attempts to do so at the algorithmic level by enforcing $\nabla_i B^i = 0$ at the discrete level. We here choose an alternative approach where the situation is remedied at the analytical level through the addition of an extra field coupled to the system in a suitable way (Kim et al., 1999; Debner et al., 2002). The proposed system is:

$$\begin{aligned}
\partial_t B^i &= -\nabla_j(v^j B^i - v^i B^j) - c_l\nabla_i\phi\,,\\
\partial_t \phi &= -c_l\nabla_k B^k - s\phi\,. &(5)
\end{aligned}$$

Notice that for $\phi = 0$ the modified system is equivalent to the original one, and ϕ has as a source proportional to the constraint. Thus if boundary and initial data are such as to guarantee that $\nabla_k B^k = 0$, and trivial data is given for ϕ the solution to the modified system is also a solution of the original equation. The advantage of this modification is that now the system is *strongly hyperbolic*, so it has a well posed initial problem and is stable irrespective of whether or not $D \equiv \nabla_k B^k$ vanishes. Furthermore, the induced evolution equation for D is no longer trivial, and it implies that the field D propagates with speed c_l. Consequently one can make the constraint violations to propagate away from the integration region, and, if correct boundary conditions are given, leave the computational region entirely. Additionally, the last term in the equation for ϕ in (5) induces a decay of the constraint for $s > 0$ as it travels along the integration region further helping to keep it under control.

2.2. Boundary conditions

Our goal is to define conditions which can yield a well posed problem and, if possible, guarantee no violations are introduced into the computational domain. To this end we must determine which are the incoming and outgoing modes off the boundary surface as this information is key to understand what data is freely specifiable. For this we seek a solution of the form $U = U^j e^{i(\sigma t + n_j x^j)}$, where U is a vector to be determined along with the frequency σ, and n_j is the outgoing normal to the boundary under consideration.

We now consider a boundary with outgoing unit normal n^j and obtain the characteristic decomposition at this boundary. For notational purposes we will employ an overbar to denote the perturbation on a given variable, for instance $\bar{\rho}$ will denote the perturbation of ρ which will be considered as a fixed background quantity. The characteristic decomposition is then determined from the system, $\sigma U = AU$, where A is

$$A = \begin{pmatrix} -v_n & -\rho & 0 & 0 & 0 & 0 & 0 \\ 0 & -v_n & 0 & B_n/\rho & -\tilde{B}_i/\rho & -1/\rho & 0 \\ 0 & 0 & -v_n & \tilde{B}_i/\rho & B_n/\rho & 0 & 0 \\ 0 & 0 & 0 & 0 & 0 & 0 & 1 \\ 0 & -\tilde{B}_i & B_n & \tilde{v_i} & -v_n & 0 & 0 \\ 0 & -{c_s}^2\rho & 0 & -(\gamma-1)B_j v^j & 0 & -v_n & -(\gamma-1)B_n \\ 0 & 0 & 0 & {c_l}^2 & 0 & 0 & 0 \end{pmatrix} \tag{6}$$

The solution to this system is cumbersome and requires dealing with different cases. Here: $U = (\bar{\rho},\ \bar{v}_n,\ \tilde{\bar{v}}_i,\ \bar{B}_n,\ \tilde{\bar{B}}_i,\ \bar{p},\ \bar{\phi})^T$ indicating perturbations off $(\rho, v^i n_i, \tilde{v}^i, B^i n_i, \tilde{B}^i, p, \phi)^T$ respectively with $\tilde{v}^i, \tilde{B}^i$ indicating the components of v^i and B^i orthogonal to the boundary.

This problem of eigenvalues/eigenvectors can be solved to determine the incoming ($\sigma > 0$), tangential ($\sigma = 0$) and outgoing ($\sigma < 0$) modes. A necessary condition for a well posed problem for hyperbolic systems indicates that data must be given only to the incoming modes, since the others are determined from the inside of the integration region (Reula, 2004). Recall that the incoming modes can be defined even as linear functions of the outgoing ones so long as the coefficients are small enough.

Now, we can determine the possible boundary conditions. A simple one is to set all incoming modes to zero (a no-incoming condition) but this, generically, will not be consistent with the constraint. To this end, one must analyze the induced evolution for the constraint and obtain from it a recipe for what to provide to the incoming modes. In the general, one can formulate constraint preserving boundary conditions by enforcing

$$\pounds(U) \equiv U L_+ \, \Theta_{L+} \dot{U} = 0, \tag{7}$$

where $\pounds(U)$ denotes the (maximally dissipative) constraint preserving boundary condition. Here, UL is the eigenvector when B and ϕ are non-zero, the subindex $+$ denotes that the eigenvector corresponds to incoming mode, and Θ is the cobasis associated with the system of equations that takes D and $\partial_i \phi$ as variables.

2.3. Boundary conditions adopted

For boundary conditions we adopt one of the following three possible cases:

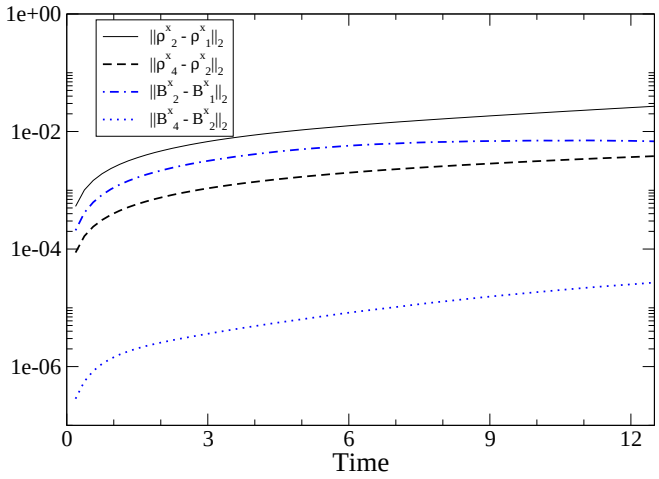

Figure 1. Behavior of $||F(\Delta_l) - F(\Delta_{l+1})||_2$ ($F = \rho$ or B^x).

1) Freezing boundary conditions (FR): Defined by $\dot{U}_i = 0$, for $i = 1..7$.

2) Outflow boundary condition -incoming modes set to zero- (NI): Defined as $\Xi^+ \dot{U} = 0$, with $\Xi^+ = \sum_j U^+_j \theta^+_j$, for j such that $\lambda_j > 0$. θ is the cobasis, which variables are B_n and ϕ.

3) Constraint preserving boundary condition (CP): Defined as $\pounds(U) = 0$, as defined by eqn. (7).

3. Numerical tests

3.1. Testing the implementation

In the first test we confirm the overall convergent behavior of the numerical solution when considering sufficiently smooth initial data. We evolve the C^2 version of the Rotor initial data (with no constraint violation or background fluid flow) for three different resolutions $\Delta_l = 1.5/2^l$ ($l = 0, 1, 2$) and check the pair-wise difference of the numerical solutions obtained decreases as expected. As is evident in Figure 1, as resolution is improved the differences decrease as expected. For all remaining tests we present results for the finest grid employed with $l = 2$.

3.2. Blast initial data

This is a variation of the MHD Blast problem (Del Zanna et al., 2003). In this test (Cécere et al., 2008), we evolve this initial data for different choices of boundary conditions setting $c_l = 20$ and $s = 1$ and examine the constraint's behavior in each case. The Figure 2 shows clearly that the numerical solution obtained with constraint preserving boundary conditions is superior by about an order of magnitude in constraint violation than the no-incoming case and almost

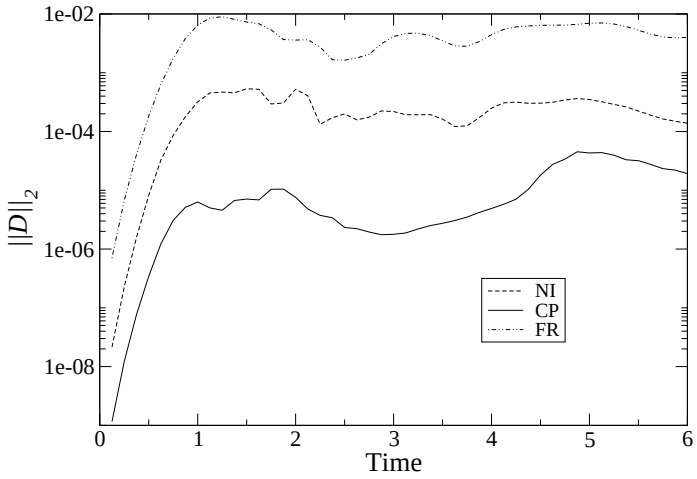

Figure 2. Behavior of the L_2 norm of the constraint for the different boundary value conditions.

three orders better than that obtained with the freezing boundary condition. An important point to emphasize is that a closer inspection of the solutions obtained reveals that the main contribution to the error originates at the boundaries in all cases (though with essentially the same behavior as far as the error's magnitude with respect to the boundary condition adopted). The norm displayed in the figure is calculated over the whole computational domain *ignoring* the last two points at all boundaries to avoid placing excessive weight on the violation at the boundary. Nevertheless, as indicated, constraint preserving boundary conditions give rise to a solution whose constraint is violated the least.

3.3. Rotor initial data. Effects of boundary conditions and divergence cleaning.

This is a variation of the MHD Rotor problem (Balsana & Spicer, 1999) which is smooth and allows for considering an additional flow field and initial constraint violation. We adopt (Cécere et al., 2008) this data to further examine the solution's behavior and allowing for initial violations of the constraint. The addition of the divergence driver allows for a dynamical reduction in the constraint violation until $t \simeq 4.6$, at this time the propagating modes interact with the boundaries which become the main source of error. Here again, one sees (Figure 3) that constraint preserving boundary condition gives rise to significantly smaller errors in the solution.
However, adopting the no-incoming modes *together* with the constraint damping field provides a reasonably similar behavior. This is due to the fact that the no-incoming boundary condition allows the outgoing constraint violating mode to leave the computational domain, while the incoming constraint violating

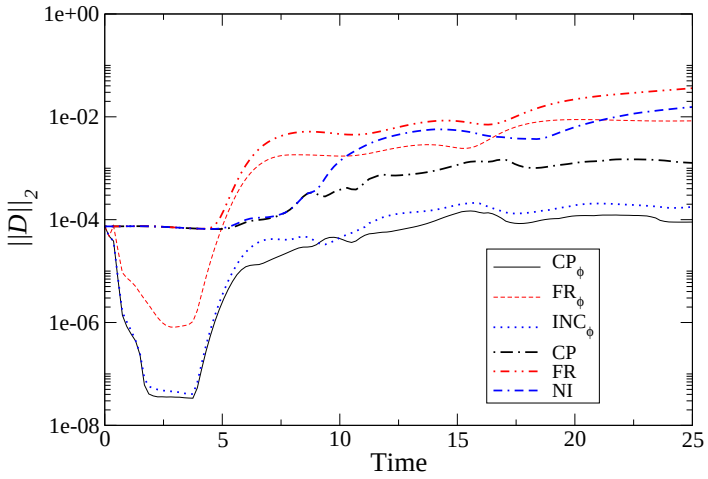

Figure 3. The solution's behavior with the different boundary conditions and with and without the use of the divergence driver.

mode, generated by not imposing the constraint preserving boundary condition, is damped to a significant degree by the divergence cleaning technique.

Another interesting behavior is revealed when varying c_l. This affects the constraint violating mode's propagation speeds which in turn has a strong influence in the solution's constraint behavior. In what follows we adopt the constraint preserving boundary condition. For this test we set $s = 0$ and choose c_l ranging from 10 to 80, together with adjusting the time step accordingly in order not to violate the Courant condition. In the Figure 4, the initial plateau corresponds to round-off values since the constraint is initially satisfied to that level. Once the non-trivial part of the solution reaches the boundary a significant violation of the constraint is generated. Depending on the boundary condition, and on the characteristic velocities of the system under consideration that violation propagates to the inside or just leave the domain. In our case, the ability of the constraint preserving boundary condition to allow constraint violating modes to leave the domain, results in smaller errors for faster propagating cases.

4. Conclusions

To examine the solution's behavior, we implemented the equations in Cartesian coordinates and with a spatial discretization that preserves the initial constraint error. This allows us to separate bulk from boundary effects and observe that the main violations do indeed occur at boundaries. To examine the boundary condition effects on the evolution we adopt three types of boundary conditions:

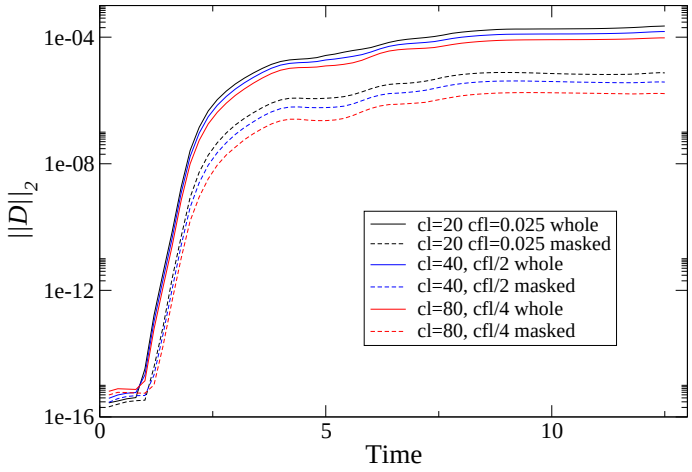

Figure 4. Behavior of the L_2 norm of the constraint for different values of the coupling constant c_l with constraint preserving boundary condition

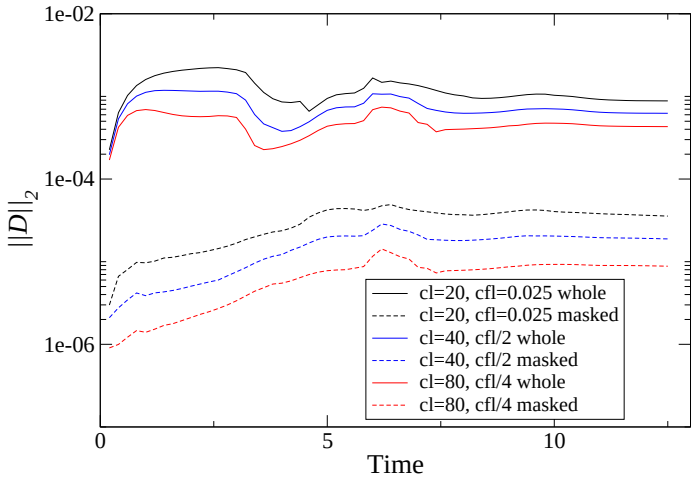

Figure 5. Similar to figure 4 but with initial data containing constraint violations.

• The most direct one, and crudest, sets to zero all right hand sides in a buffer boundary region. This might lead to inconsistencies for one might be prescribing conditions to outgoing modes.

• The second one is the "no-incoming" boundary condition where one projects out all incoming modes in the evolution equations leaving the rest (tangential and outgoing modes) intact. The implementation of this condition is slightly delicate as modes can change directions over time, and so may turn from being incoming to being outgoing and vice-versa.

• The third condition preserves the constraint in the sense that is deduced by setting to zero the incoming mode related to the constraint propagation. This condition is a modification to the previous one where now instead of projecting out all incoming modes, one incoming mode is fixed so that the incoming constraint mode is zero as a result.

The first option displays the worst behavior for the constraint as not only nothing is done to minimize the constraint violations introduced through the boundaries but further inconsistencies in the solution are induced there. As a result, in the best case the constraint mode bounces back from the boundary into the integration region. The second option performed substantially better displaying a gain of an order of magnitude in constraint preservation. This is a result of the boundary condition allowing for one of the ϕ modes –carrying constraint violations– to leave the integration region. With the third alternative an additional order of magnitude (at least) is gained with respect to the non-incoming condition. This condition not only allows for constraint violations to leave the computational domain but does not introduce significant violations at the boundary. Thus, we see that appropriately handling the boundary conditions the problem of constraint behavior can be significantly controlled.

References

Balsara, D., & Spicer, D. 1999, Journal of Comp. Phys., 148, 133

Cécere, M., Lehner, L., & Reula, O. 2008, Comp. Phys Com., 179, 545

Davidson, P. A. 2001, "An introduction to Magnetohydrodynamics", *Cambridge Univ. Press*, Cambridge

Dedner, A., et al. 2002, J. Comput. Phys., 175, 645

Del Zanna, L., Bucciantini, N., & Lodrillo, P. 2003, A&A, 400, 397

Goedbloed H., & Poedts, S. 2004, "Principles of Magnetohydrodynamics", *Cambridge Univ. Press*, Cambridge

Kim, J. S., et al. 1999, ApJ, 514, 506

Reula, O. 2004, Journal of Hyperbolic Differential Equations, 22, 251

First La Plata International School, 2008
Compact Object and their Emission, 2009
Ileana Andruchow & Gustavo E. Romero, eds.

Short Gamma Ray Bursts and Gravitational Waves

Ignacio F. Ranea-Sandoval

Facultad de Ciencias Astronómicas y Geofísicas, Universidad Nacional de La Plata, Paseo del Bosque s/n, 1900 La Plata, Argentina.
ignacio@carina.fcaglp.unlp.edu.ar

Abstract. Here we briefly review the present state of knowledge about possible sources of Gamma Ray Bursts (GRBs). In particular, we study the theoretical amplitudes of the Gravitational Waves (GWs) that different types of GRBs sources are supposed to emit. This is to be compared with the minimum detectable amplitude of actual Gravitational Wave Detectors, like the Laser Interferometer Gravitational-wave Observatory (LIGO) and VIRGO. Here we argue that this comparison may be used to favor some of the proposed short GRBs progenitors, against other models.

1. Introduction

Since their first fortuitous detection during the Cold War by the US Vela Nuclear Test Detection Satellite, the Gamma Ray Bursts (GRBs) have attained a great attention of high-energy astrophysicists. Their intriguing origin and extremely energetic nature were the main reasons for this interest. They are now becoming to be very well catalogued, and a wealth of experimental data is readily available.

The observational insights include light curves, energy release spectra, probable distance of the sources, etc. The experimental data is provided by satellites such as the Burst and Transient Source Experiment (BATSE), one of the instruments carried inside of the Compton Gamma Ray Observatory (CGRO), the Italian-Dutch satellite Beppo-SAX (SAX standing for "Satellite per Astronomia a raggi X"), and especially form the Swift Gamma-Ray Burst Mission and the High Energy Transient Esplorer (HETE-2), launched at the beginning of the XXI Century.

With all this phenomenological information, scientists noted that GRBs could be separated into two different families (Kouveliotou et al. 1993), the long GRBs (lGRBs) and the short ones (sGRBs). In Section 2, we discussed about these and some other aspects of GRBs.

Section 3 is devoted to describe sGRBs, which are our main concern in this monograph. We describe some of the models for sGRBs sources, which is one of the most important unsolved topics concerning GRBs.

In Section 4 we focus our attention on Gravitational Waves (GWs). This is a new window for high-energy astrophysics and cosmological studies. It is still a developing area and has not yet produced any reliable detection event. However, the comparison between the actual sensitivities of the detectors and the theoretical GWs amplitudes produced by different sGRB progenitor models, may be of some help to test them.

In Section 5, we discuss the case of the recently detected GRB 070201 which has generated some controversy among astrophysicists.

Finally, we bring some conclusions in Section 6.

2. Gamma Ray Bursts

GRBs are the most luminous events in the Universe discovered so far. lGRBs release a huge amount of energy, which is supposed to be highly beamed. In fact, the energy released is $\sim 10^{51}$ erg if the radiation is actually beamed; however, if it is not, it could be evaluated in the order of $\sim 10^{54}$ erg. For the short GRBs there are some uncertainties due to the lack of knowledge about their beaming factor, but their energy is supposed to be around 10^{48} erg. In both cases the energy release occurs in a very short interval of time. GRBs show spectra of non-thermal nature that for the lGRBs can be fitted with a number power law with index of ~ 1 for energies below ~ 100 keV, and ~ 2.5 for greater energies. The sGRBs present a similar feature, but the "break" energy has not been very well determined, mainly due to sensitivity limitations of GRB telescopes.

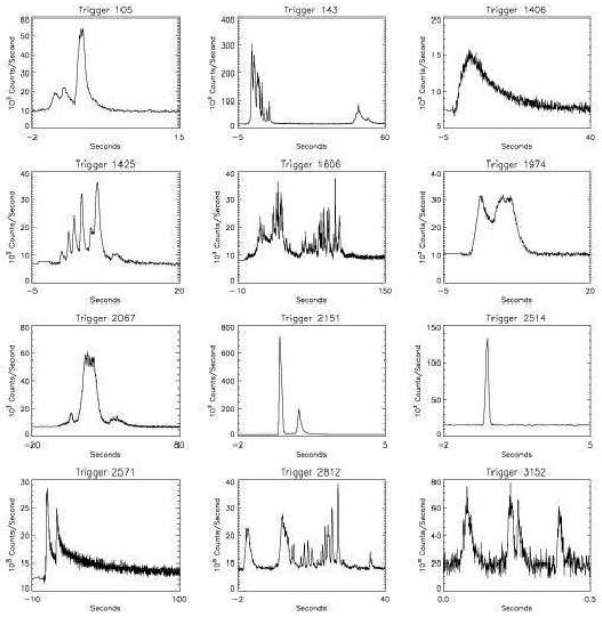

Figure 1. Different GRBs light curves. In the abscissa axis, time in seconds, and in the ordinate axis, 10^3 photon counts per second (Taken from the review of Mészáros 2006)

.

GRBs duration ranges form 10^{-2} s to 10^3 s and their rise-time could be as short as 10^{-4} s. Generally, GRBs light curves display very complex features showing millisecond γ-ray variability, but they always exhibit a sudden burst in their observed luminosities (with one or several peaks) followed by a slower decay (Fig. 1), see nontheless, Romero et al. 1999. As mentioned above,

in 1993, Kouveliotou et al. classified GRBs into two different groups (mainly distinguished by their duration), the sGRBs with durations of $T_{90} < 2$ s, and the lGRBs with duration $T_{90} > 2$ s (Fig. 2). The T_{90} parameter is defined as the time during which the cumulative counts form the source increase from 5% to 95% above the background. Other differences between GRBs of these two groups are that the short ones are less energetic, and probably less (or not at all) collimated as the lGRBs (Watson et al. 2006; Grupe et al. 2006). It is also important to note that, on average, the sGRB energy is released via harder (*i.e.* more energetic) photons than the longer ones.

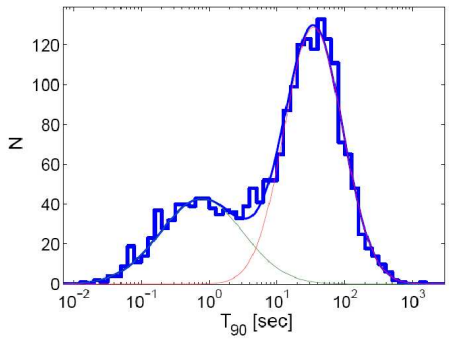

Figure 2. Bimodal duration distribution of GRBs showing two populations (Taken from the review of Nakar 2007).

A characteristic feature of GRBs is that the energy is released inside a very small region ($\sim$ 100 km) and on time scales of the order of a second. This localized and short explosion shall form a plasma almost absolutely opaque to its own γ emission due, mainly, to electron-positron pair production. According to this, no photons above the photopair production energy should be observed, even though observational data show that this is clearly not true. To solve this problem, relativistic expansion of the plasma was proposed (Piran 1999). Due to this relativistic expansion, the emitted photons are blueshifted, and the target density changes because the motion of the plasma. As a consequence, the corrected opacity could be smaller than one if the Lorentz factor of the plasma is of the order of 100, letting the energy to be radiated away. This is the basic picture of the fireball shock phenomenological model, which is capable of explaining, among other characteristics, the way energy escapes from the progenitor event.

Concerning their spatial distribution, GRBs are, within statistical uncertainties, isotropically distributed in the sky (see Fig. 3) in accordance with the requirements of every cosmological model. However, they are inhomogeneous in fluxes, with a paucity of weak bursts. All the available data is consistent with the hypothesis that GRBs have an extragalactic origin. It is also important to note that the Universe is transparent to GRBs because of their low energy γ-ray emission, making it possible to observe the short (and less energetic) ones at redshifts up to $z \geq 6$. This makes the information they carry of great importance to understand the formation of the first stars.

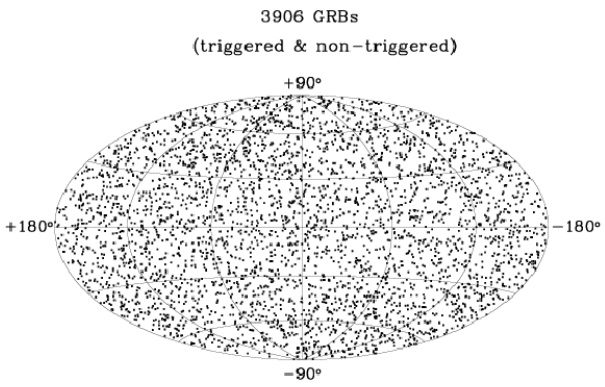

Figure 3. Sky distribution of 3909 GRBs from the BATSE Catalog, showing an isotropic distribution in Galactic coordinates. (Stern et al. 2001)

Currently GRBs are observed at a rate of about 1 event per day, so there are large quantities of new observational data to confront theoretical models.

3. sGRB

The very fast variability time scale that sGRBs show, make scientists think that a compact object with a mass similar to the Sun must be part of the GRBs central engine. If this was not the case, the time delay between different parts of the emitting region would make such short variability time scale impossible to observe. Different alternatives are proposed as sGRB progenitors. We would now briefly explain the main features of two of the most commonly accepted models.

3.1. Mainstream model: binary coalescence

Mainstream astrophysicists accept that sGRBs are the consequence of the merge of two compact objects: two neutron stars (NS/NS), a black hole and a neutron star (BH/NS) or some other type of binary system with two compact object involved. The physical foundation of the merger theory is that in any of this binary systems the components will lose angular momentum due to GW emission, making the merging unavoidable. Because of the absolute lack of spherical symmetry of these mergers, the amount of GWs emitted is supposed to be extremely large (Etienne et al. 2008; Ajith et al. 2008). Despite this fact, the huge distances from the sources make GWs elusive for current gravitational waves detectors. However, the expected sensitivities of new generation detectors such as advanced LIGO (an improvement to LIGO that it is said to be operative in 2015) would increase the "observable" volume of the universe dramatically (see Fig. 4). Advanced LIGO is expected to be capable of detecting GWs originated at distances up to the LEO Supercluster extending the chances of a detection.

Following the work of Flanagan & Hughes (1998), any binary coalescence process involving compact objects has three radically different phases: the inspiral, the merger and the ring down. The inspiral phase, occurs during the time

the system loses energy via GWs and make the components to spiral into each other. This phase ends when the objects reach the last stable orbit for the system, when the adiabatic evolution of circular orbits could not be used anymore. The merger phase starts at the moment the components come into contact. At this moment the system violently (*i.e.* on dynamical time scale) merge into a single black hole radiating some of its rest mass as GWs. Part of the mass could not cross the event horizon of this black hole, due to the fact that it retains too much angular momentum (Thorne 1974). The remaining material creates a disk, and its accretion could be the source of a GRB jet. During the ring down phase the system radiates (again, via GWs) the energy associated with initial deformations with which the black hole is formed. As a result of this process, the black hole achieves Kerr's geometry.

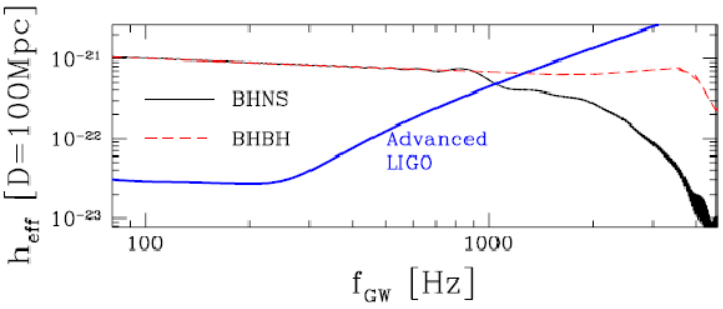

Figure 4. GW spectra for BH/NS and BH/BH, compared with advanced LIGO expected sensitivity (Adapted from Etienne et al. 2008).

Several differences exist between the spectra of GWs emitted by a BH/NS merger and the one involving two black holes. One of the more relevant is the fact that GWs emitted by BH/BH merger maintain more power at frequencies greater than 1000 Hz. Notice that BH/BH mergers ar dark at the electromagnetc spectrum since there is no matter to radiate. As a result these kind of mergers can not be considered as a GRBs progenitor candidate.

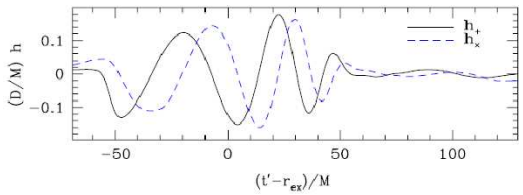

Figure 5. GW signal for the same case as in Fig. 3. The behavior of the two different polarization states is shown. D is the distance to the binary, t' the time respect to the time at which the apparent horizon is touched and r_{ex} a parameter of the model (Adapted from Etienne et al. 2008).

According to numerical calculations most of the gravitational radiation is emitted during the final stages of the merger phase and the beginning of the ring down one (Cutler & Thorne 2002). Because of that, many efforts in modeling these phases using a full general relativistic treatment are being made (see Etienne et al. 2008). This work has resulted in GW templates (Fig. 5) on which we could relay, in order to know the general aspects of the GWs is expected to observe from these events.

An unresolved issue regarding this model for sGRBs is that there are no observational data supporting beaming for these events. However, in merger systems there is a natural channel for emission along their rotational axis, giving as a result a beamed emission, though not observed yet.

3.2. An alternative model: accretion-induced collapse

There are alternative models that could explain the main characteristics of these ultra-energetic events. We are going to focus in one of these: The collapse of a neutron star into a black hole. As a result of accretion-induced collapse (AIC) in a binary system, a neutron star that reach its Chandrasekhar mass, would collapse into a black hole (MacFadyen et al. 2005; Dermer & Atoyan 2006). One of the argument used to propose this model is based on the fact that, of all the sGRBs with assigned approximate distances, 3 of them are associated with elliptical galaxies and none with supernovae. The total number of events with known distances is, however, small (see next Section). Note that in elliptical galaxies stellar formation has stopped. It is difficult to make compatible this observational fact and sGRBs progenitor models involving massive stars as their sources. Another argument is the fact that there are observations of neutron stars in binary pulsars, whose masses are much larger than the Chandrasekhar one, and so very likely to collapse to a BH by accretion.

To describe this process in more detail, the scenario we adopt is the following: a binary system, formed by a rapidly rotating neutron star and a white dwarf or a post main sequence stellar companion. During the evolution, the second component feeds matter to the neutron star through the Lagrangian point. As a result of the accretion, the neutron star exceeds its maximum stable mass and collapses to a black hole. This collapse, with high resemblance to the Type Ia supernovae, is far from spherically symmetric. As a result, during the final stages of the collapse, the rapidly rotating neutron star would be highly deformed. Because of this, emission of GWs is expected to occur during this process. There are no numerical studies of this model, and no theoretical template of the GWs that this kind of process would emit. This is the reason why the amplitudes of the waves produced by AIC are highly uncertain. Although, they are supposed to be much weaker than those produced during a merger. The GWs generated would be undetectable even with LIGO's future improvements (Kokkotas & Stergioulas 2005), if the source is located at distances greater than 10 Mpc. If a system formed by a black hole and an accretion disk is the engine of the GRB, then very optimistic models suggest that advanced LIGO could detect such GWs up to distances ~ 100 Mpc (Kobayashi & Mészáros 2003).

The lack of knowledge about the wave form is a major drawback for detecting this kind of waves, but it does not make it impossible. By using cross-correlation of the outputs of the two arms of LIGO they could still be detected.

4. Gravitational waves

GWs were predicted by Einstein in 1916, just a year after he published his general theory of relativity. Evidence of their existence is given by the observation of the shortening of the orbital periods of binary pulsars, such as the famous PSR J1913+16. Even though the concordance of the theoretical model for gravitational radiation emitted during the inspiral with the observations is excellent, there is to this date no direct evidence of GWs.

Studies on GRBs sources are associated with those related to GWs. The main reason for this is that all the electromagnetic information we can gather from GRBs and the subsequent afterglow, come from regions very far from the progenitors. On the contrary, GWs would provide information coming from regions near the source. This information is vital for determining the nature of the GRBs progenitors, especially the sGRBs.

In fact, due to the high density of the relativistic plasma fireball, both the γ-rays and the afterglow radiation are produced at distances greater than 10^{13} cm from the central engines. Instead, this plasma does not affect the propagation of GWs, which bring information on the nature of the progenitor.

The technology to build detectors that can be able to provide direct evidence of these waves is still developing. Owing to the weakness of gravity and its lack of dipole radiation, physical systems have very low efficiency for converting mechanical energy into gravitational radiation. These facts and the huge distances involved make GWs extremely difficult to be detected. No matter the great efforts that are being made, gravitational spectrum is still unexplored.

As the history of astronomy shows, whenever a new waveband window has been opened, a completely new family of unexpected phenomena was discovered. This is expected to be the case, in the close future, with the new GWs telescopes.

Depending on their source, GWs would have characteristic frequencies. We are interested in the high frequency band (ranging from 1 to 10^4 Hz) produced by stellar mass black holes. This is the region in which USA's detector LIGO, the French-Italian antenna VIRGO, the German-British detector GEO600 and the Japanese's TAMA300 operate. The low frequency band GWs, in which the Laser Interferometer Space Antenna (LISA) would operate, are produced by supermassive black holes which we are not discussing in this monograph.

LISA is a joint ESA-NASA projected GW detector expected to be launched not before 2018. This detector would consist in a three drag-free spacecrafts, that would be arranged to form an equilateral triangle, forming thus a Michelson interferometer. This interferometer would have 5 million kilometers arms and would be orbiting the Sun at the same distance as the Earth.

This kind of detectors are based on high precision laser Michelson interferometry with Fabry-Perot arms, whose detailed mechanism is beyond the scope of this monograph (see Ciufolini ed. 2001, for a detailed discussion). At present time, the detectors achieve a sensitivity to burst h_{SB} of approximately 10^{-21} at 100 Hz. With such sensitivities, these instruments are capable of detecting variations in longitude of about $\Delta l \sim 10^{-18}$ m (*i.e.* less than a thousandth part of a proton's diameter). The waves amplitude h for the merger sGRBs progenitors, can be calculated theoretically using "Newtonian/quadrupole" or higher order post-Newtonian approximation of the Einstein field equations.

The standard procedure to analyze the detectability of GWs is to compare h_{SB} with the characteristic amplitude $h_C \simeq h\sqrt{n}$, where n is the number of cycles the wave spend in a bandwidth $\Delta f \simeq f$ near the frequency f. A GW could be detectable if the condition $h_C > h_{SB}$ is satisfied.

Currently there are 7 sGRBs analyzed, with well estimated distances, being the closest at a distance of approximately 600 Mpc. The distance to a controversial eighth case is also claimed to have been estimated, we leave for next section a more detailed discussion of it. The first 7 sGRBs are located at distances where LIGO and every other ground based detector are incapable of detecting the GWs produced during the event, no matter the progenitor type it were. Just for comparison, we show in Table 1 that even the BH/BH mergers, that generates more GWs than any sGRB progenitor model, are still undetectable at such distances. Advanced LIGO is expected to reach the required sensitivities.

Table 1. Range of detectability of a 10 solar masses BH/BH coalescence for different GWs detectors. (Ciufolini ed. 2001)

Detector	GEO600	LIGO	VIRGO
Range (S/N=5)	75Mpc	160Mpc	190Mpc

5. The GRB 070201 case

At the beginning of 2007 an intense, short duration GRB (GRB 070201) was observed at about 1 degree from the center of M31 (Hurley et al. 2007, Pal'Shin 2007). A very interesting aspect of this sGRB is that its apparent location error band coincides with the spiral arms of M31. In a recent paper (LIGO Scientific Collaboration & Hurley 2007) the electromagnetic observations on this sGRB were compared with LIGO's data, which was the only detector then taking data on a scientific level. A set of very rigorous constrains to the nature of its progenitor were obtained.

They claimed, based on statistical arguments that, should GRB 070201 occurred in M31, the merger progenitor hypothesis can be excluded up to a 99% confidence level, and that other model has to be used. In the calculation, the model was supposed to describe a binary system scenario, with objects whose masses range from 1 to 4 solar masses for one, and from 1 to 40 solar masses for the other.

They also claim that, in order to preserve the merger scenario, GRB 070201 could not be hosted in M31. Another possibility (Mazets et al. 2007) is that the GRB 070201 was a Soft Gamma Repeater hosted in M31, whose GWs signal would be undetectable for LIGO. Soft Gamma Repeaters are highly magnetized neutron stars whose surface tectonic activity could be confused with some of the observed GRBs.

If the first is true, *i.e.* if this sGRB occurred at M31, the merger theory would suffer a drawback, because the amount of GWs that it would have pro-

duced should have been detected by LIGO with its present sensitivity. So, the merger theory shall be revisted or the usage of an alternative model for sGRBs progenitors should be considered.

6. Conclusions

We have presented very briefly some models for sGRBs sources and their relationship with GWs. We have also compared the theoretical profiles of the GWs that are supposed to be emitted and we have cofronted them with the actual ground-base GWs detectors. As a result, we have shown that the current technology is still not sensitive enough to detect GWs produced beyond the Milky Way or the Magellanic Clouds at most.

We have also show that, although there are many uncertainties, the merger model is expected to emit much more gravitational waves than the AIC model. So, any kind of observation produced using present time detectors that correlate sGRBs with GWs would strongly reinforce the merger theory.

Numerical calculation of templates of the GWs produced by AIC would be of extreme importance for comparison with data form GWs detectors, especially the data that would be available from the new generation of GWs detectors.

Acknowledgments. Author wishes to acknowledge reading of the manuscript, and very valuable suggestions and useful comments, made by Charles D. Dermer. The author is a fellow of CICBA.

References

Ajith, P., et al. 2008, arXiv:0710.2335v2

Ciufolini, I., Gorini, V., Moschella, U., & Fré, P. (edts.) 2001, *Gravitational Waves*, High Energy Physics, Cosmology and Gravitation Series, Institute of Physics Publishing, Bristol and Philadelphia

Cutler, C., & Thorne, K. S. 2002, arXiv:gr-qc/0204090

Dermer, C. D. & Atoyan, A. 2006, ApJ, 643, L13

Etienne, Z. B., et al. 2008, Phys. Rev. D, 77, 4002

Flanagan, É. É., & Hughes, S. A. 1998, Phys. Rev. D, 57, 4535

Grupe, D., et al. 2006, ApJ, 653, 462

Hurley, K., et al. 2007, GRB Coordinates Network, Circular Service, 6103, 1

Kobayashi, S., & Mészáros, P. 2003, ApJ , 589, 861

Kokkotas, K. D., & Stergioulas, N. 2005, arXiv:gr-qc/0506083

Kouveliotou, C., et al. 1993 ApJ, 413, L101

LIGO Scientific Collaboration, & Hurley, K. 2007, arXiv:0711.1163

MacFadyen, A. I, Ramirez-Ruiz, E., & Zhang, W. 2005, arXiv:astro-ph/0510192

Mazets, E. P., et al. 2007, arXiv:0712.1502

Mészáros, P. 2006, Rep. Prog. Phys., 69, 2259

Nakar, E. 2007, Phys. Rep., 442, 166

Pal'Shin, V. 2007, GRB Coordinate Network, Circular Service, 6098,1

Piran, T. 1999, Phys. Rep. 314, 575

Romero, G. E., et al. 1999, MNRAS, 308, 799

Stern, B. E., et al. 2001, ApJ, 563, 80
Thorne, K. S. 1974, ApJ, 191, 507
Watson, D., et al. 2006, A&A, 454, L123

Author Index